Flow on streamwise-curved surfaces: forced transition and turbulence

Davide Pirrò
Politecnico di Milano,
Dipartimento di Ingegneria Aerospaziale
Corso di Dottorato XVII ciclo

Relatore: Prof. Maurizio Quadrio
Tutor: Prof. Luigi Vigevano

Aprile 15, 2005

ABSTRACT

The flow on non-planar surfaces with curvature in the streamwise direction is studied through direct numerical simulations (DNS) and laboratory experiments. Two typical cases are considered: the Taylor-Couette flow (i.e. the flow in the gap between two rotating cylinders) and the Dean flow (i.e. the pressure-driven flow in a curved duct). Each flow is characterized by a laminar solution, which becomes centrifugally unstable above a critical value of the Reynolds number, so that elongated, streamwise-oriented, large-scale, vortical structures develop. By growing the Reynolds number, increasingly complicated flow portraits determined by successive bifurcations appear until the turbulent regime is reached, and qualitatively similar large-scale structures can still be observed.

The numerical simulations have been carried out by using a pseudo-spectral parallel code which is periodic in the homogeneous (streamwise and spanwise) directions, and uses high-accuracy compact finite-difference schemes for the discretization of the radial direction. The experiments have been conducted at the Manchester Centre for Nonlinear Dynamics on a Taylor-Couette apparatus.

In the first part of the work, we study the pattern of transition to turbulence produced by both temporal and spatial forcing in the Taylor-Couette geometry, respectively through numerical simulations and experiments. The effect of temporally modulating the velocity of the inner cylinder, being the outer at rest, is investigated with DNS in a range of the relevant parameters (Reynolds number, modulation frequency) which is wider than that considered in the literature. The issue of spatially modulating the shape of the inner wall is explored with a campaign of experiments, where a sinusoidally-shaped inner cylinder is built and tested.

In the second part of this thesis the focus shifts to the turbulent regime. The presented Taylor-Couette simulations are the first well-resolved turbulent DNS, whereas the simulations of the Dean flow are the first accurate attempt to analyse in detail how curvature affects the statistical properties of the flow (e.g. mean streamwise velocity profile, friction coefficients etc.). The typical features of wall-bounded turbulence can be observed in both flows. Besides for the Taylor-Couette flow, the large-scale structures, which appear and develop in various ways in the first stages of transition, reappear in turbulent regime, and influence mean and instantaneous properties of the flow. The contribution of the large-scale structures to the turbulent statistics is quantified and discussed.

Ai miei genitori

ACKNOWLEDGEMENTS

First of all, I want to thank my supervisor, prof. Maurizio Quadrio, for his continuous support and all the useful suggestions given during my research. When, at the very dawn of this thesis, he said working on this subject would be exciting he was absolutely right.

I also wish to thank all the members of the Manchester Centre for Nonlinear Dynamics, University of Manchester, where I spent six amazing and rainy months working on the sinusoidally-shaped rotating cylinder (also known as the Monica Bellucci's cylinder): your kindness and support helped me a lot; who is taking care of Monica now?

In particular, I am deeply indebted with prof. Tom Mullin, who shared with generosity his enthusiasm and huge knowledge on the subject, and with Dr. A. I. Khan who helped me with the setting-up of the experiments and explained the secrets of kabbadi.

I also thank prof. Renzo Piva who read a preliminary version of the work and whose comments and remarks have considerably improved this thesis.

The members of the office 41 at the DIA deserve a special mention for the joyful atmosphere created in these years and for the help given in the filling of the nicknames' blackboard: it was hard work guys, but we did it.

My Italian and Greek friends with which I shared most of my leisure time already know how important they are: *ευχαριστω πολυ*, compatrioti.

My family (pa', ma', Paola, Patri, Tony, Antonio, Lorenzo, Marco) has always been present and has constantly encouraged me: I couldn't have accomplished this without your endless support.

And I thank you Olivia, for your love.

CONTENTS

CHAPTER 1

INTRODUCTION

In this initial chapter a concise description of the Taylor-Couette and Dean flows is presented, through a definition of the geometries and the characteristic parameters. Besides, a minimal review of the massive literature on the subject is provided, as well as the reasons which have motived this work. An outline of the thesis closes this introductory chapter.

1.1 Background

Many flows of engineering interest are characterized by streamwise-curved surfaces such as the flows through an array of blades in a turbomachine, and those on airplane wings or in curved ducts; the behaviour of the streamlines in these flows is such that centrifugal instabilities exist (see [22], [36]), which influence the pattern of transition to turbulence since the early stage of this process. Moreover, centrifugal instabilities produce, under proper circumstances, large-scale, vortical structures which are oriented in the streamwise direction. These large-scale structures deeply affect the mean and instantaneous characteristics of the flow.

It is customary [102] to classify the flow on curved surfaces in three main groups, each representative of a wider category of flows: (1) the flow in the gap between two concentric, rotating cylinders (referred to as Taylor-Couette flow, TCF hereinafter), where the driving force is the movement of the walls; (2) the flow generated by a pressure gradient in a streamwise-curved duct (referred to as Dean flow, DF hereinafter); (3) the boundary layer over a concave walls (referred to as Görtler flow). In the present work only the first two classes will be considered.

The importance of the TCF geometry relies not only on its relevance as a prototypical flow, but also on its engineering applications; we recall, among the others, its employment as photo-catalytic and photochemical reactor (see

[104], [48], [78], [118], [93]). In the same way, the comprehension of the curvature-related effects in the Dean flow is pivotal in the design of devices where a fluid is forced to flow between confined streamwise-curved walls.

The numerical codes commonly used in industry for the design of fluid-related devices work out their results by solving RANS equations or implementing LES; in presence of highly circulatory phenomena, they need proper models for the representation of pressure-driven and/or shear-driven turbulent flows. However, the modelling of these flows is far from satisfactory.

In the present work, the TCF will be considered mostly in connection with the basic problem of affecting its pattern of transition to turbulence through temporal or spatial forcing, as well as with the issue of describing and quantifying the interaction between turbulence and the large-scale vortical structures. For the DF, the focus will be on applicative and modelling issues, as the presence of a logarithmic region for the mean velocity profile, or the dependence of friction coefficients on curvature.

1.2 Taylor-Couette flow

The TCF is the flow in the gap between a pair of coaxial rotating cylinders. The geometry is sketched in fig. 1.1, where the azimuthal (streamwise) direction is labeled as θ, the spanwise direction as z and the radial direction as r. The radius of the inner cylinder is $\mathcal{R}_i$, the radius of the outer is $\mathcal{R}_o$, the axial extension of the cylinders is H, and the gap width between the cylinders is $d = \mathcal{R}_o - \mathcal{R}_i$. The angular velocity of the inner and outer cylinders are Ω_i and Ω_o, respectively, and their ratio is $\Omega = \Omega_o/\Omega_i$. The fluid is confined in the upper and lower extremities by two lids, which can either rotate with the same angular velocity of one of the cylinders, or be stationary, in dependence of the chosen experimental setup. The shape and the relative movements of the lids strongly affect the flow characteristics [9], and are responsible for the so called end-effects [63].

Being the geometry fixed, and neglected the effects of gravity and other external forces, the only relevant fluid dynamic parameters are the Reynolds numbers R_i and R_o related to the inner and outer cylinders:

$$R_i = \frac{\Omega_i \mathcal{R}_i d}{\nu}, \qquad R_o = \frac{\Omega_o \mathcal{R}_o d}{\nu},$$

where ν is the kinematic viscosity of the fluid. Instead of the Reynolds number, for historic reasons, it is possible to encounter in several references

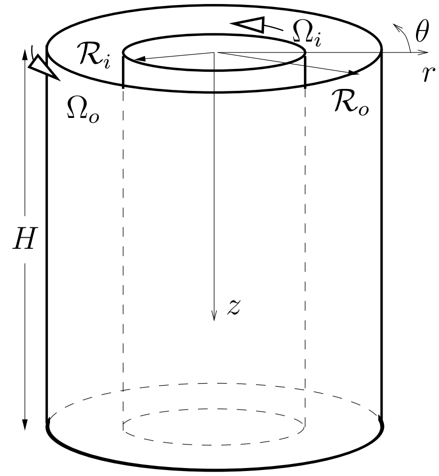

Figure 1.1: Geometry of the Taylor-Couette problem.

the Taylor number:

$$Ta_i = \frac{\Omega_i^2 d^4}{\nu^2} = R_i^2 \left(\frac{1-\eta}{\eta}\right)^2, \qquad Ta_o = \frac{\Omega_o^2 d^4}{\nu^2} = R_o^2 \left(\frac{1-\eta}{\eta}\right)^2,$$

where $\eta = \mathcal{R}_i/\mathcal{R}_o$ is the ratio between the inner and the outer radius; η discriminates the case of small-gap geometries, where η is close to 1, from that of large-gap. The parameter $\Gamma = H/d$ represents the ratio between the height of the cylinders and the gap width. It is useful to distinguish cases with long cylinders, where $\Gamma \approx \mathcal{O}(10)$, from those of short cylinders, with $\Gamma \approx \mathcal{O}(1)$.

The first experiments on the TCF were performed by Couette [26] and Mallock [76] (see [33] for an overview on historic experiments) in the late 19th century. In this very dawn of the subject, the attention was focused on the design of a device to measure easily and accurately the dynamic viscosity of the fluid μ; in fact, at low value of the Reynolds number [33], the following formula:

$$G = \frac{4\pi\mu\mathcal{R}_i^2\mathcal{R}_o^2 H(\Omega_i - \Omega_o)}{\mathcal{R}_o^2 - \mathcal{R}_i^2}$$

expresses the torque G transmitted to a length H of one cylinder as a result of a rotation of either, as a function of the angular velocities, the geometric parameters and the fluid viscosity.

However, it was only in 1923, with the seminal work of Taylor [114], that the main characteristic of the TCF was discovered. In his study with a fixed outer cylinder device Taylor showed, both by experiments and calculations, that, as a consequence of centrifugal instabilities, above a critical value $R_{i,cr}$ of the Reynolds number, the laminar solution [6]

$$w^l(r) = \frac{\Omega_i \mathcal{R}_i}{1-\eta^2} \left[\frac{\mathcal{R}_i}{r}(1-\eta) - \frac{r}{\mathcal{R}_i}(\eta^2 - \Omega) \right] \tag{1.1}$$

becomes unstable, and doughnut-like, large-scale, vortical structures appear in staggered arrays within the flow. Since then, these structures bear the name of Taylor vortices (TV).

Many papers on the subject (for a review see [112]) later defined the properties of TV, as the number N of vortices for a given cylinder length or, otherwise stated, the axial vortex wavelength $\lambda_z = H/N$ (see [63]), and the influence of the end-effects on the development of such structures [10]. Besides, owing to the instability of the laminar solution the TCF was also analysed under the point of view of bifurcations in nonlinear systems (see [30], [8], [24], [28], [23]). Experiments (see [19], [9]) and numerical simulations (see [1], [80], [42], [87]) showed that both $R_{i,cr}$ and N depend on the geometry and on the characteristics of the experimental setup (see [108], [89], [29]).

To analyse the transition scenario, we start by considering the case of outer cylinder at rest, i.e. $R_o = 0$. As R_i increases further above $R_{i,cr}$ and reaches a certain value $R_{i,w}$, the TV experience an Höpf bifurcation and gain azimuthal waviness, characterized by an azimuthal wavenumber m. The name "wavy Taylor vortices" (WTV) is used to describe the TV in this state. As the value of R_i grows further, the flow can shift from one mode, described by the pair (N, m), to another; the experience has shown that the pair (N, m) depends on the geometry (see [58],[57]).

Besides, as a consequence of the high nonlinearity of the problem, above a certain value $R_{i,nu}$ of the Reynolds number the solution is not unique and the observed mode depends on the flow history, (see [25], [8]).

At even higher values of the Reynolds number, an additional modulation of the azimuthal waviness settles (see [45], [20], [60]), which can be seen as a further Höpf bifurcation, leading to a torus-like attractor [27]. In this regime the vortices are called "modulated wavy Taylor vortices" (MWTV). Successively, as the first signals of chaotic motion appear [113], doughnut-like structures, with an axial wavelength different from their low-Reynolds number counterparts [19], still exist and even when a fully turbulent regime is established they thrive, although immersed in a noisy background. In this late stage of their existence, which seems to stop only at very high values of R_i [106], these so-called "turbulent Taylor vortices" (TTV as in [94], [62]) influence the mean and instantaneous flow field properties. The experiments carried out at even higher Reynolds number focused on the existence of scaling laws (see [46], [69], [40]), and structure functions (see [12], [66], [111]).

In fig. 1.2 snapshots of the above mentioned regimes (i.e. TV, WTV, MWTV and TTV) are reported for different geometries, characterized by the pair (η, Γ), in devices with the outer cylinder at rest ($R_o = 0$). As R_i grows the TV (fig. 1.2(a)) are observed to gain more and more azimuthal waviness, by becoming first WTV (fig. 1.2(b)) and then MWTV (fig. 1.2(c)); eventually, they enter the turbulent regime as TTV (fig. 1.2(d)).

The pattern of transition to turbulence varies heavily in dependence of both geometric and fluid dynamic parameters (as a cross-check of [2] and [103] shows): in fact the gap, the length of the cylinders and the end-effects all contribute to the selection of the flow.

The richness of patterns hidden behind the TCF geometry becomes even larger when more free parameters are introduced. When the outer cylinder is rotated spiral flows (see [107]), turbulent spots and turbulent spirals (see [50], [70], [81], [90]) appear, as pictured in fig. 1.3. Spiral flows can also appear in both laminar (see [121], [117]) and turbulent [3] regime, as a consequence of an axial flow superimposed on the TCF.

As a side aspect, we mention that the above-described pattern of transition has been interpreted as an example of transition to turbulence via the Landau's scenario [64] of successive bifurcations; this theory, though very suggestive, is today widely questioned [43]. Moreover, this geometry has been one of the first cases in which the theory of the strange attractors has come to valuable results [17].

Being the transition scenario of TCF reasonably well understood, reports have recently appeared in literature where the aim is to control the mass transport and mixing properties of the Taylor counter-rotating cells by suitable changes in the geometry of the problem. Of particular interest are those papers dealing with the forcing of the TV via temporal modulation of the inner cylinder velocity [126], or spatial modification of the inner cylinder shape [37]. In fact, through a temporal forcing, Youd, Willis & Barenghi [125] have demonstrated the existence of reversing and non-reversing TV, whose existence is related both to the value of the Reynolds number and the frequency of forcing. The spatial forcing which is realized in [38], through a sinusoidally-shaped inner cylinder, has shown that the characteristics of the TCF are significantly affected by the wavelength of the sinusoidal modulation. The open issues on the temporal and spatial modulated TCF that will be discussed in the present work are described respectively in §1.4.1 and §1.4.2.

A number of numerical simulations was carried out in the past for the TCF in cylinders with both infinite and finite lengths (see [67], [77], [72],[101]). However, the values of Reynolds number at which these simulations were performed are far from the turbulent regime, with the only exception of [51],

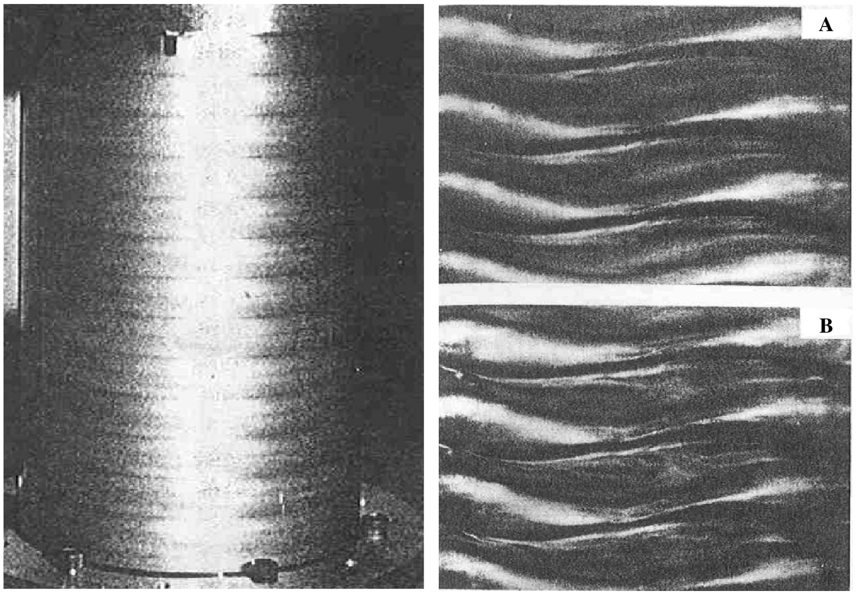

(a) TV: $R_i = 830$, $\eta = 0.889, \Gamma = 30$.

(b) WTV: $R_i^A = 1251$ and $R_i^B = 1404$, $\eta = 0.875, \Gamma = 20$.

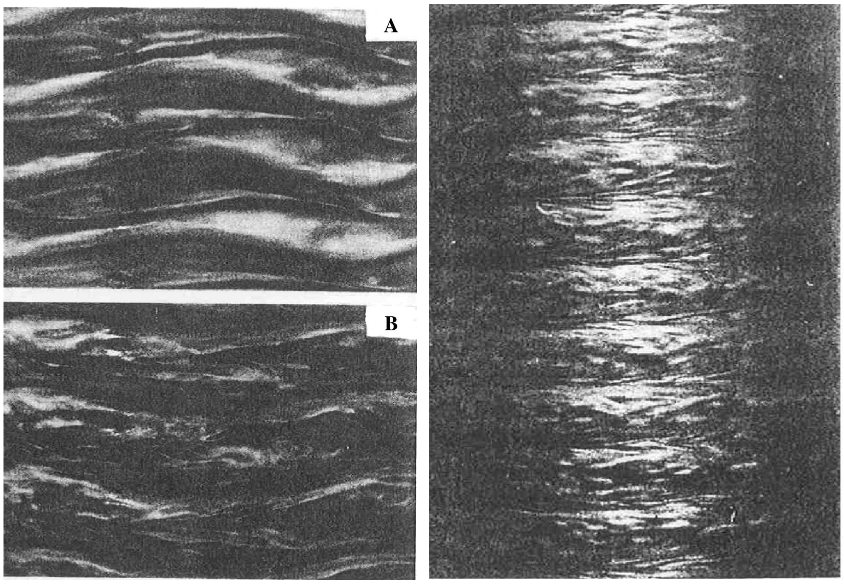

(c) MWTV: $R_i^A = 1487$ and $R_i^B = 1982$, $\eta = 0.875, \Gamma = 20$.

(d) TTV: $R_i = 5240$, $\eta = 0.896, \Gamma = 123$.

Figure 1.2: Flow regimes in the TCF with $R_o = 0$: TV (from [25]), WTV (from [17]), MWTV (from [17]) and TTV (from [62]).

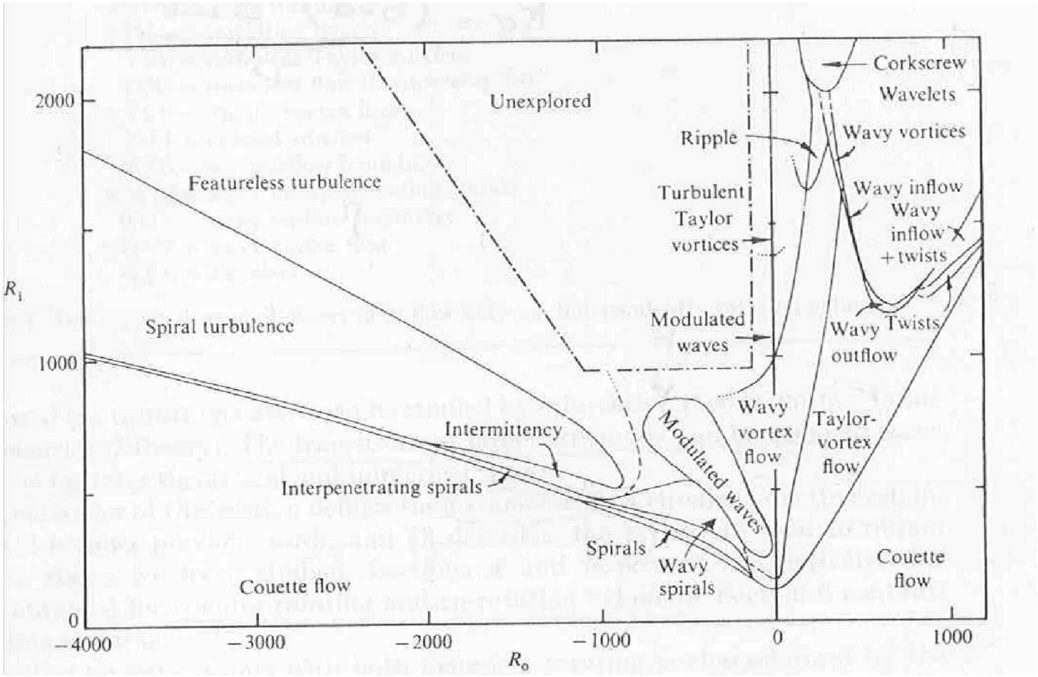

Figure 1.3: Map of the TCF for a $\eta = 0.833, \Gamma = 30$ apparatus (from [2]).

which is nevertheless not well resolved. The direct numerical simulation (DNS) of the Navier–Stokes equations for low-Reynolds number turbulent wall flows has become, in recent years, a valuable tool for basic turbulence research [84], both as complement and in substitution of laboratory experiments. It appears however that DNS has not yet been exploited to its full power for TCF investigations. As a consequence, till now, the turbulent regime remains largely unexplored numerically. The open issues on the TCF in turbulent regime that will be discussed in the present work are described in §1.4.3.

1.3 Dean flow

The DF develops when a pressure gradient drives a fluid in a streamwise-curved channel. In fig. 1.4 a curved channel is sketched, where the azimuthal (streamwise) direction is labeled as θ, the spanwise direction as z and the radial direction as r. The radius of the centre of the channel is $\mathcal{R}_c$, L_z is the axial (spanwise) extension of the channel and l_θ is the azimuthal extension expressed in radians. We note that the streamwise extension of the channel for the centreline is $L_\theta = l_\theta \mathcal{R}_c$. The radius of the inner wall and outer wall

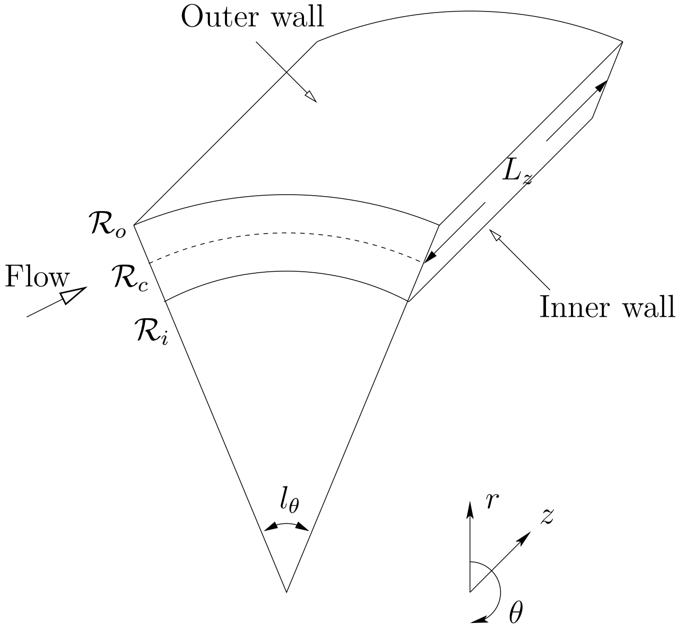

Figure 1.4: Geometry of the Dean problem.

are respectively $\mathcal{R}_i$ and $\mathcal{R}_o$, and they are related to the half width of the channel δ by $\mathcal{R}_o - \mathcal{R}_i = 2\delta$. The degree of curvature of the channel is usually expressed as $\gamma = \delta/\mathcal{R}_c$; the curvature coefficient γ and the ratio η between the inner and outer radius are related by the formula $\eta = (1-\gamma)/(1+\gamma)$.

A suitable Reynolds number is

$$Re = \frac{U_b \delta}{\nu},$$

which is based on the bulk velocity U_b, the half-width of the channel δ and the viscosity of the fluid. The bulk velocity U_b is related to the mass flow per axial length Q by $Q = 2U_b\delta$. Instead of the Reynolds number it is possible to encounter, in literature, the Dean number:

$$De = Re\sqrt{\gamma},$$

which takes into account also the curvature parameter.

In his seminal work [31] dated 1928, Dean observed that as De exceeds a certain threshold, the laminar solution [6]:

$$w^l(r) = \frac{P_\theta}{2\nu}\left[r \log r + Ar + Br^{-1}\right], \tag{1.2}$$

where $A = (\eta^2 \log \mathcal{R}_i - \log \mathcal{R}_o)(1-\eta^2)^{-1}, B = (\mathcal{R}_i^2 \log \mathcal{R}_i)(1-\eta^2)^{-1}$, is no more stable, and streamwise-elongated, large-scale, vortical structures develop close to the outer wall of the curved channel. These vortices are now called Dean vortices (DV). Like its TCF counterpart, the characteristic dimension of the DV is the axial wavelength of the vortical structures; although the DV are quite similar to TV, their characteristic dimensions are, however, different.

As the Dean number increases, a pattern of transition to turbulence develops which is a pale image of the rich scenario of transition to turbulence discussed for the TCF. In fact, DV may merge or split (see [14], [13], [47]), and this reduces or increases, respectively, the number of vortices in the channel, and, as a consequence, their characteristic wavelength. However, another scenario is possible (see [44], [68]), in which the streamwise vortices deform in the azimuthal direction and successively travelling waves appear. At first, a wave characterized by small azimuthal wavelength, corresponding to undulating vortices, is present and successively wavy-like structures, with large azimuthal wavelength, appear, which are known as twisting vortices. The undulating vortices are quite similar to the WTV, while the twisting vortices have no counterpart in the TCF. Once the turbulent regime is reached, the presence of elongated structures become subject of some controversy. In fact, the existence of large-scale turbulent Dean vortices (TDV) has been questioned by some researchers, while others [52] believe that they do exist at all (see [96] for a complete review of the subject).

In analogy with the TCF, we emphasize that the exposed pattern of transition (see [11], [83]) depends heavily on the degree of curvature of the channel as well as on end-effects, caused by the finite spanwise width of the curved channel.

Owing to its importance in practical applications, the DF in the turbulent regime has been studied more thoroughly than TCF to the aim of a general understanding of the underlying physics of turbulence in presence of streamwise curvature. This turbulence-focused attitude is an important difference from the TCF, where the largest efforts have been devoted to the study of the first stages of transition. The milestone work of Bradshaw [16], and a full chapter of [116] are dedicated to the effects due to curvature in turbulent flows, and a modern comprehensive review of the subject can be found in [96]. As pointed out by Bradshaw [16], curvature effects on the average properties of a flow in turbulent regime are heavily nonlinear, and, in particular, the extra rate of strain imposed by streamwise curvature turns out to be one order of magnitude larger than what would be inferred from an analysis of the equations of motion.

As a consequence, massive differences exist between the turbulent straight channel flow and a curved channel flow with even the smallest curvature. Experimental (see [44]) as well as numerical analyses (see [85], [124], [91]) of the DF have been carried out in the past to elucidate how streamwise curvature affects the transition to turbulence and eventually the turbulence itself; nevertheless, some fundamental issues deserve further investigation. These aspects will be mentioned in §1.4.4.

1.4 Motivations

The aim of the present work is twofold. In the first half of the work, which is schematically represented in the left part of the large central box in fig. 1.5, we have considered the non-turbulent regime. The effect of temporal modulations of the inner cylinder velocity (upper quadrant, numerical study) and of the spatial modulation of the inner cylinder shape (lower quadrant, experimental study) are studied to understand how such forcing modifies the pattern of transition to turbulence in TCF. In the second half of the work (the right part of the box), turbulence itself becomes the central subject of our study, carried out through direct numerical simulations. In fact, both TCF (upper quadrant) and DF (lower quadrant) are considered in turbulent regime, to the aim of characterizing the behaviour of engineering-relevant parameters (e.g. friction coefficients, mean velocity profiles, turbulence intensities etc.) and of analysing how large-scale and small-scale structures coexist and interact.

1.4.1 Time-modulated TCF

Let us consider the TC problem with a co-sinusoidal time modulation of the inner cylinder velocity:

$$w_i(t) = \Omega_i(t)\mathcal{R}_i = \Omega\mathcal{R}_i\cos(\omega t),$$

with a zero mean rotation and the outer cylinder at rest, i.e. $\Omega_o = 0$. Both stability analyses [92] and numerical simulations [125] have shown that, in the low-frequency regime, $R_{i,cr}$ is higher than in the no-modulation case. Moreover, recent numerical simulations conducted by Youd, Willis & Barenghi [125] have shown that two kinds of flow exist, in dependence of the Reynolds number and the oscillation frequency: (1) a reversible-TV flow (where the sense of rotation of the TV changes as the inner cylinder goes from positive to negative velocities); (2) a non-reversible TV flow.

However, these interesting results are available in literature just on a small region of the two-dimensional space parameters made by Reynolds number and modulation frequency. Moreover, the physical meaning of these flows has not been considered in detail. We believe that the extensions of the results to higher values of both frequency oscillation and Reynolds number

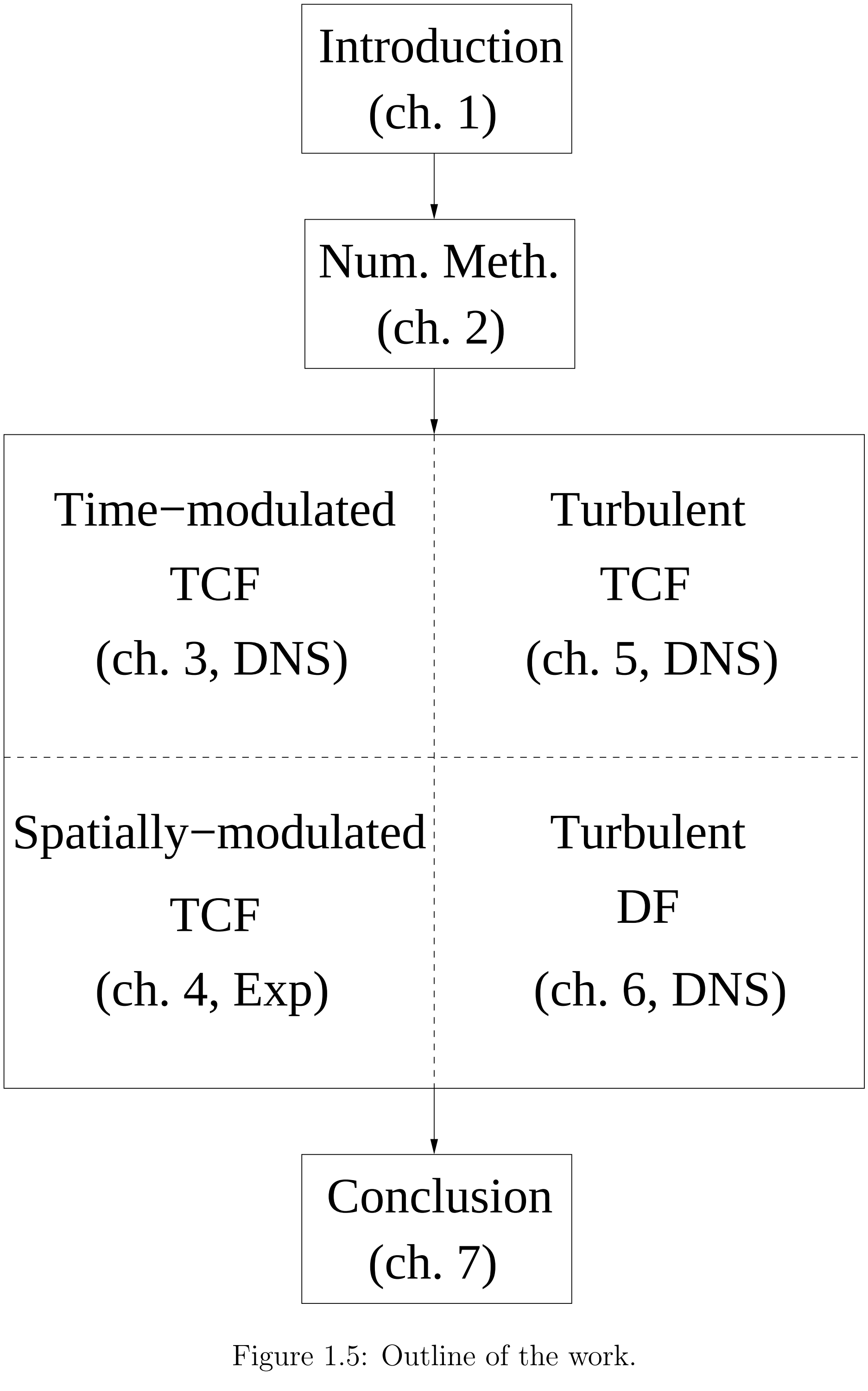

Figure 1.5: Outline of the work.

could be interesting and instructive. In fact, by growing the frequency of oscillation, it could be possible to determine, if any, the critical frequency at which the TV cease to exist, and which kind of flow substitutes them. Besides, by reaching values of Reynolds number which are associated with WTV, it could be possible to see whether the temporal forcing interacts with the periodic nature of the flow in an almost resonant behaviour. These points will be addressed in detail in chapter §3.

1.4.2 Spatially-modulated TCF

Among the several devices which have been proposed to modify the behaviour of the cellular-like structures, those that force the vortex wavelength have been the most studied. We can cite the experimental studies of Wiener et al. [122] on an hourglass geometry, that of Ikeda & Maxworthy [54] on a sinusoidal modulated inner cylinder at rest and a moving outer one, and the very recent ones by Drozdov, Rafique & Skali Lami [37] and Staples & Smits [109] both on the moving sinusoidal inner cylinder with the outer one at rest.

In particular, the last two works present a qualitative description of the pattern of transition to turbulence. We believe that an accurate quantitative description of the transition to turbulence scenario could be very interesting in determining the effects caused by the wavelength forcing. Besides, the non-uniqueness which is typical of the TCF for the straight cylinder, has not yet been explored for sinusoidally-shaped inner cylinders. These points will be discussed in detail in chapter §4.

1.4.3 Turbulent TCF

Although TTV have been deeply investigated since the seminal work of Pai [94], dated 1943, the difficulties of experimental measurements and the limited availability of accurate numerical simulations have determined a shortage of data on the behaviour of the TTV, which are typically described through flow visualisations, or with single-probe experimental measurements.

We believe that, by analysing the high-Reynolds number regime through an accurate DNS, it could be possible to provide a large amount of information on the behaviour of the flow in terms of mean velocity, turbulence intensities, high-order statistics. Moreover, a contribute on the existence of a logarithmic law for the concave and convex wall, which is still an open problem (see [96]), could be given, eventually leading to an improvement of the current RANS and LES modelling of rotating flows driven by wall movements. Lastly, it is our aim to describe the interaction of wall turbulence with TTV, by computing their relative contribution to the usual turbulent statistics. These points will be discussed in detail in chapter §5.

1.4.4 Turbulent DF

In spite of its above-mentioned importance, to our knowledge there are only a few number of direct numerical simulations on DF in turbulent regime (namely [85], [91], [124]). Besides, the results presented in literature sometimes disagree: for example the effect of curvature on the turbulent intensities is considered negligible by [85] and very important by [91]. Moreover, the analyses of some fundamental points remain at preliminary stage, as the behaviour of the friction coefficient as a function of the curvature on the concave and convex surfaces, which have been studied by [91] but without particular discussion of the obtained results.

Another fundamental issue for engineering applications and turbulence modelling (RANS, LES) is the questioned existence of a logarithmic law for the streamwise velocity. These points will be addressed in detail in chapter §6.

1.5 Outline of the thesis

The outline of the thesis has been already sketched in fig. 1.5. The numerical method used for the direct numerical simulations will be presented in chapter §2, with emphasis on its design, targeted towards parallel computing and commodity hardware. In chapter §3 numerical simulations of a time modulated TCF in a wide-gap geometry will be discussed. A map of the flow regimes as a function of the Reynolds number and the frequency of modulation will be presented, and the nature of the flows will be analysed in detail. The results of a campaign of experiments on a TCF, with a sinusoidally-shaped inner cylinder, will be presented in chapter §4. Chapter §5 opens the part of the thesis devoted to the fully-turbulent regime, and describes the TCF in turbulent regime. The analysis of the turbulent DF at several degrees of curvature, carried out through DNS, is the subject of chapter §6. Finally, in chapter §7 some general conclusions will be given, and the main results presented in the previous chapters will be summarized and discussed on a global optics; besides, some possible future developments will be hinted.

CHAPTER 2

NUMERICAL METHOD

The numerical method used for the simulations presented in chapters §3, §5, §6 will be introduced in this chapter. For a more detailed description of the method, as well as for its parallel strategy and performance, the paper [99] by Quadrio & Luchini must be taken as reference. Since this publication may not be readily available, we report here the main characteristic of the numerical method, and the minor adjustments implemented during the present work.

2.1 The direct numerical simulation

The direct numerical simulation (DNS) of the Navier–Stokes equations for incompressible fluids in geometrically simple, low-Reynolds number, turbulent wall flows has become in the last years a valuable tool for basic turbulence research [84]. A few examples of such flows are the turbulent plane channel flows and boundary layers (which naturally call for the use of a cartesian coordinate system), and turbulent pipe flows and flows in ducts with annular cross-sections (which are well suited for the cylindrical coordinate system).

Despite their practical relevance, turbulent flows in pipes and circular ducts have not been studied so deeply through DNS as their planar counterparts. This can be at least partially ascribed to the numerical difficulties associated with the cylindrical coordinate system, in particular the increase of the azimuthal resolution of the computational domain with decreasing radial coordinate.

For the cartesian coordinate system, a very effective formulation of the equations of motion was presented almost 15 years ago by Kim, Moin & Moser in [59]. This formulation has since then been employed in many of the DNS of turbulent wall flows in planar geometries. It consists in the replacement of the continuity and momentum equations written in primitive variables with two scalar equations: one (second-order) for the normal component of vorticity and one (fourth-order) for the normal component of velocity, much as the Orr–Sommerfeld and Squire decomposition of linear stability problems. In this way pressure disappears from the equations, and the two wall-parallel velocity components are easily computed (through the continuity equation and the definition of vorticity) when a Fourier expansion is adopted for the homogeneous directions. This method has been extended to the cylindrical geometry in [99] and will be briefly reviewed in the following.

2.2 Formulation of the equations

The non-dimensional Navier-Stokes equations for an incompressible fluid in cylindrical coordinates are:

$$\frac{\partial u}{\partial z} + \frac{1}{r}\frac{\partial (rv)}{\partial r} + \frac{1}{r}\frac{\partial w}{\partial \theta} = 0; \tag{2.1}$$

$$\frac{\partial u}{\partial t} + u\frac{\partial u}{\partial z} + v\frac{\partial u}{\partial r} + \frac{w}{r}\frac{\partial u}{\partial \theta} = -\frac{\partial p}{\partial z} + \frac{1}{Re}\nabla^2 u; \tag{2.2a}$$

$$\frac{\partial v}{\partial t} + u\frac{\partial v}{\partial z} + v\frac{\partial v}{\partial r} + \frac{w}{r}\frac{\partial v}{\partial \theta} - \frac{w^2}{r} = -\frac{\partial p}{\partial r} + \frac{1}{Re}\left(\nabla^2 v - \frac{v}{r^2} - \frac{2}{r^2}\frac{\partial w}{\partial \theta}\right); \tag{2.2b}$$

$$\frac{\partial w}{\partial t} + u\frac{\partial w}{\partial z} + v\frac{\partial w}{\partial r} + \frac{w}{r}\frac{\partial w}{\partial \theta} + \frac{vw}{r} = -\frac{1}{r}\frac{\partial p}{\partial \theta} + \frac{1}{Re}\left(\nabla^2 w - \frac{w}{r^2} + \frac{2}{r^2}\frac{\partial v}{\partial \theta}\right), \tag{2.2c}$$

where the Laplacian operator in cylindrical coordinates takes the form:

$$\nabla^2 = \frac{\partial^2}{\partial z^2} + \frac{1}{r}\frac{\partial}{\partial r}\left(r\frac{\partial}{\partial r}\right) + \frac{1}{r^2}\frac{\partial^2}{\partial \theta^2}, \tag{2.3}$$

and a Reynolds number $Re = U\delta/\nu$ is selected by choosing the appropriate reference dimension δ and velocity U.

To close the differential problem an initial condition for all the fluid variables should be specified, and suitable boundary conditions have to be chosen. Periodic boundary conditions are used for the azimuthal direction, as well as for the axial direction, whereas the no-slip condition is considered at the walls.

The periodicity assumption permits to write a variable f as

$$f(z, r, \theta, t) = \sum_{\alpha, m} \hat{f}(r, t) e^{i\alpha z} e^{im\theta},$$

where the hat indicates the Fourier component of the transformed variable and the symbols α and m denote the axial and azimuthal wavenumbers, respectively. By defining $k^2 = (m/r)^2 + \alpha^2$, and by introducing the Chandrasekhar [22] notation:

$$D_1(f) = \frac{\partial f}{\partial r}; \qquad D_*(f) = \frac{\partial f}{\partial r} + \frac{f}{r}, \tag{2.4}$$

the Fourier-transformed Laplacian operator (2.3) can be written in the more compact form:

$$\nabla^2 = D_* D_1 - k^2.$$

The transformed equations are:

$$i\alpha\hat{u} + D_*(\hat{v}) + \frac{im}{r}\hat{w} = 0; \tag{2.5}$$

$$\frac{\partial \hat{u}}{\partial t} = -i\alpha\hat{p} + \frac{1}{Re}\left(D_* D_1(\hat{u}) - k^2\hat{u}\right) + \widehat{HU}; \tag{2.6a}$$

$$\frac{\partial \hat{v}}{\partial t} = -D_1(\hat{p}) + \frac{1}{Re}\left(D_1 D_*(\hat{v}) - k^2\hat{v} - \frac{2im}{r^2}\hat{w}\right) + \widehat{HV}; \tag{2.6b}$$

$$\frac{\partial \hat{w}}{\partial t} = -\frac{im}{r}\hat{p} + \frac{1}{Re}\left(D_1 D_*(\hat{w}) - k^2\hat{w} + \frac{2im}{r^2}\hat{v}\right) + \widehat{HW}. \tag{2.6c}$$

In these expressions, the nonlinear convective terms have been grouped under the following definitions:

$$\widehat{HU} = -i\alpha\widehat{uu} - D_*(\widehat{uv}) - \frac{im}{r}\widehat{uw}; \tag{2.7a}$$

$$\widehat{HV} = -i\alpha\widehat{uv} - D_*(\widehat{vv}) - \frac{im}{r}\widehat{vw} + \frac{1}{r}\widehat{ww}; \tag{2.7b}$$

$$\widehat{HW} = -i\alpha\widehat{uw} - D_1(\widehat{uw}) - \frac{im}{r}\widehat{ww} - \frac{2}{r}\widehat{vw}. \tag{2.7c}$$

2.3 Equation for the radial vorticity component

The wall-normal (radial) component of the vorticity vector, which we shall indicate with η, is defined as

$$\eta = \frac{1}{r}\frac{\partial u}{\partial \theta} - \frac{\partial w}{\partial z},$$

and, after transforming in Fourier space, it is given by:

$$\hat{\eta} = \frac{im}{r}\hat{u} - i\alpha\hat{w}. \tag{2.8}$$

By multiplying equation (2.6a) times im/r and subtracting equation (2.6c) times $i\alpha$, and by means of the relations (2.4) it is possible to write the following second-order equation for $\hat{\eta}$:

$$\frac{\partial \hat{\eta}}{\partial t} = \frac{1}{Re}\left(D_1 D_*(\hat{\eta}) - k^2 \hat{\eta} + 2\frac{im}{r^2} D_1(\hat{u}) + 2\frac{m\alpha}{r^2}\hat{v} \right) + \frac{im}{r}\widehat{HU} - i\alpha \widehat{HW}. \tag{2.9}$$

We note that equation (2.9) does not contain the pressure terms, because of the nabla vector properties. The numerical solution of equation (2.9) requires an initial condition for $\hat{\eta}$, which can be computed from the initial condition for the velocity field. The periodic boundary conditions in the homogeneous directions are automatically satisfied thanks to the Fourier transform, whereas the no-slip condition for the velocity vector translates in $\hat{\eta} = 0$ to be imposed at the two walls at $r = \mathcal{R}_i$ and $r = \mathcal{R}_o$.

2.4 Equation for the radial velocity component

The elimination of the pressure-related term in equation (2.6b) is a little cumbersome, since it requires pressure to be written as a function of velocity. After some algebra and by using the time derivative of the continuity equation (2.5), the following expression for $\hat{p}$ is obtained:

$$\hat{p} = -\frac{1}{Re}\frac{1}{k^2}\left[k^2 D_*(\hat{v}) - D_* D_1 D_*(\hat{v}) - 2\frac{m^2}{r^3}\hat{v} + 2\frac{im}{r^2} D_1(\hat{w}) - 2\frac{im}{r^3}\hat{w} \right] + \\ -\frac{1}{k^2}\left[\frac{\partial D_*(\hat{v})}{\partial t} + i\alpha \widehat{HU} + \frac{im}{r}\widehat{HW} \right].$$

This expression for $\hat{p}$ can now be differentiated with respect to the radial coordinate, and then substituted into equation (2.6b) to get rid of $\hat{p}$ altogether. Eventually, the fourth-order equation for $\hat{v}$ emerges in the final form:

$$\frac{\partial}{\partial t}\left[\hat{v} - D_1\left(\frac{1}{k^2} D_*(\hat{v}) \right) \right] = \frac{1}{Re} D_1 \left\{ \frac{1}{k^2}\left[k^2 D_*(\hat{v}) - D_* D_1 D_*(\hat{v}) - 2\frac{m^2}{r^3}\hat{v} + \\ 2\frac{im}{r^2} D_1(\hat{w}) - 2\frac{im}{r^3}\hat{w} \right] \right\} + \frac{1}{Re}\left(-k^2\hat{v} + D_1 D_*(\hat{v}) - 2\frac{im}{r^2}\hat{w} \right) + \\ D_1\left[\frac{1}{k^2}\left(i\alpha\, \widehat{HU} + \frac{im}{r}\widehat{HW} \right) \right] + \widehat{HV}. \tag{2.10}$$

This scalar equation can be solved numerically provided an initial condition for $\hat{v}$ is known. The periodic boundary conditions in the homogeneous directions are automatically satisfied thanks to the Fourier transform, whereas the no-slip condition for the velocity vector immediately translates in $\hat{v} = 0$ to be imposed at the two walls. The continuity equation written at the two walls makes evident that the additional two boundary conditions required for the solution of (2.10) are $D_1(\hat{v}) = 0$ at $r = \mathcal{R}_i$ and $r = \mathcal{R}_o$.

2.5 Velocity components in the homogeneous directions

For computing the nonlinear terms and their spatial derivatives, one needs to know the velocity components $\hat{u}$ and $\hat{w}$ in the homogeneous directions at a given time by knowing $\hat{v}$ and $\hat{\eta}$. By using the definition definition (2.8) of $\hat{\eta}$ and the continuity equation (2.5) written in Fourier space, a 2×2 algebraic system can be written for the unknowns $\hat{u}$ and $\hat{w}$; its analytical solution reads:

$$\begin{cases} \hat{u} = \dfrac{1}{k^2}\left(i\alpha D_*(\hat{v}) - \dfrac{im}{r}\hat{\eta} \right) \\ \hat{w} = \dfrac{1}{k^2}\left(i\alpha\hat{\eta} + \dfrac{im}{r} D_*(\hat{v}) \right) \end{cases} \tag{2.11}$$

When $k^2 = 0$ the system (2.11) is singular. By applying the averaging operator

$$\tilde{f}(r,t) = \frac{1}{L_z}\frac{1}{l_\theta}\int_0^{L_z}\int_0^{l_\theta} f(z,r,\theta,t)\ \mathrm{d}z\mathrm{d}\theta,$$

on equations (2.2a) and (2.2c), the proper equations for the mean motion can be written as

$$\frac{\partial\tilde{u}}{\partial t} = \frac{1}{Re} D_* D_1\left(\tilde{u}\right) - D_*\left(\widetilde{uv}\right) + f_z;$$

$$\frac{\partial\tilde{w}}{\partial t} = \frac{1}{Re} D_1 D_*\left(\tilde{w}\right) - D_1\left(\widetilde{uw}\right) - \frac{2}{r}\widetilde{vw} + f_\theta.$$

In these expressions, f_z and f_θ are the forcing terms needed to force the flow through the channel against the viscous resistance of the fluid.

2.6 Spatial discretization in the homogeneous directions

As a consequence of the hypothesis of periodicity, the unknown functions are expanded in truncated Fourier series in the homogeneous directions. For example the radial component v of the velocity vector is represented as:

$$v(z,r,\theta,t) = \sum_{h=-nz/2}^{+nz/2} \sum_{\ell=-n\theta/2}^{+n\theta/2} \hat{v}_{h\ell}(r,t) e^{i\alpha z} e^{im\theta} \tag{2.12}$$

where:

$$\alpha = \frac{2\pi h}{L_z} = \alpha_0 h; \qquad m = \frac{2\pi \ell}{l_\theta} = m_0 \ell$$

Here h and ℓ are integer indexes corresponding to the axial and azimuthal direction respectively, and α_0 and m_0 are the fundamental wavenumbers in these directions, defined in terms of the axial length L_z of the computational domain and its azimuthal extension l_θ, expressed in radians.

2.7 Compact finite-differences schemes

Compact finite-differences (hereinafter FD) schemes are used to discretize the differential operators by enjoying quasi-spectral resolution (see [65]). The main characteristic of a compact FD scheme can be most easily understood by thinking of a standard FD formula in Fourier space as a polynomial interpolation of a transcendental function, with the degree of the polynomial corresponding to the formal order of accuracy of the FD formula [115]. Compact schemes improve the interpolation by replacing the polynomial with a ratio of two polynomials, i.e. with a rational function. This obviously increases the number of available coefficients, and moreover gives control over the behavior at infinity (in frequency space) of the interpolant, whereas a polynomial necessarily diverges. This allows a compact FD formula to approximate a differential operator in a wider frequency range, thus achieving resolution properties similar to those of spectral schemes [65].

As an explicative example, we will illustrate the method proposed by Thomas [115] by considering a fourth-order one-dimensional ordinary differential equation, linear for simplicity, in the form:

$$D_4(a_4 f) + D_2(a_2 f) + D_1(a_1 f) + a_0 f = g, \tag{2.13}$$

where the coefficients $a_i = a_i(r)$ are arbitrary functions of the independent variable r, and $g = g(r)$ is a known right-hand side and $D_p = \partial^p/\partial r^p$.

Let us moreover suppose that a differential operator, for example D_4, is approximated in frequency space as the ratio of two polynomials, say $\mathcal{D}_4$ and $\mathcal{D}_0$. Polynomials like $\mathcal{D}_4$ and $\mathcal{D}_0$ have their counterpart in physical space, and d_4 and d_0 are the corresponding FD operators. The key point is to impose that *all* the differential operators appearing in the example equation (2.13) admit a representation such as the preceding one, in which the polynomial $\mathcal{D}_0$ at the denominator remains *the same*.

Equation (2.13) can thus be recast in the new, discretized form:

$$d_4\left(a_4 f\right) + d_2\left(a_2 f\right) + \ldots + d_1\left(a_1 f\right) + d_0\left(a_0 f\right) = d_0\left(g\right),$$

and this allows us to use explicit FD formulas, provided the operator d_0 is applied to the right-hand side of our equations. We note that, owing to the absence of the third-derivative operator from equation (2.13), compact fourth-order accurate schemes at the cost of explicit schemes can be used.

However, the particular nature of equations (2.9) and (2.10) does not permit to obtain straightforwardly a fourth-order accuracy over a five unevenly spaced points stencil (see [75]), as their cartesian counterpart do. In fact three main points make the extension difficult: (1) third-derivative terms are present in equation (2.10), thus preventing the possibility of finding explicit compact schemes; (2) both equations (2.9) and (2.10) do contain r-dependent coefficients which are not in the innermost position; (3) equation (2.10) for $\hat{v}$ is a fourth-order equation, yet the highest differential operator is not D_4, but DD_*DD_*.

The first problem can be solved by using the continuity equation (2.5), which allows the first radial derivative of $\hat{v}$ to be substituted with terms not containing radial derivatives:

$$D_*(\hat{v}) = -i\alpha\hat{u} - \frac{im}{r}\hat{w}.$$

The second problem, though cumbersome for the algebra handled, can be faced with a straightforward strategy by applying repeated integrations by parts to shift the r-dependent coefficients in the innermost position, i.e. by repeatedly performing the following substitutions:

$$aD_1(f) = D_1(af) - D_1(a)f; \qquad aD_*(f) = D_*(af) - D_1(a)f,$$

where a indicates the generic r-dependent coefficient. Finally, the presence of fourth order terms like DD_*DD_* instead of D_4, simply reflects in a more complicated formula for the derivation of the FD coefficients.

2.8 Time discretization

The two equations (2.9) and (2.10) are coupled since (2.9) contains $\hat{v}$. Provided the nonlinear terms are advanced in time explicitly, equations (2.9) and (2.10), though coupled, can be solved sequentially at each time step, by solving first (2.10) for $\hat{v}$ and then (2.9) for $\hat{\eta}$.

Time integration of the equations is performed by a partially-implicit method, implemented to reduce the memory requirements of the code to a minimum, by exploiting the finite-difference discretization of the wall-normal direction. The use of a partially-implicit scheme is a common approach in DNS [59]: the explicit part of the equations can benefit from a higher-accuracy scheme, while the stability-limiting viscous part is subjected to an implicit time advancement, thus relieving the stability constraint on the time-step size Δt.

We can write the equations (2.9) and (2.10), for a generic wavenumber pair (h, ℓ), in a short-handed form of the type:

$$\frac{\partial}{\partial t}\widehat{unkn}_{h\ell} = \widehat{expl}_{h\ell} + \widehat{impl}_{h\ell}$$

where $\widehat{unkn}_{h\ell}$ represents the unknowns of the problem, namely the left-hand side of equations (2.9) and (2.10), $\widehat{expl}_{h\ell}$ is the explicit part, which consist of nonlinear terms plus some additional viscous curvature terms (see [98] for more details), and $\widehat{impl}_{h\ell}$ is the implicit part.

By following [86], we use an explicit third-order, low-storage Runge-Kutta method for the integration of the explicit part of the equations, and an implicit second-order Crank-Nicolson scheme is used for the implicit part, which altogether result in

$$\frac{\widehat{unkn}_{h\ell}^{\,n+p/3} - \widehat{unkn}_{h\ell}^{\,n+(p-1)/3}}{\Delta t} = \sigma_p \left(\widehat{impl}_{h\ell}^{\,n+p/3} + \widehat{impl}_{h\ell}^{\,n+(p-1)/3} \right) + \\ + \left(\tau_p \widehat{expl}_{h\ell}^{\,n+(p-1)/3} + \xi_p \widehat{expl}_{h\ell}^{\,n+(p-2)/3} \right) \quad (2.14)$$

with $p = 1, 2, 3$, and Δt the time advancement. The $\boldsymbol{\sigma}, \boldsymbol{\tau}, \boldsymbol{\xi}$ coefficient vectors can be expressed in a single matrix of the form

$$\left(\boldsymbol{\sigma}^T | \boldsymbol{\tau}^T | \boldsymbol{\xi}^T \right) = \begin{pmatrix} 4/15 & 8/15 & 0 \\ 1/15 & 5/12 & -17/60 \\ 1/6 & 3/4 & -5/12 \end{pmatrix}.$$

The procedure to solve these discrete equations is made by two distinct steps. In the first step, the right-hand sides (hereinafter RHS) corresponding to the explicitly-integrated parts part have to be assembled. At a given time, the Fourier coefficients of the variables are represented at different r positions; hence the velocity products can be computed through inverse/direct Fast Fourier Transform (hereinafter FFT) in wall-parallel planes. Their spatial derivatives are then computed: spectral accuracy can be achieved for wall-parallel derivatives, whereas the FD compact schemes are used in the wall-normal direction. These spatial derivatives are eventually combined with values of the RHS at previous time levels. The whole r range, from one wall to the other, must be considered.

The second step involves, for each α, m pair, the solution of a set of two ordinary differential equations (ODEs), derived from the implicitly integrated viscous terms, for which the RHS is now known. A FD discretization of the radial differential operators produces two real banded matrices, in particular pentadiagonal matrices when a 5-point stencil is used. The solution of the resulting two linear systems gives $\hat{\eta}_{h\ell}^{n+1}$ and $\hat{v}_{h\ell}^{n+1}$, and then the homogeneous velocity components $\hat{u}_{h\ell}^{n+1}$ and $\hat{w}_{h\ell}^{n+1}$ can be computed by solving system (2.11) for each wavenumber pair. For each α, m pair, the solution of the two ODEs requires the simultaneous knowledge of their RHS in all r positions. The whole α, m space must be considered. In the $\alpha - m - r$ space the first step of this procedure proceeds per wall-parallel planes, while the second one proceeds per wall-normal lines.

2.9 The parallel strategy

Being the calculations executed in parallel by p computing machines (nodes), data necessarily reside on these nodes in a distributed manner, and communication between nodes takes place. Therefore, the main design goal is to keep the required amount of communication to a minimum.

The FD discretization in the r direction permits to distribute the unknowns in wall-parallel slices and to carry out the two-dimensional inverse and direct FFT locally to each machine. Moreover, thanks to the locality of the FD operators, the communication required to compute wall-normal spatial derivatives of velocity products is small, since data transfer is needed only at the interface between contiguous slices.

The arrangement of the data across the machines is schematically shown in figure 2.1: each machine holds all the streamwise and spanwise wavenumbers for nr/p contiguous r positions. The FFT in the homogeneous directions do not require communication at all, while the radial derivatives needed for the evaluation of the RHS require a small amount of communication at the interface between contiguous slices.

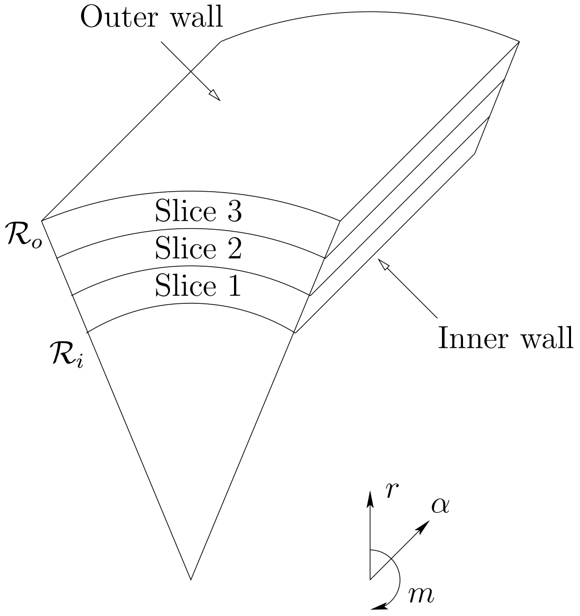

Figure 2.1: Arrangement of data in wall-parallel slices across the channel, for a parallel execution with $p = 3$ computing nodes.

The critical part of the procedure lies in the second half of the time-step advancement, i.e. the solution of the set of two linear systems, one for each h, ℓ pair, and the recovery of the planar velocity components: the necessary data just happen to be spread over all the p machines. It is relatively easy to avoid a global transpose, by solving each system in a *serial* way across the machines: adopting a LU decomposition of the pentadiagonal distributed matrices, and a subsequent sweep of back-substitutions, only a few coefficients at the interface between two neighboring nodes must be transmitted. The global amount of communication remains very low and, at the same time, local between nearest neighbors only. The problem here is to obtain a reasonably high parallel efficiency: if a single system had to be solved, the computing machines would waste most of their time waiting for the others to complete their task. In other words, with the optimistic assumption of infinite communication speed, the total wall-clock time would be simply equal to the single-processor computing time. The key observation to obtain high parallel performance is that the number of linear systems to be solved at each time (sub)step is very large, i.e. $(nz + 1)(n\theta + 1)$ which is at least 10^4 and sometimes much larger in typical DNS calculations [32]. This allows the solution of the linear systems to be efficiently pipelined.

While a computer program based on the numerical method described heretofore can be easily run on a general-purpose cluster of machines, connected through a network in a star topology with a switch, for maximum efficiency a dedicated computing system can be specifically designed and built on top of the parallel algorithm described above. An example of a such a dedicated system, made by 10 SMP nodes, has been built at the Dipartimento di Ingegneria Aerospaziale del Politecnico di Milano. Each node carries 2 Intel Xeon 2.66 GHz CPU, and 512MB of 266 MHz SDRAM; the interconnections are two onboard Gigabit Ethernet cards. This is the machine where most of the computations have been carried out. For some smaller computations we have used the first prototype of such a dedicated system, composed of 8 SMP Personal Computers: each node is equipped with 2 Pentium III 733MHz CPU and 512MB of 133MHz SDRAM. The nodes are connected to each other by two cheap 100MBits Fast Ethernet cards.

Finally, we notice that the cylindrical version of the computer code shares with its cartesian counterpart the basic structure, and the high computational efficiency when executed in serial or parallel mode (see [99]). The differences in source code are actually very limited, allowing to re-use most of the numerical routines.

2.10 Validation

2.10.1 Laminar TCF

To the purpose of validating the numerical method in the cylindrical geometry, we present here a few results concerning both TCF and DF. Further comparisons of results obtained from our DNS code and results available in literature can be found in the following chapters. For the TCF numerical simulations have been conducted in the laminar regime for various dimension of the radius ratio, η; in fig. 2.2 the computed radial profile of the azimuthal velocity $w(r)$ is presented for $R_i = 2, R_o = 0$ and for two different η : 0.925 and 0.75.

Both the velocity profiles fit well the laminar solution $w^l(r)$, given by equation (1.1), thus no visible difference can be appreciated between the computed solutions and the analytical solutions. The relative error E between the computed and the laminar solution:

$$E = \max_{\mathcal{R}_i < r < \mathcal{R}_o} \left| \frac{w(r) - w^l(r)}{w_{max}} \right| \tag{2.15}$$

where w_{max} is the maximum of the azimuthal velocity, is plotted in fig. 2.3 for $\eta = 0.925$. The value of E is low and, most important, it decays as a fourth-order power function of the number of points in the radial direction nr^{-4}, which confirms the asymptotic order of accuracy of the numerical method.

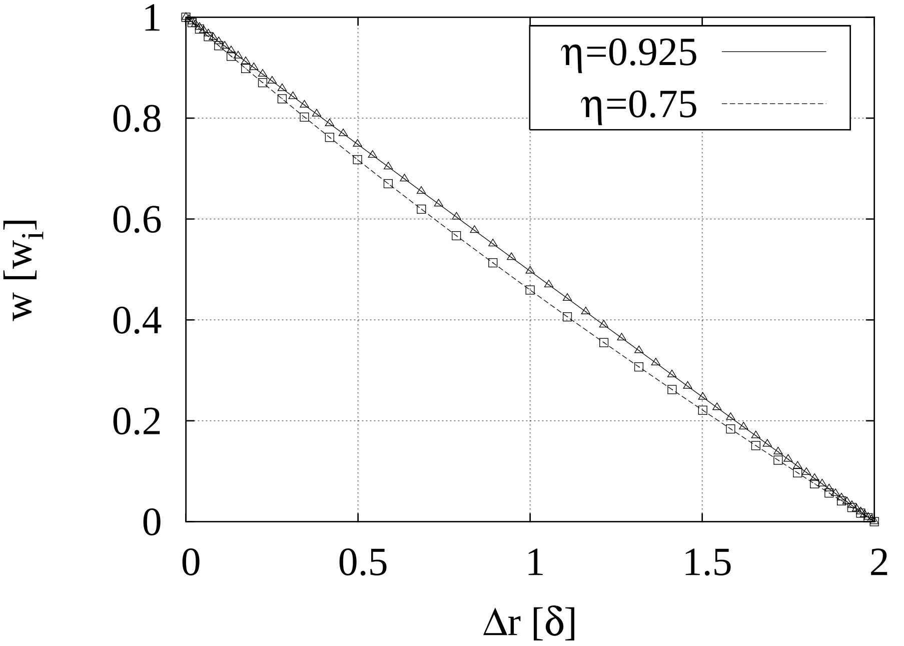

Figure 2.2: Laminar solution $w^l(r)$ for the TCF with $\Omega = 0$. Analytical solution: continuos line, $\eta = 0.925$, and dashed line, $\eta = 0.75$. Computed solution: $\triangle$ for $\eta = 0.925$ (with $nr = 64$), and $\square$ for $\eta = 0.75$ (with $nr = 32$).

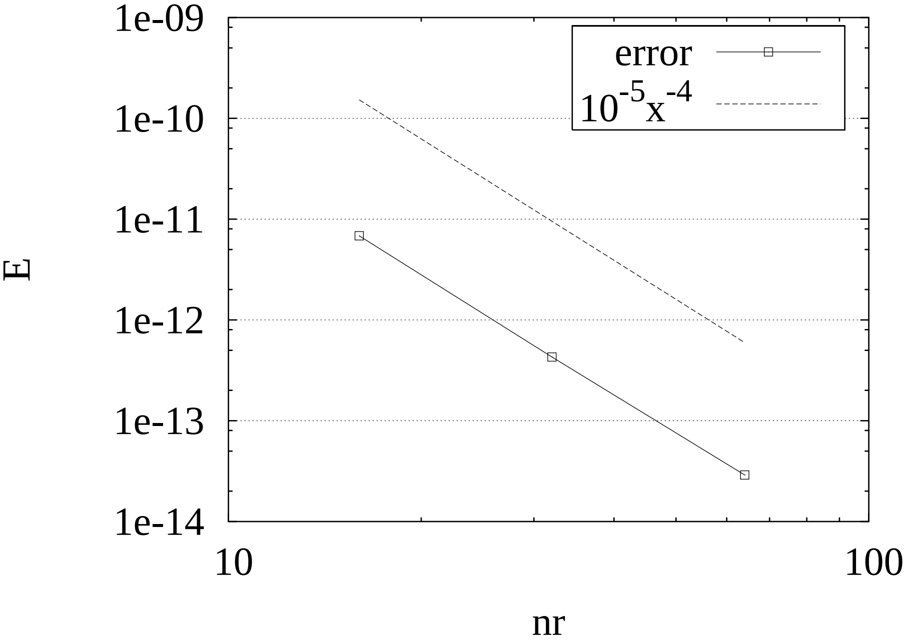

Figure 2.3: Relative error as a function of nr for a TCF with $\Omega = 0, \eta = 0.975$.

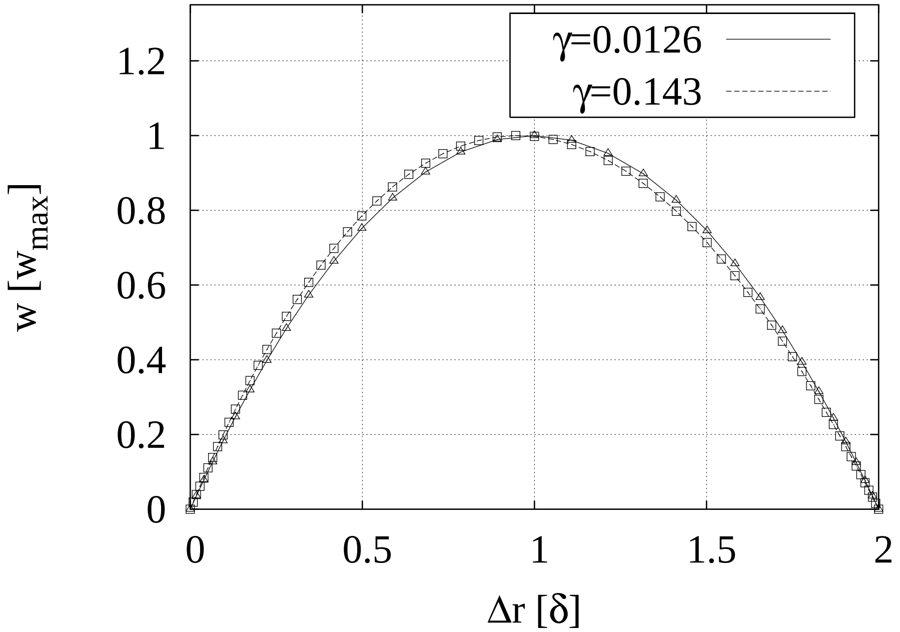

Figure 2.4: Laminar solution $w^l(r)$ for the DF with $P_\theta/\mu = 2$. Analytical solution: continuous line, $\gamma = 0.0126$, and dashed line, $\gamma = 0.143$. Computed solution: $\triangle$ for $\gamma = 0.0126$ (with $nr = 32$), and $\square$ for $\gamma = 0.143$ (with $nr = 64$).

2.10.2 Laminar DF

The same kind of validation is carried out for the DF with a ratio between the pressure gradient and the viscosity equal to two, i.e. $P_\theta/\nu = 2$. Both cases of large ($\gamma = 0.0126$) and small ($\gamma = 0.143$) curvature have been tested; the azimuthal velocity profile $w(r)$, obtained from the numerical simulations are plotted in fig. 2.4 and compared with the laminar solution $w^l(r)$, given by equation (1.2). The agreement between the velocity profiles is fairly good; the relative error, plotted in fig. 2.5 for $\gamma = 0.143$, shows both small values and a fourth-order decay.

2.10.3 TV and WTV

The numerical method is also assessed by comparing the obtained values of $R_{i,cr}$ with those available in literature for both large-gap and small-gap geometries. A periodic box with $L_z = 2d$, $l_\theta = \pi$ is considered; 32 and 16 modes in axial and azimuthal directions are used, whereas 33 points are used in radial direction. The initial field consists of fluid at rest with small super-

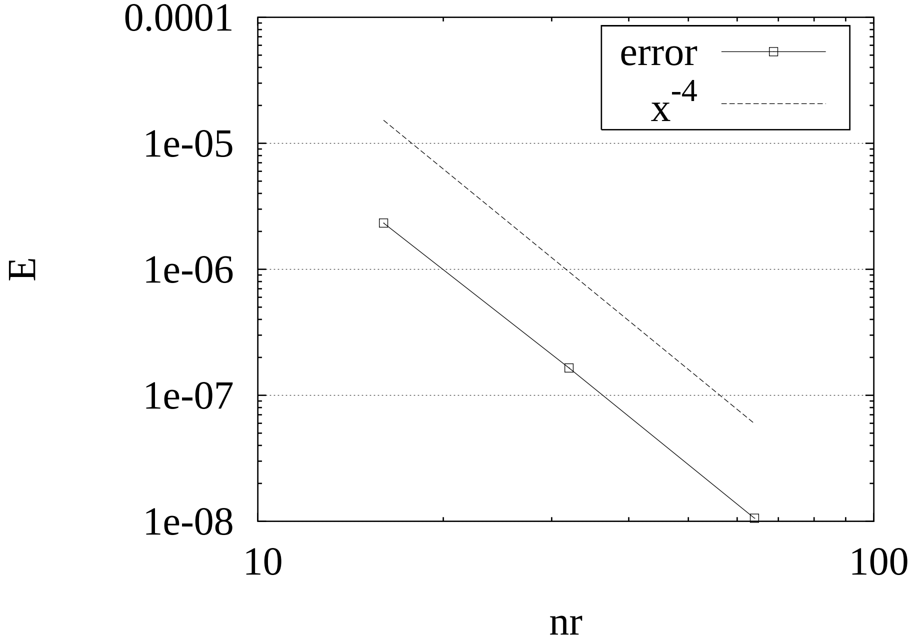

Figure 2.5: Relative error as a function of nr for a DF with $P_\theta/\mu = 2, \gamma = 0.143$.

imposed disturbances, $\mathcal{O}(10^{-3})$, on high spatial modes. After a settlement time, the solution, for low values of the Reynolds number, reaches a steady regime. Other grids and different initial conditions have been considered too: the results have been found to differ only for the time required for the settlement of the final solution.

For a large-gap geometry with $\eta = 0.5$ our simulations provide a $R_{i,cr}$ in the range $]68.2, 68.4[$, in excellent agreement with the value of 68.2 calculated through numerical simulations by [42],[87] and with the value of 68.4 measured in experiments by [103]. The small-gap geometry with $\eta = 0.95$ provides good results too; a $R_{i,cr}$ in the range $]184, 186[$ is calculated against a value of 185 by [87]. Moreover, the value of the torque [34]:

$$G(r) = \mu 2\pi r^2 H \left[\frac{\partial w(r)}{\partial r} - \frac{w(r)}{r} \right] \tag{2.16}$$

evaluated at the inner wall has been calculated in both geometries. In table 2.1 the values of $G(\mathcal{R}_i)$, for various R_i, are compared with those calculated by [42], in a large-gap geometry ($\eta = 0.5$) and with the experimental results of [34] for a small-gap geometry ($\eta = 0.95$). The agreement is fairly good in the large-gap geometry, and it is satisfactory (around one per cent), considering

$\eta = 0.5$	$G(\mathcal{R}_i)[\mu w_i \mathcal{R}_i H]$		$\eta = 0.95$	$G(\mathcal{R}_i)[10^{-7}Nm]$		
R_i	ref. [42]	here	R_i	ref. [34]	here	% error
60.0	16.7551	16.7546	150	94	96.58	2.6
68.0	16.7551	16.7546	184	118	118.47	0.4
69.0	16.9347	16.9370	186	121.3	120.10	1.0
72.5	17.6752	17.6758	188	124	126.30	1.8
80.0	19.0527	19.0514	195	140	142.45	1.7

Table 2.1: Steady TCF: torque, as in eq. (2.16), at the inner cylinder, for different values of R_i. In the large-gap geometry ($\eta = 0.5$) the comparison is with the numerical results by [42]. For the small-gap geometry ($\eta = 0.95$) the comparison is with the experimental results by [34].

the coarse mesh used, in the small-gap case. Preliminary simulations in the wavy regime have been conducted too. A DNS with a $L_z = 2d, l_\theta = 2\pi$ periodic box and with $(nz, n\theta, nr) = (64, 32, 32)$ has been conducted for values of the Reynolds numbers of $(R_i, R_o) = (255, -55)$. The results of the simulations show a pair of wavy vortices, with azimuthal wavenumber $m = 2$ and a characteristic period of rotation $T = 117\delta/w_i$; the non-dimensional rotational velocity $s = 2\pi/(mT\Omega_i)$ is 0.054, in agreement with the results of 0.05 derived from the graphs presented by [107].

2.11 Performance

A brief evaluation of the performance of the numerical method is now given by referring to [99] for more detailed analysis. We present here data obtained with the cartesian counterpart of the present code. The performance evaluated for the cartesian code applies for the cylindrical code too, in particular concerning the properties of the PLS parallel method. For a problem of the same computational size, the CPU overhead of the cylindrical version compared to the cartesian case is approximately 40%. Pre-computing the r-dependent coefficients increases memory requirements by about 13%. In the following, instead of the $(nz, n\theta, nr)$ triad already seen for the cylindrical code, we will consider the streamwise and spanwise modes nx and nz, respectively, and the wall normal discretization points ny, of the cartesian geometry.

The amount of required RAM is dictated by the number and the size of the three-dimensional arrays, and it is typically reported (see [59],[55]) to be no less than 7 $nx \times ny \times nz$ floating-point variables. Owing to the implementation of the time advancement procedure, which takes advantage of the finite-difference discretization of the wall-normal derivatives, the present code requires a memory space of 5 $nx \times ny \times nz$ floating-point variables, plus workspace and two-dimensional arrays. For example a simulation with $nx = ny = nz = 128$ takes only 94 MBytes of RAM (using 64-bit floating-point variables).

In a parallel run the memory requirement can be subdivided among the computing machines. With $p = 2$ the same 128^3 case runs with 53 MBytes of RAM (note that the amount of RAM is slightly larger than one half of the $p = 1$ case, because of the duplication of boundary planes).

As far as CPU efficiency is concerned, without special optimization the 128^3 test case mentioned above requires 42.8 CPU seconds for the computation of a full three-sub-steps Runge-Kutta temporal step on a single Pentium III 733MHz processor. Internal timings show that the direct/inverse two-dimensional FFT routines take the largest part of the CPU time, namely 56%. The calculation of the RHS of the two governing equations (where wall-normal derivatives are evaluated) takes 25% of the total CPU time, the solution of the linear systems arising from the implicit part around 12%, and the calculation of the planar velocity components 3%. The time-stepping scheme takes 3% and computing a few runtime statistics requires an additional 1% of the CPU time.

The parallel (distributed-memory) performance of the code is illustrated in fig. 2.6, where speedup ratios are reported as a function of the number of computing nodes. We define the speedup factor as the ratio of the actual wall-clock computing time t_p obtained with p nodes and the wall-clock time t_1 required by the same computation on a single node:

$$S(p) = \frac{t_p}{t_1}.$$

The maximum or ideal speedup factor S_i that we can expect with our PLS algorithm, corresponding to the assumption of infinite communication speed, is less than linear, and can be estimated with the formula:

$$S_i(p) = p\left(1 - \frac{4(p-1)}{ny}\right), \tag{2.17}$$

where the factor 4 accounts for the two wall-parallel planes duplicated at each side of interior slices. Equation (2.17) reduces to a linear speedup when $ny \to \infty$ for a finite value of p. A quantitative evaluation of the function (2.17) for typical values of $ny = \mathcal{O}(100)$ shows that the maximum achievable speedup is nearly linear as long as the number of nodes remains moderate, i.e. $p < 10$.

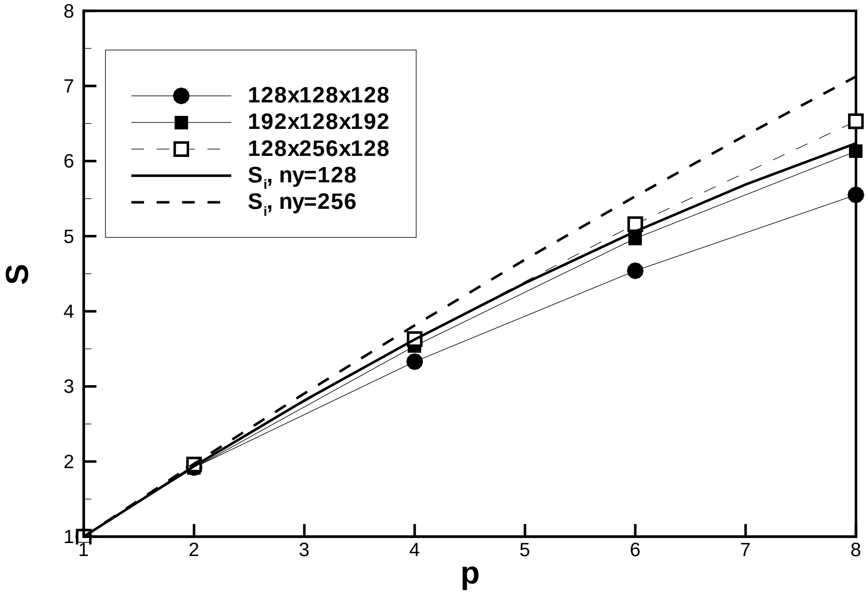

Figure 2.6: Measured speedup on the Pentium III-based machine as a function of the number p of computing nodes. Thick lines are the ideal speedup S_i from eq. (2.17) for $ny = 128$ (continuous line) and $ny = 256$ (dashed line). From [99].

The maximum possible speedup S_i is shown with thick lines. S_i approaches the linear speedup for large ny, being reasonably high as long as p remains small compared to ny: with $p = 8$ it is 6.25 for $ny = 128$ and 7.125 for $ny = 256$. Notwithstanding the commodity networking hardware and the overhead implied by the error-corrected TCP protocol, the actual performance compared to S_i is extremely good, and improves with the size of the computational problem. The case $192 \times 128 \times 192$ is hardly penalized by the time spent for communication, which is only 2% of the total computing time when $p = 8$. The communication time becomes 7% of the total computing time for the larger case of $nx = 128$, $ny = 256$ and $nz = 128$, and is 12% for the worst (i.e. smallest) case of 128^3, which requires 7.7 seconds for one time step on our machine, with a speedup of 5.55.

2.12 Final remarks

The numerical method reviewed here has proven to be capable of achieving high efficiency by using commodity hardware. Many elements of the code concur to the cause, in particular: (1) the compact FD approach, (2) the v, η formulation, (3) the parallel method, (4) the possibility of using a low-cost, dedicated system.

In fact, the choice of compact finite differences of fourth-order accuracy, while retaining a large part of the accuracy enjoyed by spectral schemes, is crucial to the development of the parallel strategy, which exploits the locality of the FD operators to largely reduce the amount of inter-node communication. Moreover, it permits a minimal storage space of 5 variables per point, compared to the commonly reported minimum of 7 variables per point. Important is also the formulation of the cylindrical Navier–Stokes equations in terms of radial velocity and radial vorticity, which permits to solve them numerically with high computational efficiency.

Besides, the parallel method, based on the pipelined solution of the linear systems (PLS) arising from the discretization of the viscous terms, permit to subdivide the computing effort, as well as the required memory space, among a number of low-cost computing nodes. Moreover, a dedicated system can be easily built, using commodity hardware and hence at low cost, to run a computer code based on the PLS method.

CHAPTER 3

TEMPORAL MODULATION OF TAYLOR-COUETTE FLOW

In the present chapter the flow field in the gap between an inner cylinder, moving with a time dependent law, and an outer steady cylinder is investigated via direct numerical simulations. A large-gap geometry is considered and Reynolds numbers characterized by the presence of TV and WTV are analysed.

3.1 Background

Since the milestone work of Taylor [114], who discovered that an array of pairs of counter-rotating vortices appear as a product of centrifugal instability above a critical value of the Reynolds number, large efforts of the scientific community have been devoted to the comprehension of the behaviour of these vortices, the TV.

The behaviour of these doughnut-like structures is considered to be pivotal for the overall control strategy of the flow, i.e. to enhance the mass transport and mixing properties. Many control strategies have been studied, ranging from the shape modification of the cylinders (hourglass geometry [122], wavy geometry [100]), to the axial movement of the inner cylinder (see [82], [71]), from the superposition of axial flow (see [121], [53]) to the temporal modulation of the azimuthal velocity of the cylinders. In particular, as recently reviewed by Normand [92], the temporal modulation of TCF has been investigated through asymptotic methods [49], experimental studies [35], linear stability combined with Floquét theory [21], and numerical simulations [125].

Here, we consider the last approach and study the flow generated by the co-sinusoidal modulation of the rotational velocity of the inner cylinder

$$\Omega_i(t) = \Omega \cos(\omega t) \tag{3.1}$$

in the case of zero-mean rotation, being the outer cylinder at rest, i.e. $\Omega_o = 0$. As a consequence of (3.1), the inner-cylinder Reynolds number defined in §1.2 is now a time-dependent parameter,

$$R_i(t) = \frac{\Omega \mathcal{R}_i d}{\nu} \cos(\omega t) = R \cos(\omega t).$$

The Navier–Stokes equations in the case of cylinders with infinite axial length admit a solution, which can be written in closed form by means of the modified Bessel functions of order one, I_1 and K_1. The solution is given by (see [21]):

$$w(r,t) = w_i \left[\frac{\eta}{1-\eta^2} \left(\frac{\mathcal{R}_o}{r} - \frac{r}{\mathcal{R}_o} \right) + \frac{\Delta(r, \mathcal{R}_o)}{\Delta(\mathcal{R}_i, \mathcal{R}_o)} \cos(\omega t) \right], \tag{3.2}$$

where $w_i = \Omega \mathcal{R}_i$, $\Delta(r,s) = I_1(\kappa r) K_1(\kappa s) - I_1(\kappa s) K_1(\kappa r)$, $\kappa = \sqrt{i\omega/\nu}$ and $i = \sqrt{-1}$.

Owing to the amplitude of the modulated part, which is not infinitesimal, a perturbation theory cannot be used, however both stability analyses and numerical simulations have shown that, in the low-frequency case, the critical value of the Reynolds number at which TV appear is higher than $R_{i,cr}$, which is the value for the zero-frequency limit. Moreover, when this critical Reynolds number R_0 is reached, the numerical simulations in [125] have shown that two kinds of flow can exist, in dependence of the Reynolds number and the oscillation frequency. In one case, the so-called reversing TV appear: their sense of rotation alternatively changes as the inner cylinder velocity goes from the positive to the negative values, and vice versa; in the other case, a non-reversing modulated flow appears, in which the sense of rotation does not change with the sign of the inner-cylinder velocity. Besides, experiments [95] have shown that, for very high frequencies, TV exist just in a small range of Reynolds numbers and thus a sudden transition to a chaotic flow takes place.

Since the physical nature of this reversing phenomenon is not clear, we investigate these problems with DNS. We chose a large-gap geometry since the TV have a wider domain of existence than in small-gap geometry, as we will see soon in §3.2. As a consequence, the transition between reversing and non-reversing regimes can be observed in wider range of Reynolds numbers. At the same time, the range of considered Reynolds numbers and frequencies will be expanded compared to what is currently available in literature [126], in order to observe the effects of a temporal modulation on the possible insurgence of periodic phenomena.

3.2 The numerical simulations

We chose to focus on a large-gap geometry with $\eta = 0.5$. The reason is related to the relative difference between the critical values of the Reynolds number at which TV and WTV settle, respectively $R_{i,cr}$ and $R_{i,w}$. When η is close to one this relative difference, i.e. $(R_{i,w} - R_{i,cr})/R_{i,cr}$, is small, but increases as η diminishes. For example, in a small-gap geometry with $\eta = 0.883$ (see [2]) the relative range is 0.2, while for $\eta = 0.5$ a value of 6 is obtained.

Since our main interest is the behaviour of a single pair of vortices and not the interaction between many of them, we have chosen an axial length of $L_z = 2d$, which, according to the experimental observations, is the typical axial dimension of a single pair of counter-rotating vortices. As azimuthal dimension we have considered the full angular extension: $l_\theta = 2\pi$. The number of modes chosen for the simulation are $(nz, n\theta) = (32, 16)$; for the radial direction 33 points have been chosen on a non-uniform mesh. Simulations with a finer grid, $(nz, n\theta, nr) = (32, 16, 64)$, have shown no substantial difference. In [125] various axial wavelength have been considered, while in our simulations the axial wavelength $\alpha = 2\pi/L_z$ is fixed at the value π/d.

The initial condition for the $\omega = 0$ case consists of the Couette laminar solution, equation (1.1), with superimposed disturbances of $\mathcal{O}(10^{-3})$ on the higher-frequency spatial modes. When a temporal modulation is considered, the initial condition is the solution of an $\omega = 0$ case at the proper R_i.

3.3 Reversing and non-reversing TV

As mentioned in §2.11, when $\omega = 0$ the computed $R_{i,cr}$ is in the range $]68.2, 68.4[$. As R_i grows beyond $R_{i,cr}$ the TV thrive until the appearance of WTV produced by an Höpf bifurcation. The corresponding $R_{i,w}$ is approximately 480 ([58] reported a value of 475) and the azimuthal wavenumber is $m = 1$.

When a slow modulation is considered the appearance of TV shifts from $R = R_{i,cr}$ to $R = R_0 > R_{i,cr}$: with $\omega \approx 3\nu/d^2$ it is $R_0 \approx 123$, which results in a ratio $R_0/R_{i,cr} \approx 1.78$. This result is in good agreement with the value obtained by Youd, Willis & Barenghi [126], i.e. $R_0/R_{i,cr} \approx 1.755$. The increase in the value of the critical Reynolds number means that the core of the flow does not respond instantaneously to the velocity of the inner wall. Though R ($R_{i,cr} < R < R_0$) is compatible with the existence of TV for the non-modulated case, locally the vortices feel a lower R, and thus decay; when $R > R_0$, however, the vortices have enough energy to survive through the

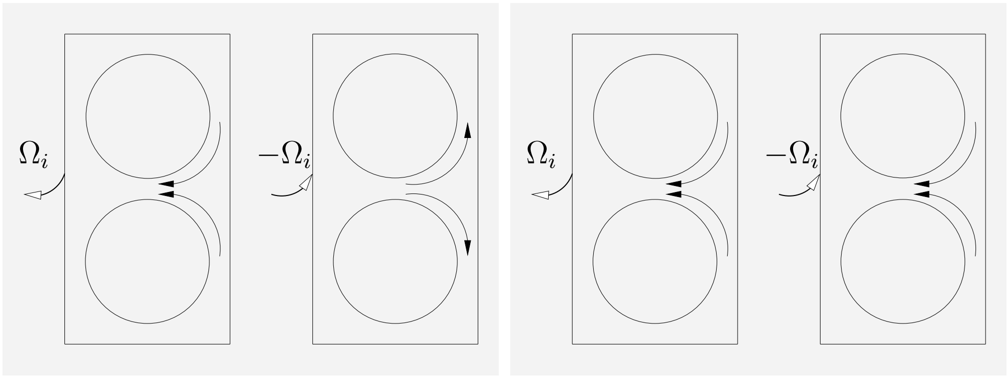

(a) RTV.

(b) NRTV.

Figure 3.1: Reversing and non-reversing TV flow.

whole cycle.

As observed in the numerical study by [125], for $R > R_0$ and low ω a reversible regime exists, for which the sense of rotation of the TV changes as Ω_i passes from positive to negative values, see fig. 3.1(a). This configuration is named reversing TV flow (RTV hereinafter). No particular consideration was given in [125] to the physical significance of the RTV.

In a physical experiment the sense of rotation of the inner cylinder can be reversed by simply viewing the experimental setup upside-down; if one pair of vortices is pushing fluids from the outer towards the inner cylinders in the up orientation, it will continue to do so also in the upside-down view. So the numerical RTV appears as unphysical in experiments, where only non-reversing TV (NRTV hereinafter) are observed, see fig. 3.1(b) .

The explanation of the numerically observed RTV can be given by considering the influence of a (numerical or experimental) perturbation in the selection of the solution of a pitchfork bifurcation problem. By applying a perturbation expansion [30] of the velocity field in the Navier–Stokes equations, the transition of the standard TCF from the laminar solution can be expressed through a nonlinear equation for the amplitude $X(t)$ of the perturbed streamwise velocity field, namely

$$\dot{X} = (R_i - R_{i,cr})X - X^3. \tag{3.3}$$

The equation (3.3) is nonlinear and depends on the parameter R_i. Its steady solution can be found by solving (3.3) for $\dot{X} = 0$. In fig. 3.2 we have sketched these steady solutions: by growing the R_i above its critical value $R_{i,cr}$ we pass from one stable solution, labeled with the number 1 (see

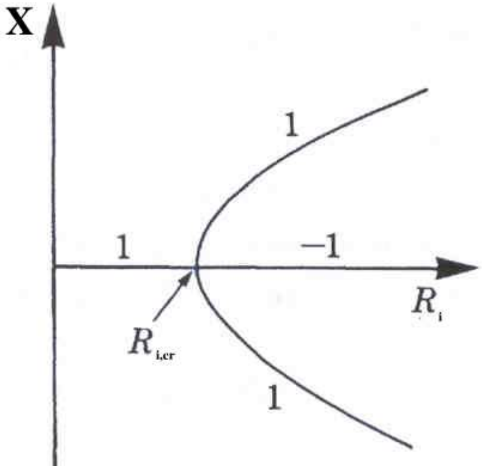

Figure 3.2: State diagram illustrating a pitchfork bifurcation, eq. (3.3), from [8]. The stable branch are labeled with 1, the unstable with −1.

[27]), to three possible solutions: one unstable (label −1) and two stable (label 1). In line of principle, both the stable supercritical branches can be followed by continuously growing R_i from the subcritical solution. Owing to its particular form, this bifurcation is known as pitchfork bifurcation. In physical system perturbations ϵ of some sort (no matter if numerical or experimental in nature) always exist, and (3.3) modifies in:

$$\dot{X} = (R_i - R_{i,cr})X - X^3 + \epsilon. \tag{3.4}$$

The steady solutions to this equation are sketched in fig. 3.3. Now the two branches of the solution are no mores symmetric, and only one can be followed by slowly increasing R_i from $R_i = 0$, while the other can be reached only through jumps. In any case, the non uniqueness feature exists only above a critical value $R_{i,nu}$, to which corresponds a critical point labeled in fig. 3.3 with the index $i = 0$. Roughly speaking, the perturbation selects a particular branch of the solution. Another, not minor, consequence of the presence of a perturbation is that "no precise critical value of R_i exists for the onset of the cellular motion" (as stated in [8]).

In an experimental setup, the experimental perturbation ϵ_e depends on many factors related to the geometry (e.g. lids' movements, the manufacturing process), and is therefore not controllable. Thus, ϵ_e *chooses* the preferred branch which means, roughly, how many vortices appear; however, the chosen branch does not depend on the sense of rotation of the cylinder. In a numerical simulation, we introduce some controllable perturbation ϵ_n to the initial

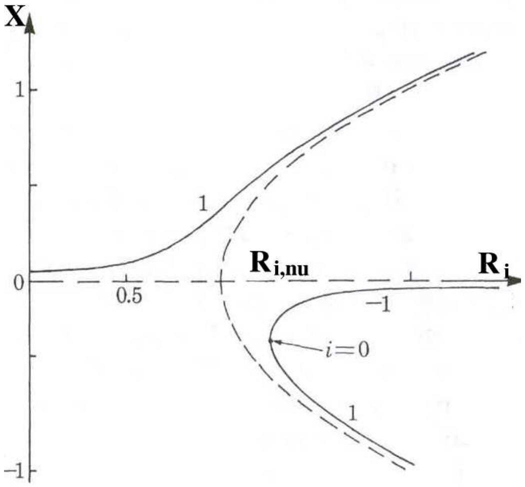

Figure 3.3: State diagram representing a perturbed pitchfork bifurcation, eq. (3.4), from [8] The stable branch are labeled with 1, the unstable with −1, the critical point with 0.

field; without ϵ_n the laminar solution would persist up to high R_i whereas by means of ϵ_n it loses stability and, at the proper value of $R_i > R_{i,cr}$ a particular pair of TV appears. Let us call this pair the A-vortices. We have checked that the same A-vortices are selected in a simulation where both the sense of rotation of Ω_i, and the sign of the initial perturbation ϵ_n are reversed. On the other hand, the reversal of just one of the two parameters Ω_i, ϵ_n produces a pair of vortices which are identical to the A-vortices, but shifted by half a period in the axial direction. This means that, for a given ϵ_n the change from Ω_i to $-\Omega_i$, corresponds to a shift of half a wavelength. Thus, by imposing an initial perturbation ϵ_n, the TV which are properly selected by a given Ω_i switch to their half-a-period twins with the inversion of Ω_i to $-\Omega_i$. As stated above, in experiments the sense of rotation of the TV does not depends on the sense of rotation of Ω_i, *whatever* ϵ_e is considered; so it appears that the numerically observed RTV are the logical counter-part of the experimental NRTV.

To identify the vortices we have decided, following [18], to use the stream-function Ψ, which, for a two-dimensional case, is defined as:

$$v(r,z) = \frac{1}{r}\frac{\partial \Psi(r,z)}{\partial z}, \qquad u(r,z) = -\frac{1}{r}\frac{\partial \Psi(r,z)}{\partial r}, \tag{3.5}$$

and can be extended to the three-dimensional case, by simply taking into account the azimuthal dependence. In fact, in the 3D case $\Psi(r,z,\theta)$ represents “the intersection of the physical stream-surfaces with a θ-meridional plane” (see [18]). By using the axial-periodicity of the flow, the Fourier transformed Ψ can be obtained as

$$\hat{\Psi}_{h\ell}(r,t) = (i\alpha)^{-1} r \hat{v}_{h\ell}(r,t).$$

As a representative example of RTV, a full period $T = 2\pi/\omega$ of modulation is plotted in fig. 3.4 for the case $(R,\omega) = (140, 3.52)$. The azimuthal velocity in a (z,r) plane is plotted at $\theta = 0$. The cylindrical annulus has been represented as straightened, so that the actual geometry can be visualized by closing the box cyclically. Two iso-surfaces where Ψ attains positive (yellow/grey coloured) and negative (blue/dark coloured) values are also plotted, hinting at the TV. The positive TV in the upper part of the gap (see figs 3.4(a) and 3.4(b)) is observed to switch its position with the negative vortex at half the cycle, and occupies the lower part of the gap (figs 3.4(e) and 3.4(f)) during the second part of the cycle.

In fig. 3.5 a full period of modulation has been similarly plotted for the case $(R,\omega) = (140, 7.04)$ which is characterized by NRTV. We notice that the positive and negative rotating TV do not change position during all the period and that they repeat their cycle of growth and decay every half a period.

3.3.1 Map of existence of NRTV and RTV

In fig. 3.6 the map of existence of NRTV and RTV has been depicted as a function of the two parameters R and ω. When ω is increased above a certain limit, the flow behaves like an oscillating Stokes' boundary layer [6] (ST, hereinafter): the frequency of oscillation is so high and the periodic variation of azimuthal velocity is confined in such a thin layer near the moving wall that the TV cannot be sustained in the bulk of the flow. We note that the range considered by [125] is limited to $2 < \omega < 8$, so that the Stokes' regime was not observed in their simulations.

The frequencies corresponding to the transition from the RTV to the NRTV and from the NRTV to the ST regime both show a dependence on R. This dependency is very strong for the NRTV-ST boundary, and relatively weak for the RTV-NRTV boundary.

In fig. 3.7 we have plotted the limit of existence of the various regimes as a function of ω and the square root of the difference between the current R and the R_0. This figure seems to suggest that the critical frequency and $\sqrt{R - R_0}$ scale in a linear way for both the NRTV-RTV and the RTV-ST boundaries.

In fig. 3.8 the thickness of the Stokes' layer $\delta_s = \sqrt{2\nu/\omega}$ is represented as a function of $\sqrt{R - R_0}$; it can be seen that the range of δ_s under consideration

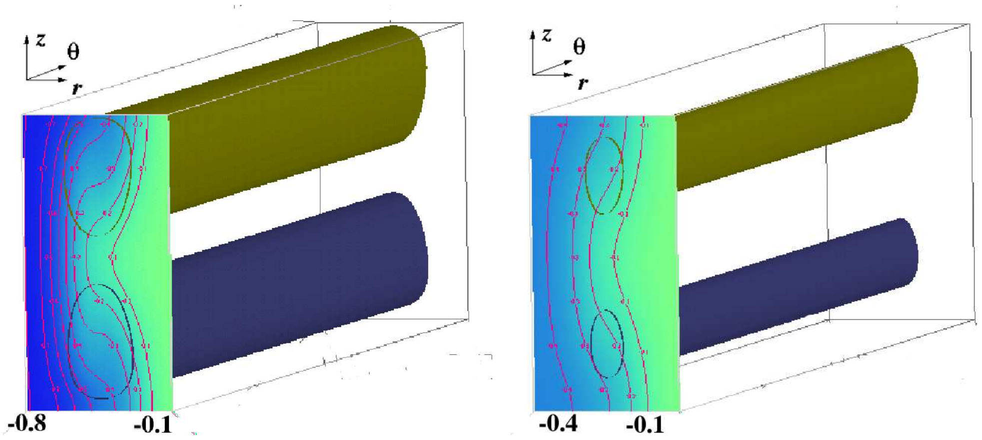

(a) $t = 0T$.

(b) $t = 4/50T$.

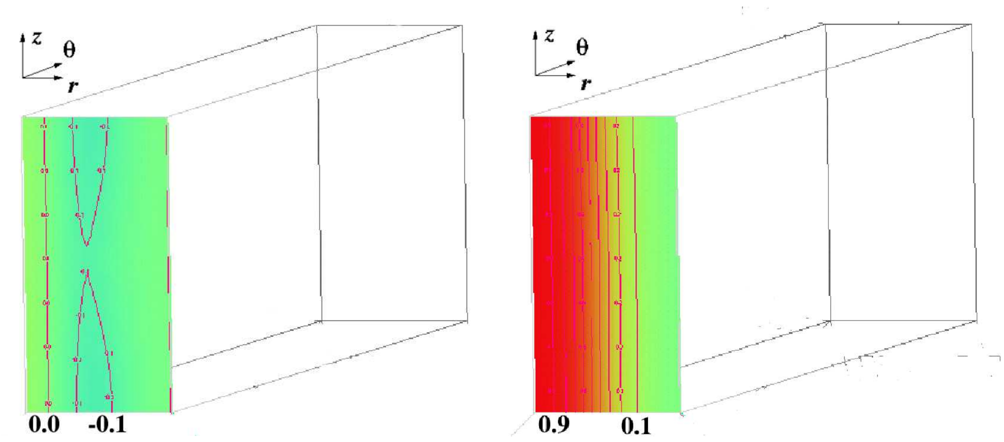

(c) $t = 8/50T$.

(d) $t = 20/50T$.

(For caption see facing page.)

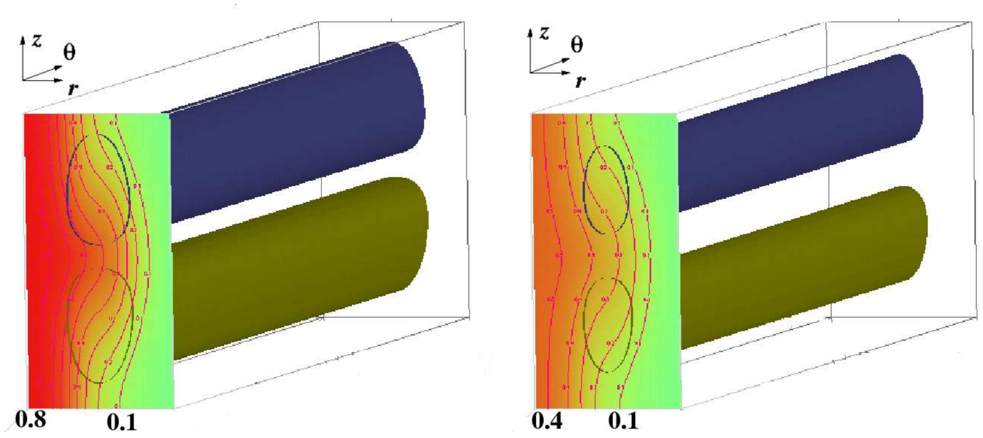

(e) $t = 24/50T$.

(f) $t = 28/50T$.

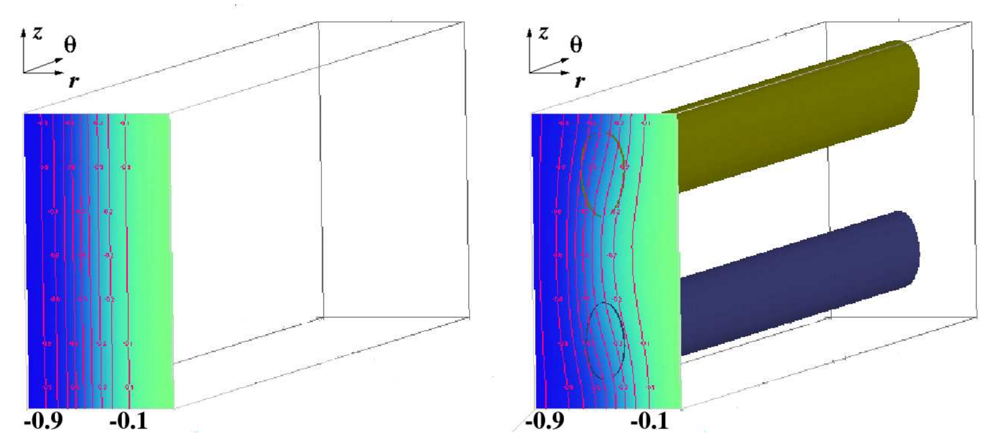

(g) $t = 44/50T$.

(h) $t = 48/50T$.

Figure 3.4: RTV for $(R, \omega) = (140, 3.52)$ at various instants of a temporal period T. Iso-azimuthal velocity contours ($\Delta w = 0.1 w_i$) and iso-Ψ surfaces: blue/dark=-0.08, yellow/grey=0.08.

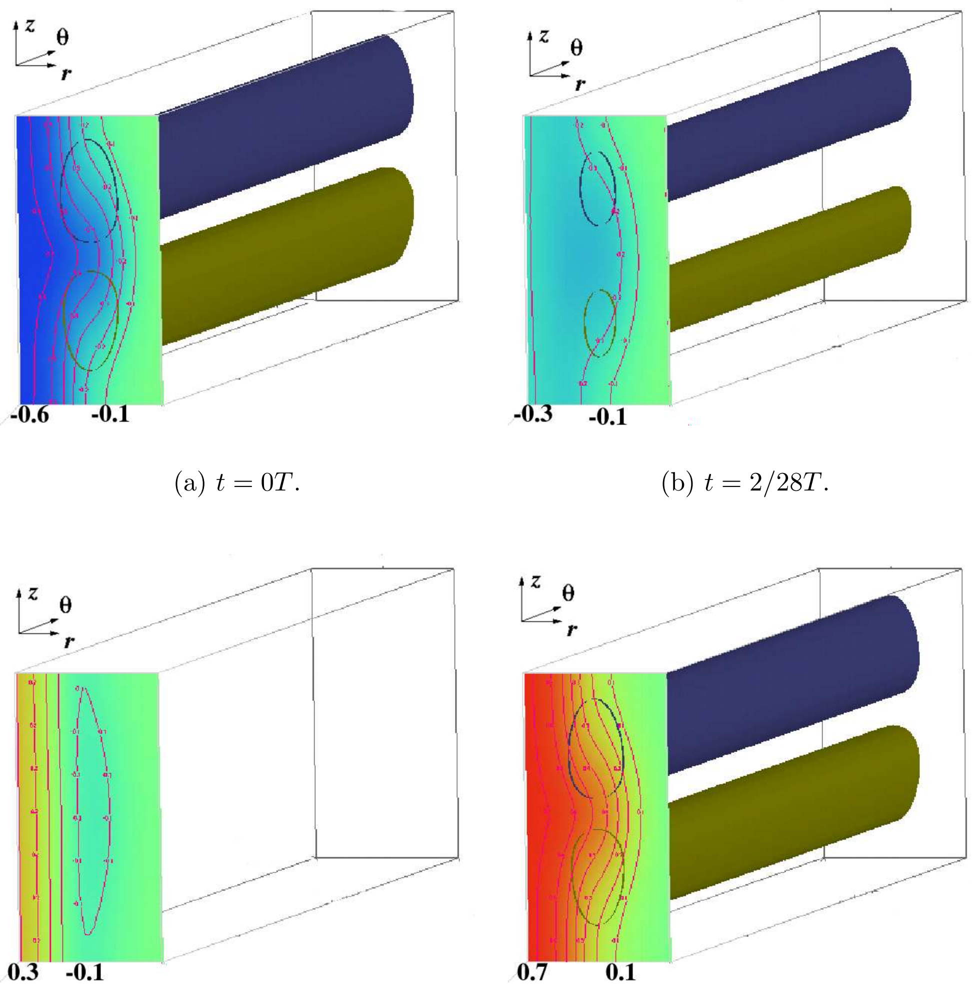

(a) $t = 0T$.

(b) $t = 2/28T$.

(c) $t = 4/28T$.

(d) $t = 12/28T$.

(For caption see facing page.)

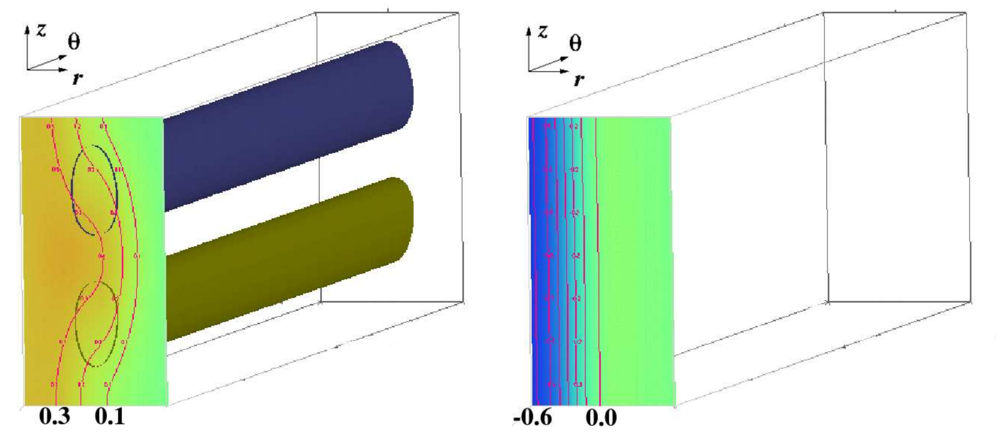

(e) $t = 14/28T$.

(f) $t = 18/28T$.

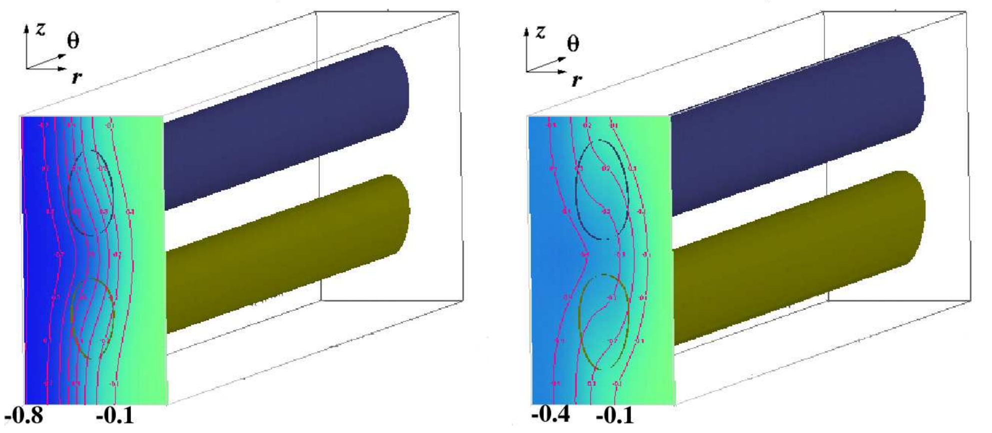

(g) $t = 24/28T$.

(h) $t = 26/28T$.

Figure 3.5: NRTV for $(R, \omega) = (140, 7.54)$ at various instants of a temporal period T. Iso-azimuthal velocity contours ($\Delta w = 0.1 w_i$) and iso-Ψ surfaces: blue/dark=-0.08, yellow/grey=0.08.

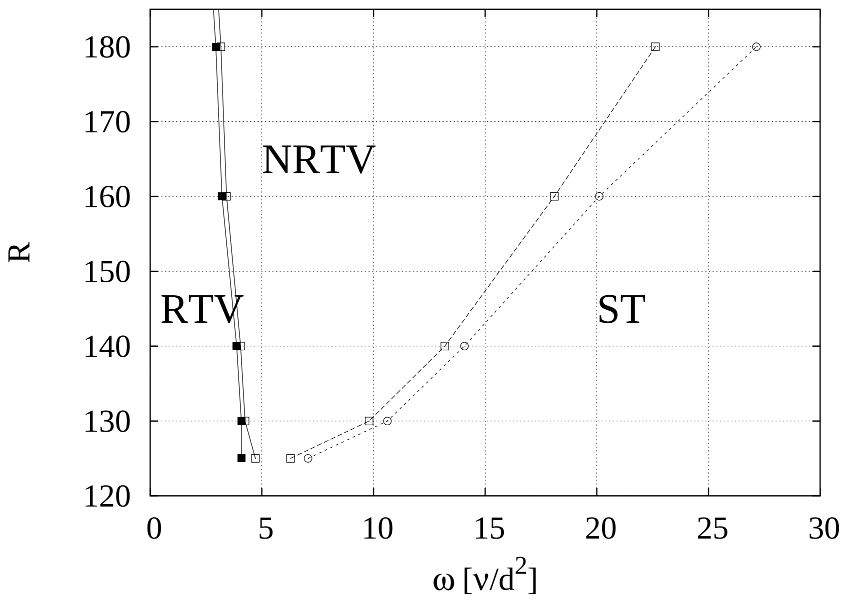

Figure 3.6: Map of the different regimes as a function of R and ω: RTV (■), NRTV (□), and ST (◯); RTV-NRTV boundary (continuous line), NRTV-ST boundary (dashed line).

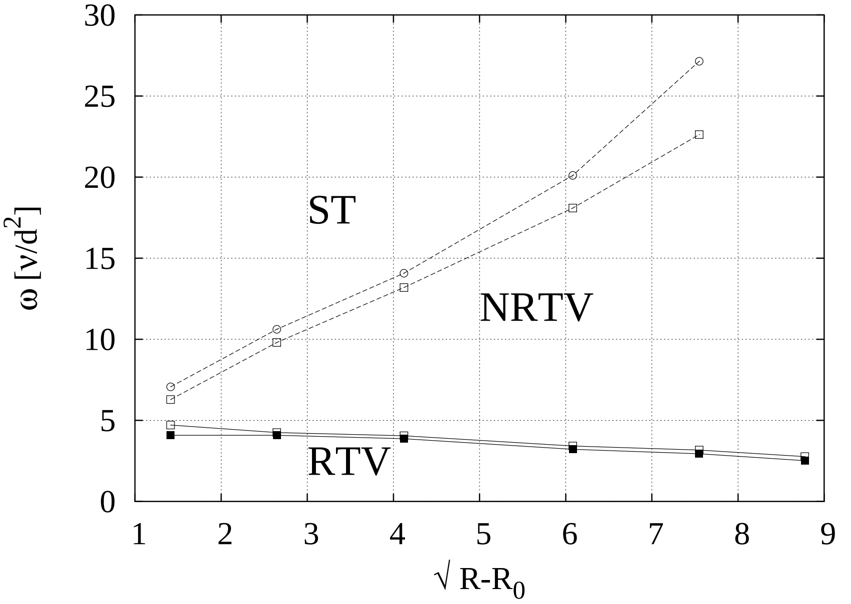

Figure 3.7: Limit of existence of RTV (■), NRTV (□) and ST (◯), and RTV-NRTV boundary (continuous line) NRTV-ST boundary (dashed line) represented as ω vs. $\sqrt{R-R_0}$.

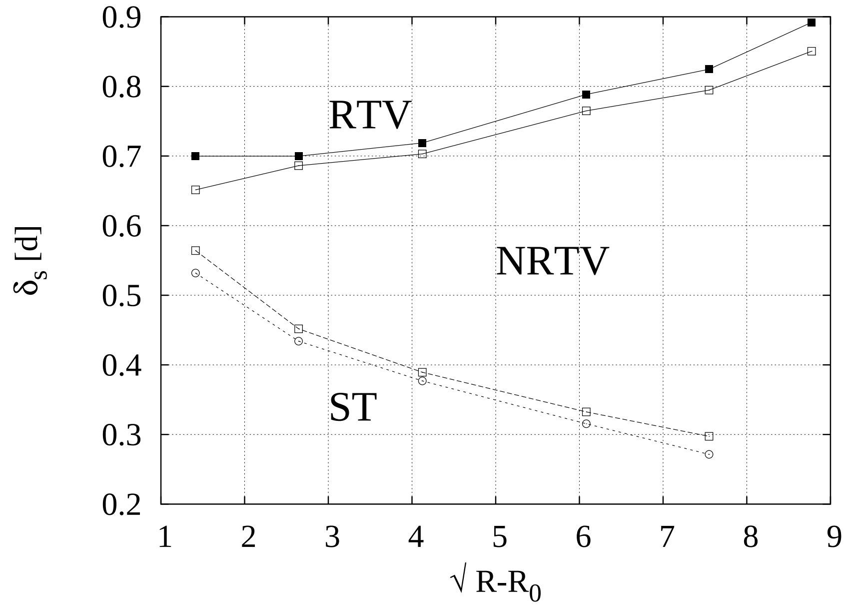

Figure 3.8: Limit of existence of RTV (■), NRTV (□) and ST (○), and RTV-NRTV boundary (continuous line) NRTV-ST boundary (dashed line) represented as δ_s vs. $\sqrt{R - R_0}$.

is confined below one gap width d.

3.4 Temporally modulated WTV

As R increases above R_0 the range of existence of NRTV grows, but when $R \approx 250$ we observe new phenomena appearing at a particular frequency. In fact, the number of vortices per axial length doubles, giving rise to four TV (N_4) instead of two (N_2), which is the solution for the $\omega = 0$ case at the same R_i.

We have compared the N_4 and N_2 flows in a $\omega = 0$ case; their main differences are: (1) for N_4 the critical Reynolds $R_{i,cr4}$ at which the TV first appear is around 100, while for N_2 it is $R_{i,cr2} \approx 68.2$; (2) the critical Reynolds $R_{i,w4}$ at which the Höpf bifurcation occurs is approximatively 250 which is lower than the value for N_2: $R_{i,w2} \approx 480$; (3) the range of R_i for which the Höpf regime thrives for N_4 is smaller than for N_2; (4) the temporal period of the wavy structures for the N_4 case is $T \approx 95\delta/w_i$ while for the single pair is $T \approx 165\delta/w_i$; (5) after the settlement of the short-living wavy regime, a sudden transition to chaotic regime appears for the N_4 case, while the pattern of transition experienced by the N_2 flow manifests other instabilities before entering the chaotic regime.

Although the critical $R_{i,w}$ at which waviness appears is about 480, we have recognized that by means of the temporal forcing a sub-critical bifurcation of the Höpf type can take place. In fact as R increases up to ≈ 300, in a particular range of frequencies, the TV of both the N_2 and N_4 classes begin to gain a certain amount of waviness, and become θ-dependent.

Though we have noticed that for certain value of the couple (R, ω) the waviness extends to multiples of the azimuthal wavelength ($m = 2, 3, ..$), the kinetic energetic content of the first azimuthal mode, $m = 1$, remains comparable or larger than those of the other modes. So we have chosen to use, as a suitable indicator of the waviness in the flow, the (radial) integral kinetic energy belonging to the zero axial and the first azimuthal mode:

$$E_{0,1} = \int_{\mathcal{R}_i}^{\mathcal{R}_o} \sum_{i=1}^{3} \langle |\hat{u}_i(\alpha = 0, m = 1, r)|^2 \rangle \, \mathrm{d}r, \tag{3.6}$$

where $\langle \cdot \rangle$ represents the time average. The energy $E_{0,1}$ is plotted for various values of R, from 350 to 500, as a function of ω in fig. 3.9. The curves are pinned with a number (2 or 4) indicating the N_2 or N_4 case.

At low R the energy $E_{0,1}$ clearly shows three features: two peaks and a broad band. The peak at low ω corresponds to a four vortices system, N_4, and appear at $\omega \approx 5\nu/d^2$; the flow has a three-dimensional character. The second peak belongs to the two vortices system, N_2, and appears at values of $\omega \approx 30\nu/d^2$, which corresponds to periods of modulation of $\approx 200\delta/w_i$. We recall that the characteristic period of a the N_2 system in the zero-modulation case is $T \approx 165\delta/w_i$. In fig. 3.10(a) an N_2 system of WTV has been depicted for $(R, \omega) = (425, 26.7)$.

The broad band is related to the high frequency-regime, $\omega > 40\nu/d^2$, and the flow consists of four WTV, N_4. We note that the appearance of the broad band is associated with a modulation period $T \approx 110\delta/w_i$, while the characteristic period of the N_4 vortices is $T \approx 95\delta/w_i$. In fig. 3.10(b) WTV, belonging to the N_4 class, have been plotted for $(R, \omega) = (400, 50.2)$.

We can thus claim that some oscillation frequencies, related to the characteristic period of the zero-frequency case, appear to amplify the wavy nature of the flow, resulting in a sub-critical transition to a wavy regime.

It can be seen that for the higher R the energy $E_{0,1}$ is almost constant with ω. Moreover, the flow is characterized by the N_2 vortices system for $\omega < 40\nu/d^2$ and by the N_4 vortices system for $\omega > 40\nu/d^2$. In particular, in fig. 3.11 we have plotted three different cases of WTV for the same $R = 500$. In fig. 3.11(a) a value of $\omega = 18.84\nu/d^2$ has been considered which results in a N_2 system of wavy vortices characterized by an azimuthal wavenumber

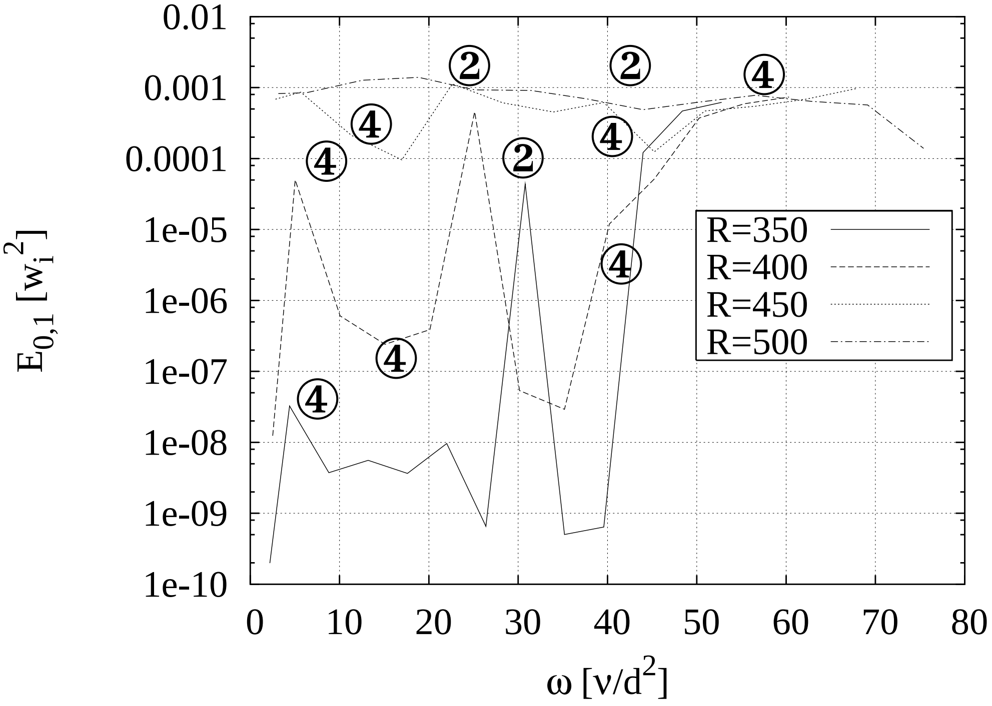

Figure 3.9: Energy of the first azimuthal mode represented by eq. (3.6) as a function of ω at various R. The symbols 2 and 4 represent the regions where the regime N_2 and N_4 respectively exist.

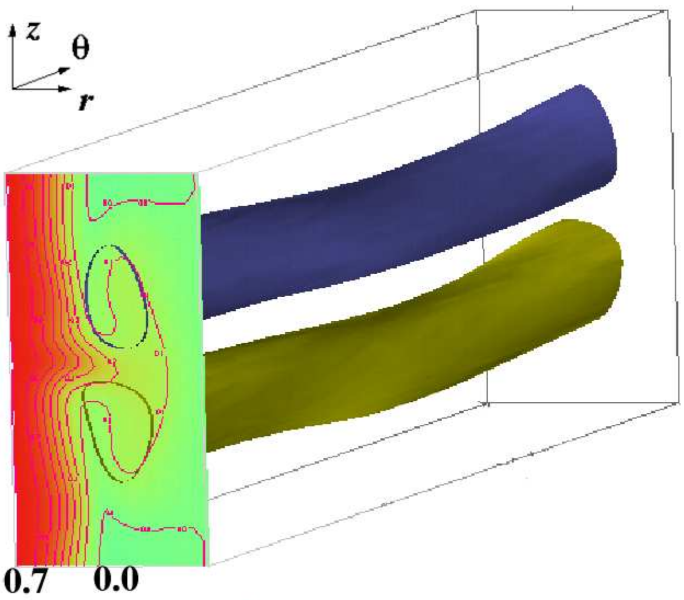

(a) N_2 at $(R, \omega) = (425, 26.7)$.

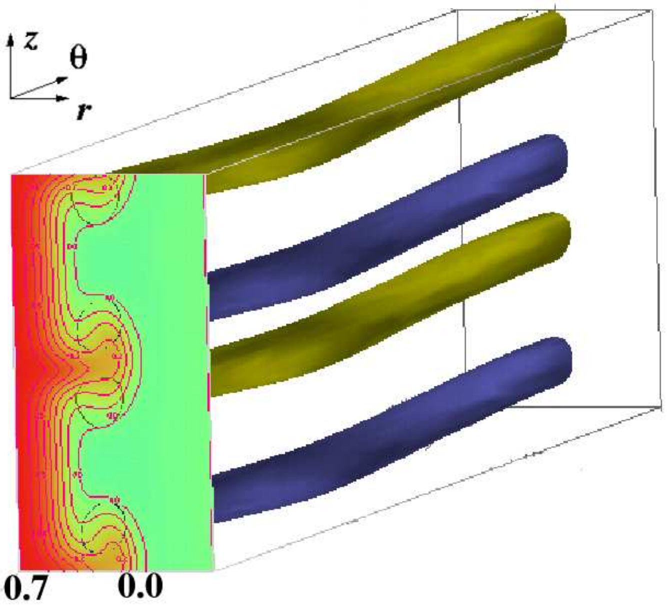

(b) N_4 at $(R, \omega) = (400, 50.2)$.

Figure 3.10: Sub-critical wavy regime: N_2 and N_4 WTV. Iso-azimuthal velocity contours ($\Delta w = 0.1 w_i$) and iso-Ψ surfaces: blue/dark=-0.08, yellow/grey=0.08

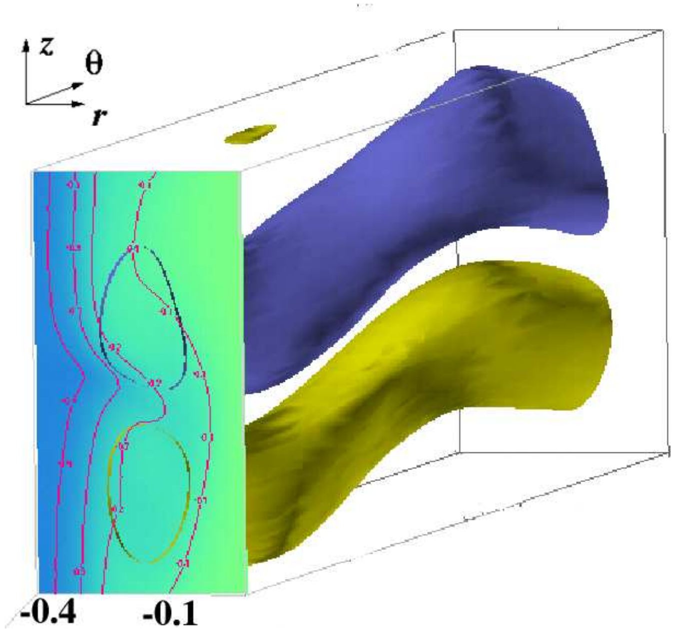

(a) $\omega = 18.84\nu/d^2$.

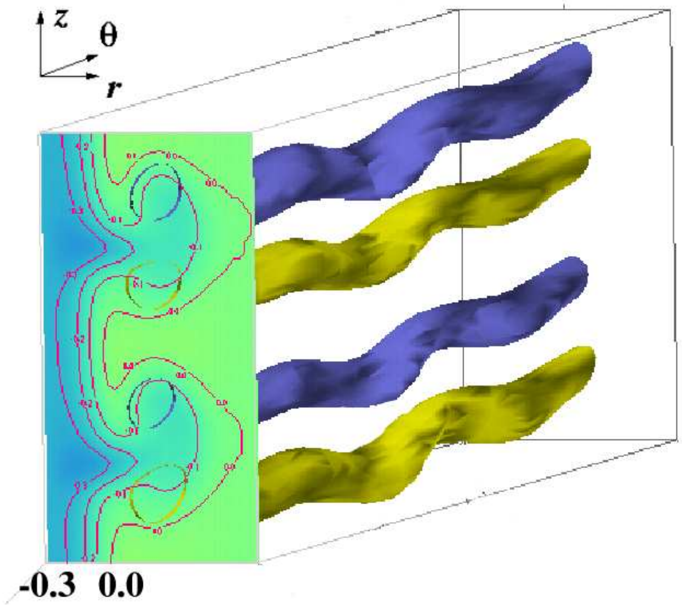

(b) $\omega = 69.11\nu/d^2$.

(For caption see facing page.)

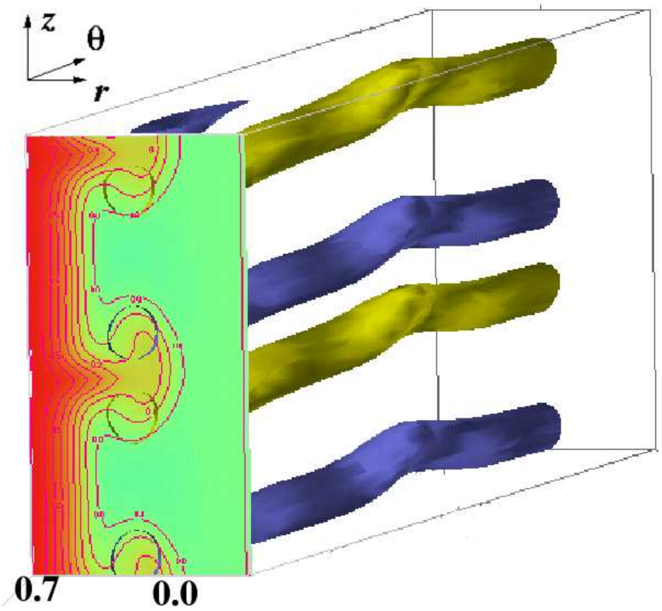

(c) $\omega = 56.52\nu/d^2$.

Figure 3.11: Wavy regime at $R = 500$. Iso-azimuthal velocity contours ($\Delta w = 0.1 w_i$) and iso-Ψ surfaces: blue/dark=-0.08, yellow/grey=0.08

$m = 1$; however other cases can happen, and, in fact for $\omega = 69.11\nu/d^2$, see fig. 3.11(b), an N_4 system appears with an azimuthal number $m = 3$. The competition of azimuthal modes have been observed too, as pictured in fig. 3.11(c), for the case $\omega = 56.52\nu/d^2$ where $m = 1$ and 2 appear at the same time.

3.5 Final remarks

Our numerical simulations of a temporally modulated TCF in a large-gap geometry with $\eta = 0.5$ confirm the existence of reversing and non-reversing TV, already observed by [125]. The value of critical Reynolds number at which these phenomena appear is in good agreement with the after-mentioned paper.

By extending the analysis in the $R-\omega$ space to a wider region compared to [125], new insight is provided into the behaviour of the temporally-modulated flow. We observe that the critical frequency at which the transition from RTV to NRTV appears depends on the Reynolds number. Moreover, by growing the modulation frequency another transition is noticed, for the first time: NRTV are substituted by oscillating Stokes' flows; the frequency at which this happens shows a strong dependence on the Reynolds number.

By growing the Reynolds number further, two classes of phenomena are observed: (1) an halving of the axial period of the vortices, as a result of the modulation at particular frequencies; (2) a sub-critical transition to the wavy regime. The latter feature is magnified at some frequencies, which are approximatively related to the typical period of the WTV in the zero-modulation limit, in what could be seen as an almost-resonant behaviour.

CHAPTER 4

SPATIAL MODULATION OF TAYLOR-COUETTE FLOW

In this chapter we present the results of a campaign of laboratory experiments conducted, under the supervision of Prof. Tom Mullin, at the Manchester Centre for Nonlinear Dynamics, University of Manchester. The flow visualisations of the patterns of instability experienced by a fluid confined between a moving inner cylinder with sinusoidal shape and an outer circular one at rest will be presented and discussed.

4.1 Background

As seen in the previous chapters, the TV are the fundamental patterns that characterize the TCF. As a consequence, various kinds of devices have been studied in order to modify the behaviour of these cellular-like structures, which influence the physical properties of the flow (i.e. mass transport and mixing), and to control their stability properties. These studies involved both temporal and spatial forcing, as mentioned in chapter §3 where the temporal forcing has been already addressed. Regarding the spatial forcing, we mention the experimental study of Wiener et al. [122] on an hourglass geometry, that of Ikeda & Maxworthy [54] on a sinusoidally-shaped inner cylinder at rest and a moving outer one, and the very recent ones by Rafique & Skali Lami [100], Staples & Smits [109] and Drozdov, Skali Lami & Rafique [38] on the moving sinusoidal inner cylinder and the outer one at rest. In particular, in the present chapter, we focus on the sinusoidal spatial modulation of the inner cylinder. This geometry has been also studied numerically by Drozdov [39] for its promising application in mixing, suspension and emulsification.

The experimental works previously carried out on this subject have focused on *qualitative* rather than *quantitative* description of instabilities that

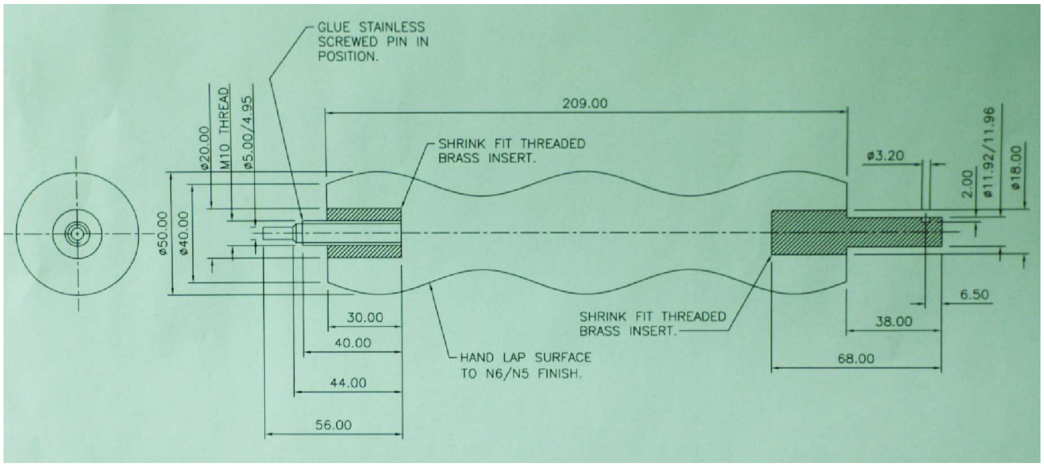

Figure 4.1: Technical design of the sinusoidally-shaped cylinder at Manchester Centre for Nonlinear Dynamics.

lead to the settlement of turbulence. At low values of the Reynolds number, a pair of cellular-like structures for each wavelength has been observed; the vortices successively double in number, and then experience some kind of oscillation which eventually leads to the turbulent regime, with again a single pair of TV-like structures. Our aim is to describe the pattern of transition through an analysis of high-quality images which permit quantitative information on the flow. Moreover, the region in which instabilities develop, the characteristic dimensions of the various regimes, as well as some features related to the non-uniqueness of the flow will described for the first time.

4.2 Experimental apparatus and procedures

The flow generated in the gap between a steady outer cylinder and a sinusoidally-shaped inner one has been studied through a campaign of experiments conducted at the Manchester Centre for Nonlinear Dynamics (MCND, University of Manchester), under the supervision of prof. Tom Mullin. The inner cylinder (see fig. 4.1) has been realized in aluminium, while the outer one is in Plexiglas, which guarantees good optical properties for the visualisations. The whole system is portrayed in fig. 4.2. The outer cylinder has a radius $\mathcal{R}_o = 31.63mm$, while the inner radius is

$$\mathcal{R}_i(z) = \overline{\mathcal{R}}_i + A\sin(2\pi z/\lambda),$$

where $\overline{\mathcal{R}}_i = 20mm$ is the average radius, $A = 5mm$ is the amplitude of the spatial modulation, $\lambda = 83.6mm$ is the wavelength of the sinusoidal cylinder.

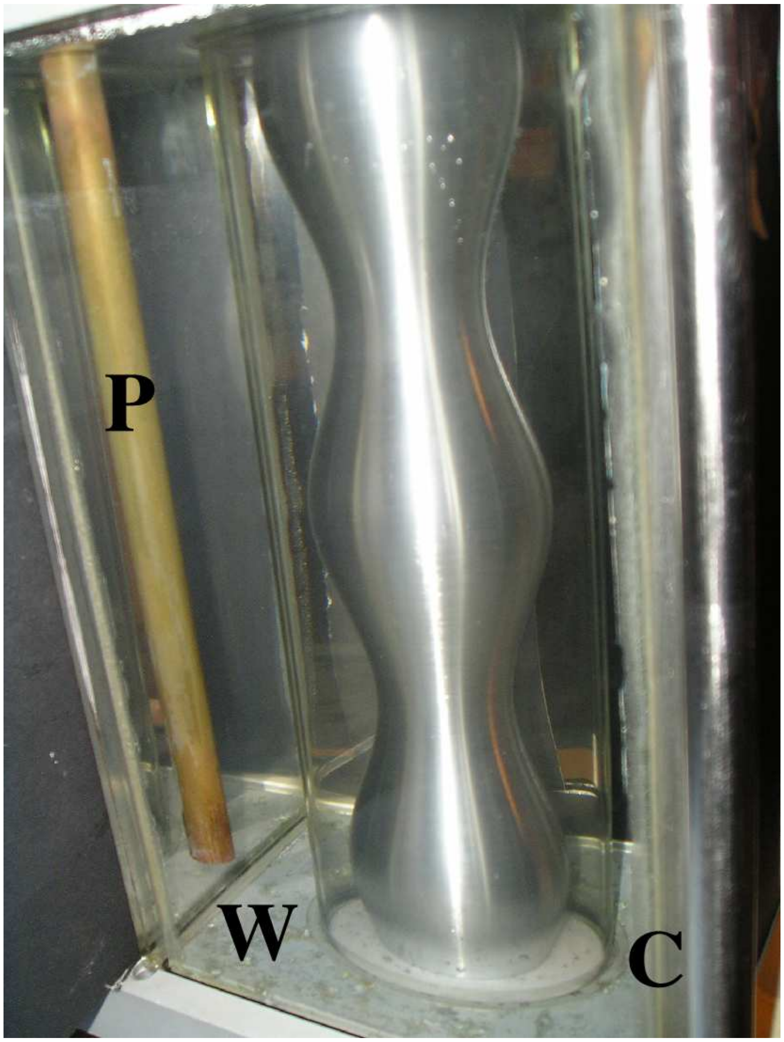

Figure 4.2: Experimental apparatus realized at the Manchester Centre for Nonlinear Dynamics. The water jacket is labeled as **W**, **P** is the pipe which permits the intake of fresh water into the outer cage **C**. The total vertical (axial) dimension of the apparatus is $310mm$.

Defining the mean gap as $d = \mathcal{R}_o - \overline{\mathcal{R}}_i$ we obtain $d = 11.63mm$ and, therefore, $A \approx 0.43d$, $\lambda = 7.19d$. The average radius ratio is $\overline{\eta} = \overline{\mathcal{R}}_i / \mathcal{R}_o \approx 0.632$. The tolerances are $\pm 0.2mm$.

The inner cylinder is driven round at an angular velocity Ω_i by a stepping motor controlled by an oscillator. The outer cylinder is held fixed, hence $\Omega_o = 0$. The total length of the sinusoidal cylinder is $H = 209mm \approx 18d$, at the top and bottom extremities the lids do not rotate. The temperature inside the gap is held constant at $25 \pm 0.1^\circ$ C through a water bath surrounding both cylinders (see fig. 4.2); the temperature of the bath is controlled by a commercial controller. The fluid is a water-glycerine mixture and its kinematic viscosity at 25° C has been measured with a Hubbelohde viscometer (suspended level viscometer) as $\nu = 5.94 \pm 0.03cSt$ (in accordance with the value of $5.79 \pm 0.03cSt$ measured in [105]); as a tracer, for the purpose of visualisation, a Mearlmaid Pearl Essence (a natural essence obtained from fish scales) was added in small quantities (few νl). A thin sheet of light generated from a slide projector enlighten a meridional plane between the cylinders; a digital camera (NikonD100) is used to capture the images with a resolution of 6.1 Megapixels (3.008×2.000) and color depth of 36 bit.

As pointed out by Coles [25], the feature of non-uniqueness is typical of TCF. In order to catch the primary branch of the solution (see Benjamin [8]), the angular velocity in our experiments is increased slowly, starting from rest up to the desired value of the Reynolds number

$$\overline{R}_i = \frac{\Omega_i \overline{\mathcal{R}}_i d}{\nu}.$$

The linear acceleration $\mathrm{d}\overline{R}_i/\mathrm{d}t$ was 0.17 which is far from the limit of sudden acceleration described in [123]. As a consequence, the total time to speed-up the system to $\Omega_i = 2.1 rad \quad s^{-1}$ is $240s$. When the existence of secondary branches is analysed, both sudden impulsive accelerations and decelerations of Ω_i are tried. Once the proper $\overline{R}_i$ is reached, the flow is allowed to stabilize for about ten times the average viscous diffusion time $\tau = d^2/\nu \approx 22.8s$.

A comparison (see tab. 4.1) with the other sinusoidal-cylinder experiments available in literature ([54],[100], [109], [38]) shows that our experiment is characterized by the largest relative amplitude (A/d) and relative wavelength (λ/d), and by the smallest radius ratio $\overline{\eta}$. These facts should permit to our experiment to follow the pattern of transition to turbulence in a clearer way than previous analyses.

Ref.	A/d	λ/d	$\overline{\eta}$	$A/\overline{\mathcal{R}}_i$
[54]	0.112	2.8	0.96	0.0048
[100]	0.391, 0.196	7.1	0.68	0.186, 0.093
[109]	0.12	2,3,4,5	0.90	0.0133
[38]	0.031, 0.061, 0.122	5.6	0.80	0.038, 0.076, 0.153
here	0.43	7.2	0.63	0.25

Table 4.1: Comparison between the characteristic dimensions of the sinusoidally-shaped inner-cylinder setups available in literature.

4.3 Results

4.3.1 Primary flow

At the very low value of $\overline{R}_i$ (around 20.5), we have observed that in each wavelength a cellular pattern develops in the form of a pair of counter-rotating vortices (see fig. 4.3); the same kind of flow was observed by other investigators. The elements of the pair rotate in a direction such that the fluid is pumped from the outer cylinder to the inner one in correspondence of the minimum radius. Apart from their different shape, these structures are quite similar to the TV of the straight-cylinder case, and the wavelength of the couple is around 0.8λ. We call this, for obvious reasons, the *mono-cellular regime.*

In the case of straight cylinders (see [63]) we know that:

- the typical wavelength of the vortex pair is $\approx 2d$, which is considerably lower than the value of $5.8d$ observed for the sinusoidally-shaped cylinder;
- for the radius ratio corresponding to the maximum gap in the sinusoidally-shaped cylinder $\eta_m = \mathcal{R}_m/\mathcal{R}_o = (\mathcal{R}_i - A)/\mathcal{R}_o \approx 0.475$ the critical Reynolds number $R_{i,cr}$ at which TV develop is around 65 and becomes even higher for $\overline{\eta}$.

This suggests that the effect of the spatial modulation is to force an early transition from the laminar to the primary flow, and that this forcing influences the wavelength of the Taylor-like vortices.

4.3.2 Secondary flow

By slowly increasing $\overline{R}_i$ we can follow the primary branch of the solution; at $\overline{R}_i \approx 85$ a secondary instability develops. Another pair of counter-rotating

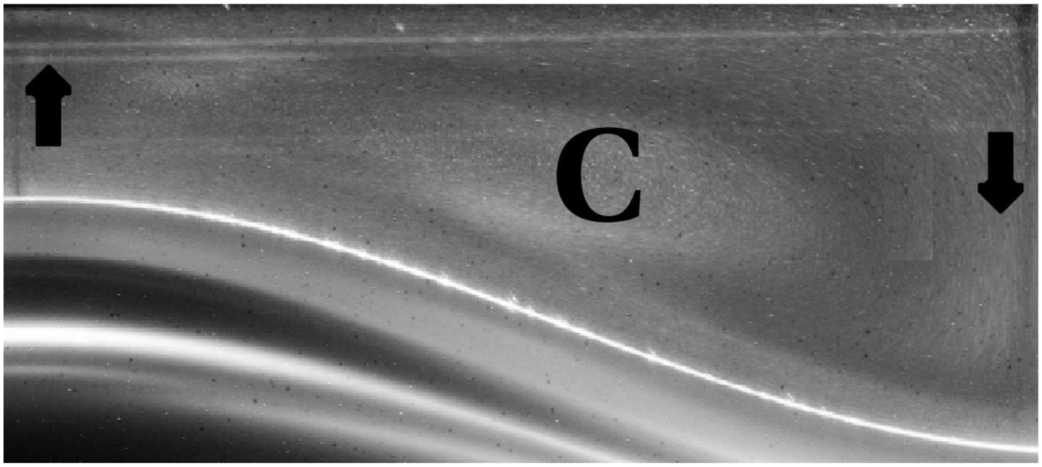

Figure 4.3: Picture of a (z, r) meridional plane for half a wavelength of the sinusoidal shaped inner cylinder. In the central region a clockwise-rotating vortex **C** can be noticed. The white line is the sinusoidal inner cylinder, the upper part of the picture is outer cylinder.

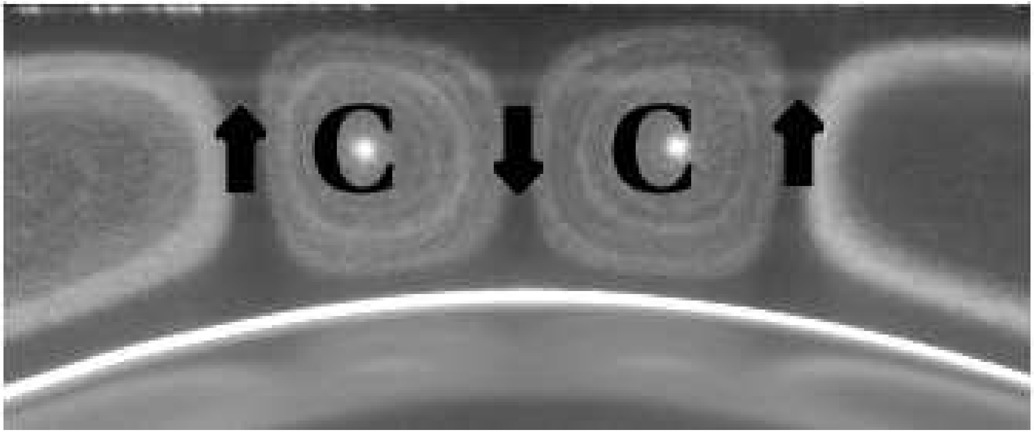

Figure 4.4: Picture of a (z, r) meridional plane for a 0.28λ length in the trough region of the sinusoidal shaped inner cylinder. In the central region a couple of counter-rotating small vortices, labeled as **C**, can be noticed; on both sides of the small vortex pair a large scale vortex is present.

vortices appears in the region corresponding to the minimum gap, as in fig. 4.4.

As depicted in fig. 4.5 these secondary vortices are generated near the outer cylinder (see fig. 4.5(c)); in figs 4.5(c) to 4.5(h) we can follow their growth after their birth near the outer cylinder: they increase in size expanding towards the inner one, and eventually they occupy the whole gap. They succeed in filling the whole space between the primary vortices. We appoint this second type of flow as the *bi-cellular regime*.

Even though we believe this instability should be studied considering the complex geometry as a whole, an intuitive explanation for the development of these secondary vortices can be gained from the following argument. At first, we recognize that the region corresponding to the crest of the sinusoidal cylinder is not heavily interested by the primary cellular-like structures. If we consider, in this simplified vision, the sinusoidal geometry as a locally-deformed circular cylinder, we can associate at each z point a local Reynolds number

$$R_i(z) = \frac{\Omega_i \mathcal{R}_i(z) d(z)}{\nu},$$

as depicted in fig. 4.6; this function has a local minimum in correspondence of $z = \lambda/4$, where $\mathcal{R}_i(\lambda/4) = \mathcal{R}_M$, the crest. So once fixed the $\overline{R}_{i,cr}(z)$ the crest is interested by the instability later than trough.

We have also plotted R_i/Ω_i in case of a sinusoidal amplitude of $A/2$. It is easy to see that by halving the amplitude the local minimum of R_i is significantly less pronounced, while the local maximum is slightly decreased; so it is possible, as described by [100], that for the same $\overline{R}_i$ the case with amplitude A is in mono-cellular regime, while the one with $A/2$ experiences a bi-cellular flow. This means that the amplitude has a massive effect on the road of transition to turbulence.

We have then focused on the area occupied by the secondary vortices. For each vortex, the area has been evaluated as the white region surrounded by dark margins as in fig. 4.4; by analysing three series of pictures of the same region, the mean area occupied by the vortex has been computed, the error bars have been derived from the standard deviation of the area. The area has been plotted in fig. 4.7 versus $\overline{R}_i$, normalized with the dimension d^2. In the mono-cellular regime, the area is obviously equal to zero. As the instability develops the secondary vortex appears, and its size grows, eventually reaching an asymptotic value which is slightly below unity; we note that the unitary case corresponds to a vortex which has the same shape of those in the straight-cylinder geometry.

Though the secondary vortices have already been observed by [100] (see the picture (3.ii) of the cited work), this is the first time that the birth of

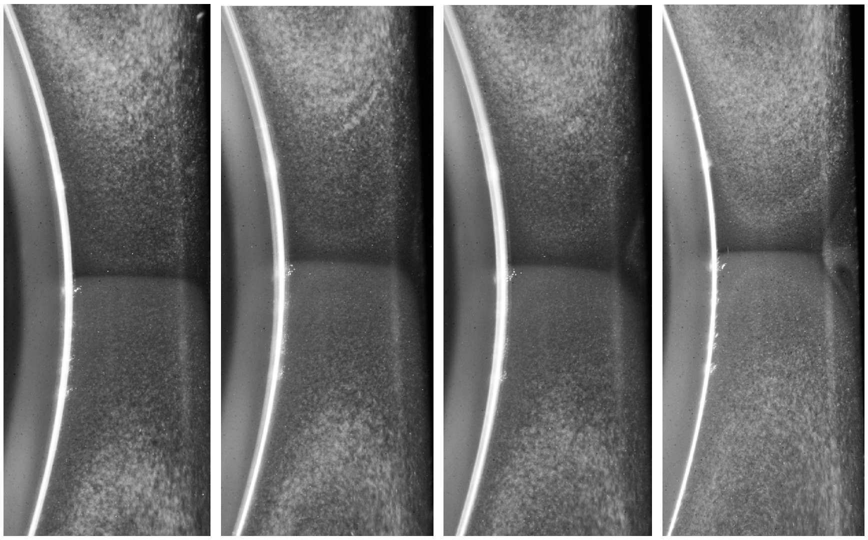

(a) $\overline{R}_i$=82, (b) $\overline{R}_i$=85, (c) $\overline{R}_i$=86, (d) $\overline{R}_i$=87,

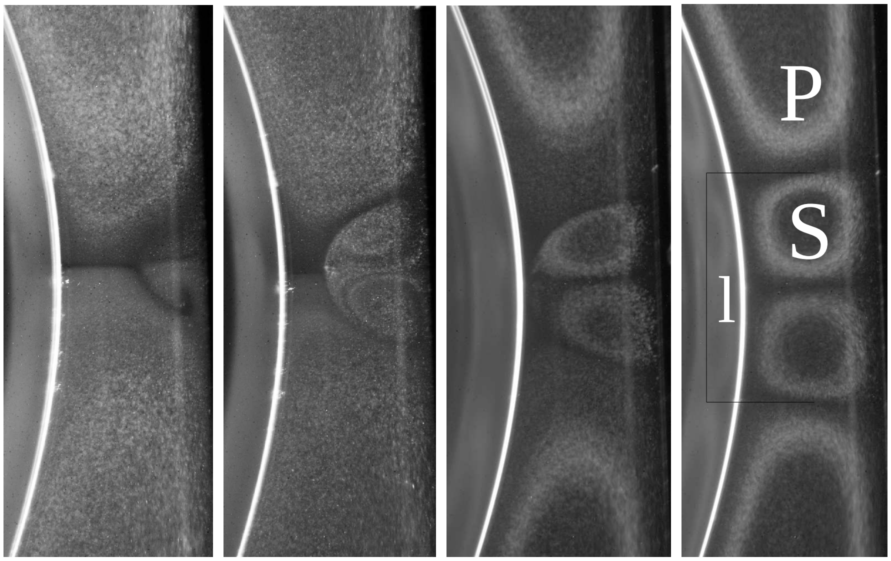

(e) $\overline{R}_i$=88, (f) $\overline{R}_i$=90, (g) $\overline{R}_i$=92, (h) $\overline{R}_i$=112,

Figure 4.5: Pictures of a (z, r) meridional plane in correspondence of the trough region: transition from the mono-cellular to the bi-cellular regime in dependence of $\overline{R}_i$. The bright curved line on the left of each picture is the inner cylinder surface, while the outer cylinder is at the right. P is the primary vortex, S is the secondary one, and l is the distance between the edges of two secondary vortices.

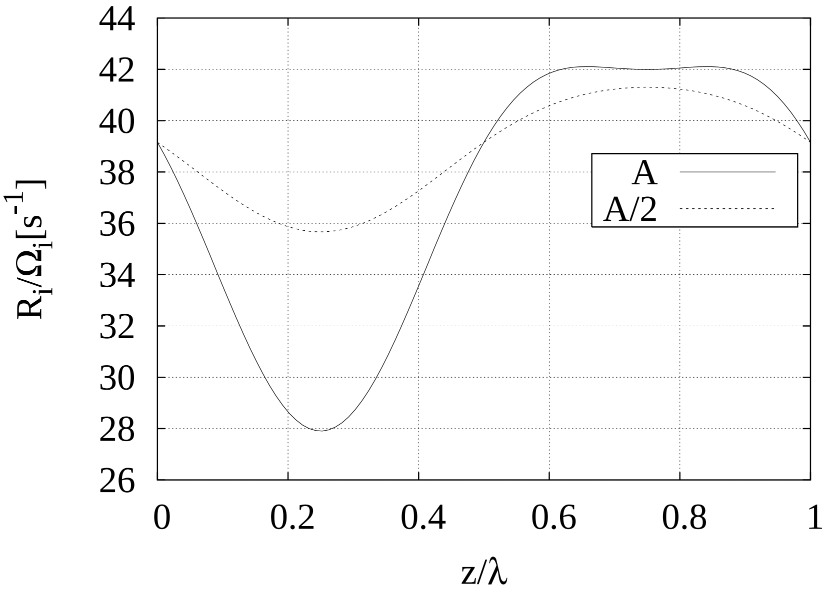

Figure 4.6: $R_i(z)/\Omega_i$ as a function of z/λ for an amplitude of the sinusoidal modulation $A = 5mm$ (continuous line) and $A/2$ (dashed line).

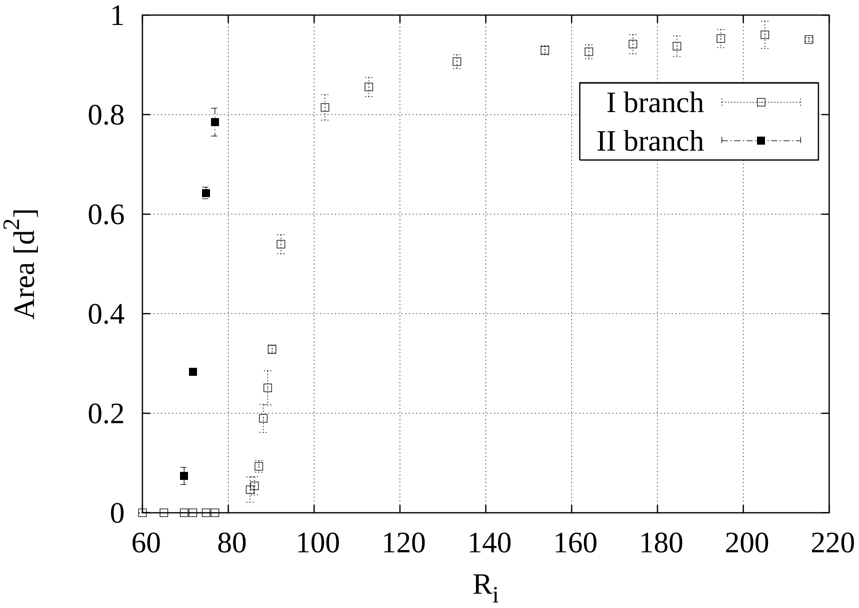

Figure 4.7: Bifurcation diagram: area occupied by a secondary vortex as function of $\overline{R}_i$. The primary branch is depicted with □, and the secondary branch with ■.

the flow is observed and a description in terms of characteristic parameters of the flow is proposed.

4.3.3 Non-uniqueness: part I

It has been recognised, during our experiments, that a critical Reynolds number $\overline{R}_{i,nu}$ (around 65) exists, above which the flow appears to be non-unique. In fact, for $\overline{R}_i > \overline{R}_{i,nu}$ it is possible, by a sudden start of the angular velocity or by an abrupt deceleration from very high $\overline{R}_i$, to obtain a bi-cellular regime instead of the expected mono-cellular one. In fig. 4.7 we have described in terms of vortex area also one of these secondary branches, which in line of principle can be very numerous. Though non-uniqueness is a common feature in TCF with straight-cylinder geometry, its discovery in the spatially-modulated flow is new. As a remark we recall that, in analogy with the circular-cylinder case, the critical value of the Reynolds number $\overline{R}_{i,nu}$ is expected to depend on the experimental apparatus.

4.3.4 Höpf bifurcation

The bi-cellular flow exists and thrives up to $\overline{R}_i \approx 220$. Above this value the secondary vortices begin to oscillate in the axial direction; each vortex oscillates in phase with its companion: the flow experiences an Höpf bifurcation. Also [100] recognized that "with the increase of the rotation rate, the flow undergoes the subsequent transition and the multi-vortex configuration starts oscillating", however they do not give any further description of this flow.

The oscillations can be described in terms of their amplitude and frequencies. Since we are able to analyse just a (z, r) meridional plane at a time we can't say whether these oscillations are of the same kind of those experienced by the flow in WTV, i.e. we cannot guarantee whether the flow is still axisymmetric.
However, as $\overline{R}_i$, grows three facts can be observed:

- the centre of each vortex shifts towards the crest;
- the amplitude of the oscillation increases;
- the radius of each vortex diminishes.

The analysis of the pictures suggests an indicator that takes into account the above-mentioned facts: the distance between the external edges of the vortices belonging to the secondary pair (distance l in fig. 4.5(h)). This distance diminishes as $\overline{R}_i$ increases, as shown clearly in fig. 4.8.

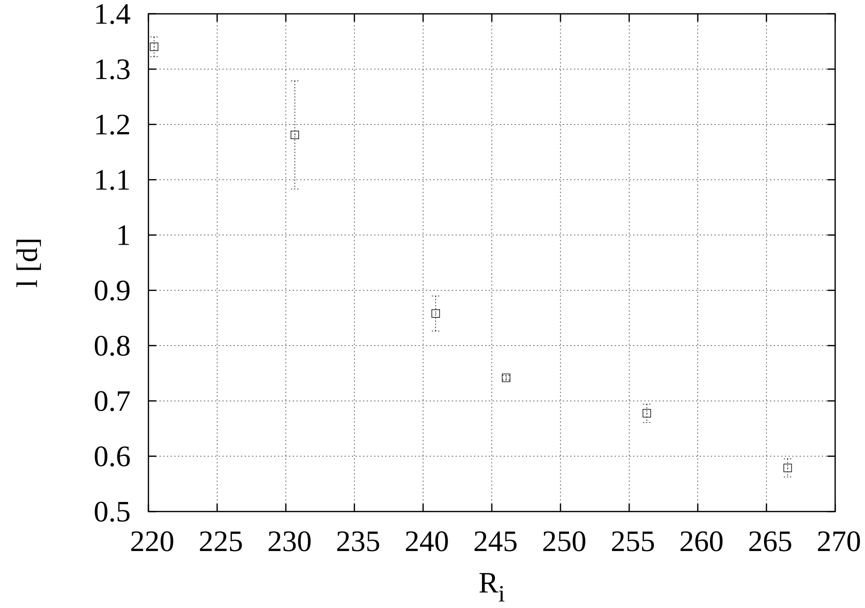

Figure 4.8: Distance between the edges of the wavy vortices l as a function of $\overline{R}_i$.

We have also measured the period T of the oscillation: for each $\overline{R}_i$, seven measurements of the period have been taken with a digital chronograph, and then the mean value and the error bars evaluated. As the Reynolds number increases, T appears to diminish. However, dividing the period T by the period of rotation of the inner cylinder $T_{rot} = 2\pi/\Omega_i$, it turns out that, in the interval considered (see fig. 4.9), the ratio between the characteristic times T/T_{rot} is almost constant with $\overline{R}_i$ at a value of 0.42.

4.3.5 Pattern of transition to turbulence

Above a certain $\overline{R}_i$ (around 287) the secondary vortices disappear altogether, and the primary vortices grow to fill the whole wavelength. We appoint this flow as the *second mono-cellular regime.* Though this regime is quite similar to the mono-cellular regime of §4.3.1, the characteristic length λ of the vortices is now larger than that of the primary mono-cellular flow.

The flow remains successively stable for a wide range of $\overline{R}_i$. In fact, it is only at $\overline{R}_i \approx 450$ that the flow begins to oscillate in radial direction in correspondence of the trough. The amplitude of this phenomenon is large and gives rise rapidly to the onset of a turbulent motion. The appearance of turbulence, at $\overline{R}_i \approx 480$, does not eliminate the cellular pattern in the flow, at least in the range of $\overline{R}_i$ considered (< 820). This is consistent with what

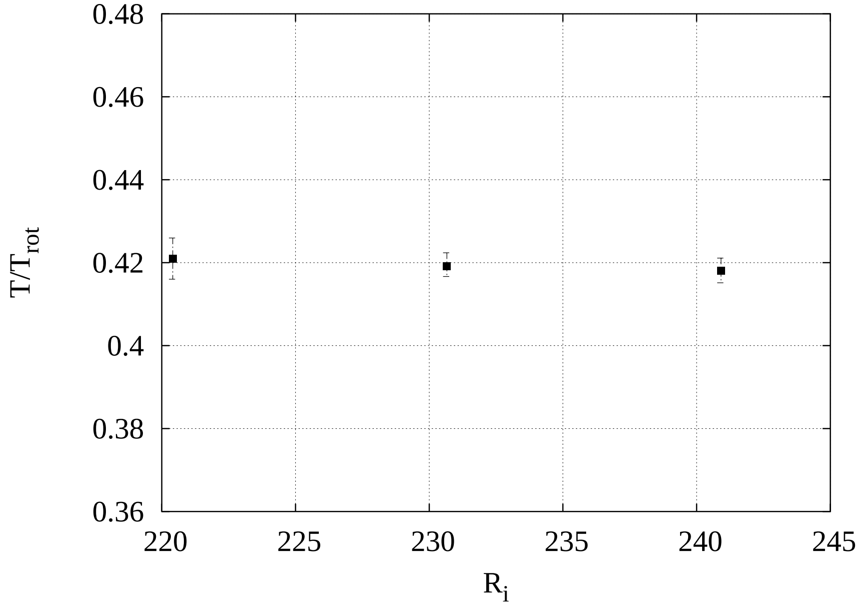

Figure 4.9: Ratio between the period of the oscillation T and the period of rotation of the inner cylinder T_{rot} expressed as a function of $\overline{R}_i$.

is known from the circular-cylinder case, where the TTV last up to very high R_i.

4.3.6 Non-uniqueness: part II

We have previously shown in §4.3.3 that the phenomenon of non-uniqueness is deeply rooted in the nature of the problem; moreover, the higher $\overline{R}_i$ the wider is the variety of multiple possible solutions.

As an example in fig. 4.10 four different cases at $\overline{R}_i = 246$ are shown. The regions near the top and the bottom of the lids of the apparatus are pictured. The solution corresponding to the first branch has an even number of cells, is symmetric with respect to a plane at $z = H/2$ and perpendicular to the z axis, and it is characterized by a wavy regime. However, we have observed also a sub-critical solution with a steady secondary mono-cellular flow, and both symmetric and non-symmetric features with an even number of cells.

In figs 4.10(a) and 4.10(e) two small vortices (we call **A** the one close to the lids and **B** the other) appear in the 25% of wavelength near the extremities; another symmetric case is the one depicted in figs 4.10(b) and 4.10(f) where the upper and lower region are occupied by a single vortex of type **A**. A snapshot of a non-symmetric flow has also been captured: while the upper

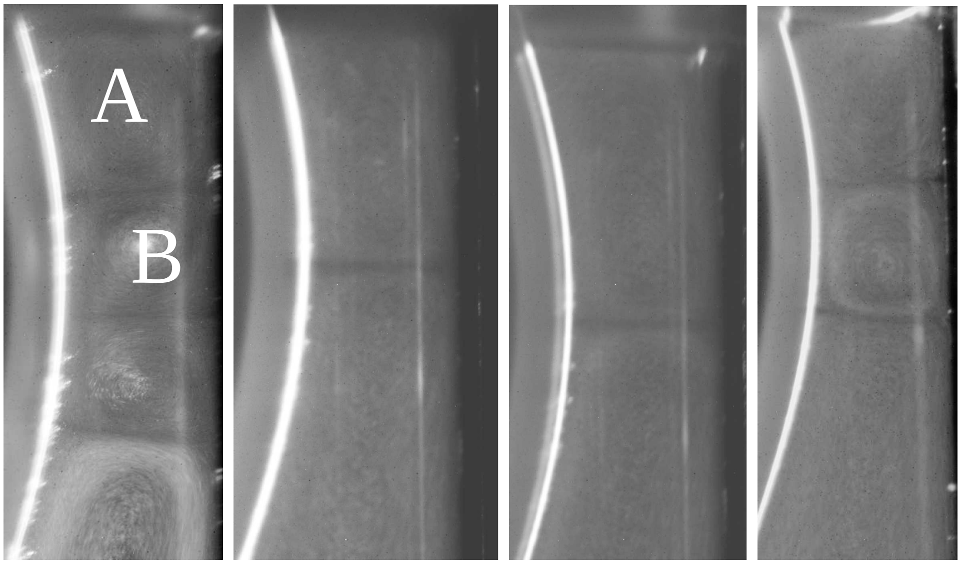

(a) Bicellular. (b) Mono-cellular. (c) Non symmetric. (d) Anomalous.

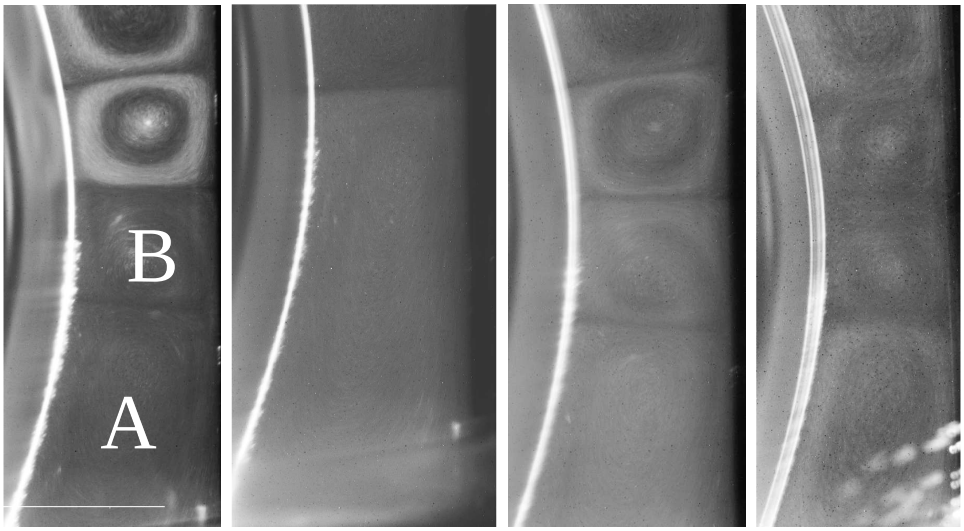

(e) Bicellular. (f) Mono-cellular. (g) Non symmetric. (h) Anomalous.

Figure 4.10: Non-unique flow configurations at $\overline{R}_i = 246$, pictured in a z, r meridional plane at the top (a-d) and the bottom (e-h) extremities of the apparatus. The white curved line on the left of each picture is the inner cylinder surface, the outer cylinder is the right part of each picture. Lid is on top in (a-d) and on bottom in (e-h). **A** is the vortex close to the lid and **B** is the vortex close to vortex **A**.

quarter (see fig. 4.10(c)) is occupied by a **A**-vortex, the lower quarter (see fig. 4.10(g)) shows a bi-cellular structure quite similar to that of fig. 4.10(e).

In all the previous examples the sense of rotation is dictated by the Ekman pumping layer (see [6], [108], [29]): the fluid goes from the stationary lids to the moving wall, resulting in a counter-clockwise rotating vortex near the upper extremity and a clockwise rotating vortex near the lower one.

However, it has been shown [10] for the TCF with straight-cylinder that this is not the only possibility: flows with an odd number of cells may exist, the so-called anomalous modes. We have verified that the same is true for the spatially-modulated apparatus. In fact both the **A**-vortices of figs 4.10(d) and 4.10(h) have clockwise sense of rotation, thus indicating anomalous modes.

4.4 Final remarks

In this chapter, we have presented a quantitative evaluation of the pattern of transition from the laminar solution to the onset of the turbulence in a Taylor-Couette apparatus with sinusoidally-shaped inner cylinder. In order to obtain a better comprehension of the spatial forcing, both wavelength and amplitude of the spatial modulation are larger than in the previous analysed apparatuses.

The measurements suggest that the very first effect of the spatial forcing is to trigger a centrifugal instability at values of $\overline{R}_i$ which are small in comparison with the straight-cylinder case. However, the structures generated by this instability are quite similar to the TV seen in the straight-cylinder case, except for the wavelength which is significantly larger (around $0.8\lambda = 5.8d$ compared to $2d$ for the straight case). By further increasing $\overline{R}_i$ above around 85, another instability is generated near the outer cylinder: toroidal-like structures appear in steady pair. Successively, these structures experience an Höpf bifurcation characterized by an almost constant ratio of period of oscillation T to period of rotation $T_{rot} = 2\pi/\Omega_i$, namely $T/T_{rot} \approx 0.42$. Eventually the oscillations lead to a chaotic regime, where the TV-like structures are still present, even though superimposed on a turbulent background. Moreover, as commonly happens in nonlinear systems, non-unique behaviours have been noticed above a certain value of $\overline{R}_i$ (around 65). The comparison between our results and the existing literature suggests that the pattern of transition, once fixed $\overline{\mathcal{R}}_i$ and $\mathcal{R}_o$, depends dramatically on the wavelength λ and the amplitude A.

CHAPTER 5

TURBULENT TAYLOR VORTICES

This chapter deals with the turbulent TCF, studied with DNS. A co-existence of large-scale structures and small-scale turbulence is the main feature of this flow: the large-scale vortical structures, TTV, fill the whole gap, and affect the mean and instantaneous properties of the flow. Our aim is to identify the relative contribution of TTV to low-order turbulence statistics.

5.1 Background

Since the first experiments of Pai [94] the existence of TTV has stirred the interest of a plethora of scientists. In fact, the persistence of large-scale, well-defined, vortical structures in such a wide range of Reynolds number, up to several hundred times the critical value $R_{i,cr}$, raised at first the suspicion that some kind of large-scale, organized, vortical structure permeates the fluid flows in turbulent regime. Today many studies (see [88]) recognize that the existence of the same kind of structures in laminar and turbulent regimes in TCF depends on its particular symmetries, and that the fascinating suggestion of the persistence of cellular structures up to the turbulent regime cannot be generalized to the turbulent flow *tout court*.

Moreover, for the particular nature of its pattern of transition to turbulence, the TCF was seen, in the early years of its study, as a paradigm of the process of transition to turbulence via the Landau's successive bifurcations hypothesis [64]. In fact the toroidal TV gain successive waviness and modulation in azimuthal direction as the Reynolds number increases, and, as mentioned above, they are still present in turbulent regime; however, the analysis of the energy spectra has shown (Fenstermacher, Swinney & Gollub [43]) that, after initial stages which are characterized by sharp peaks, hence in accordance with Landau's theory, a broad-band component and, successively, a large amount of noise appear as predominant. Accordingly, the transition-to-turbulence scenario based on an infinite-bifurcations pattern suggested by the Russian scientist seems to be not fully applicable in this case (see [15]).

Many aspects of the TTV have been already investigated. Koschmieder [62] studied their characteristic wavelength, showing its strong dependence on the flow history. Smith & Townsend [106] discovered that large-scale vortices exist up to values of R_i several hundreds times larger than the critical Reynolds number at which they first appear; however, both the value $R_{i,ttv}$ of the Reynolds number at which TTV develop, and their dependence on R_o are not yet well defined (see the dashed region in fig. 1.3 from [2]). Barcilon et al. [5] and later Barcilon & Brindley [4] studied the small-scale structures which develop close to the walls at high Reynolds numbers and co-exist with TTV.

While the literature on experimental works is impressive, with many experiments conducted in the most various ranges of Reynolds number, the only numerical simulation devoted to the subject is, to our knowledge, the conference paper by Hirschberg [51]. In fact, the other numerous and useful numerical simulations of TCF deal with the capture of the first instabilities (as in Fasel & Booz [42], Marcus [79], Moser, Moin & Leonard [87]), in regimes which are far from a fully developed turbulent case (as in Raspo et al. [101], Magere & Deville [74]) or are focused on various ways of preventing the TV from reaching the turbulent regime by controlling the boundary conditions (Marques & Lopez [82]) or by adding secondary flows (Wereley & Lueptov [120]).

Comprehensive and extensive analyses of the turbulence statistics for the turbulent TCF are absent in literature, owing to the lack of numerical simulations and the intrinsic difficulty in obtaining valuable experimental measurements close to moving walls. As a consequence, it is unclear the relative dynamical role of TTV and the typical turbulent structures, as well as the most immediate strategy to discriminate between them. Hence the relative contribution of the large-scale structures to the main statistical quantities, which are customarily employed to characterize the turbulent flow, still needs to be addressed.

Other aspects of this flow which are fundamental both for the design of TC devices and for the RANS and LES modelling of turbulent flows over streamwise-curved walls need further examination. For example, the existence of a logarithmic law for the mean velocity profile on the concave and convex wall is still an open problem, since, as discussed in [96], some researchers believe in its presence, while others denies it.

To give a contribution in this area, we have performed several DNS of the TCF in the fully turbulent regime, focusing on a small-gap geometry.

The simulations resulted in large databases, whose statistical analysis will be described in the following.

5.2 The numerical simulations

We have studied the turbulent flow which develops in the gap between a pair of cylinders with infinite axial length as sketched in fig. 1.1. Direct numerical simulations of the Navier–Stokes equations have been carried out with the numerical method, the computer code and the computing system described in chapter §2.

We have used the half-gap width δ and the velocity of the inner cylinder w_i as scaling quantities, so that the reference time is δ/w_i. We have chosen a small-gap geometry of the same kind of that considered by Andereck, Liu & Swinney [2] with $\eta = 0.882$, which corresponds to an inner radius $\mathcal{R}_i = 15\delta$ and an outer radius $\mathcal{R}_o = 17\delta$. Regarding the dimensions of the periodic box, a few considerations on the nature of the flow have been necessary to suggest the proper values. The azimuthal extension of the box has been chosen as $l_\theta = \pi/2$, which is twice that used in [51]. Experimental results [62] suggest that the axial wavelength of a pair of vortices is 5δ in turbulent regime, so we have chosen an axial dimension of $L_z = 5\delta$, which has been a posteriori accounted as reasonable for the TTV simulation.

To obtain a good resolution of the spatial scales, 512×256 Fourier modes have been used respectively in the axial and azimuthal directions, while 129 points have been considered for the discretization of the radial direction. The grid size for the simulation with the highest Reynolds number, i.e. $(R_i, R_o) = (10500, 0)$, are $3.3 - 3.7$ wall units[1] for the outer and inner wall respectively, in the axial directions, from 0.7 (near the inner wall) to 3.0 (in the centreline) wall units in the radial direction, and less than 8.7 in the streamwise direction. The time advancement is $\Delta t = 0.015\delta/w_i$ which corresponds to $\Delta t^+ \approx 0.1$. The computational domain has the following dimensions in wall units: L_z is around 880, and $\mathcal{R}_c l_\theta$ is approximately 4410. One simulation with an axial dimension of twice this size has not shown significant differences in terms of the considered turbulence statistics (see below).

In a preliminary stage, a number of simulations has been also carried out for smaller R_i on a coarser grid, i.e. 128×128 modes and 129 radial points on a computational box of $L_z = 5\delta, l_\theta = \pi/4$; they are listed in tab. 5.1 and correspond to cases (a) to (e). For $R_i = 6000$ also a small amount of rotation of the outer cylinder in both the directions has been considered.

---

[1] Obtained by non-dimensionalazing with ν and the friction velocity u_τ, as defined by eq. (5.2).

The simulations have been run for $700\delta/w_i$; the first time interval of $200\delta/w_i$ has not been considered in the averaging process, which has been carried out with 26 flow fields, each separated from the other by $20\delta/w_i$. The computational time for the simulation (f) is around two weeks on a cluster of 10 SMP Personal Computers, each equipped with 2 Intel Xeon 2.66 GHz CPU, and 512MB of 266 MHz SDRAM.

In all these simulations the initial field consists of the laminar solution of eq. (1.1), with superimposed disturbances of $\mathcal{O}(10^{-3})$ in correspondence of all Fourier modes. Other initial conditions have been tested, and no significant differences have been noticed.

5.3 The onset of turbulence

We start by defining the Reynolds number R_τ based on the average friction velocity u_τ as:

$$R_\tau = \frac{u_\tau \delta}{\nu}. \tag{5.1}$$

From the balance of forces in the azimuthal direction, see [124], the average friction velocity is defined as:

$$u_\tau = \sqrt{\frac{(1-\gamma)^2\overline{\tau}_i + (1+\gamma)^2\overline{\tau}_o}{2\rho}}, \tag{5.2}$$

where $\gamma = \delta/\mathcal{R}_c$ is the curvature parameter evaluated at the central line, the over-bar represents the average in the (z, θ) directions, the azimuthal shear on a plane normal to r in the θ direction is

$$\tau(z, \theta, r, t) = \mu\left(\frac{\partial w}{\partial r} - \frac{w}{r}\right),$$

the indices i and o in eq. (5.2) represent the value of an r-dependent function evaluated, respectively, at $r = \mathcal{R}_i$ and $r = \mathcal{R}_o$. It is also possible to define a local R_τ as $R_{\tau,p} = u_{\tau,p}\delta/\nu$, where

$$u_{\tau,p} = \sqrt{\frac{\overline{\tau}_p}{\rho}}$$

is the local friction velocity at the inner $(p = i)$ or outer $(p = o)$ wall.

As shown by eq. (5.2) the local Reynolds number is connected with the wall shear τ. The behaviour of the wall shear in a turbulent plane channel is deeply influenced by the presence of near-wall structures (elongated streaks,

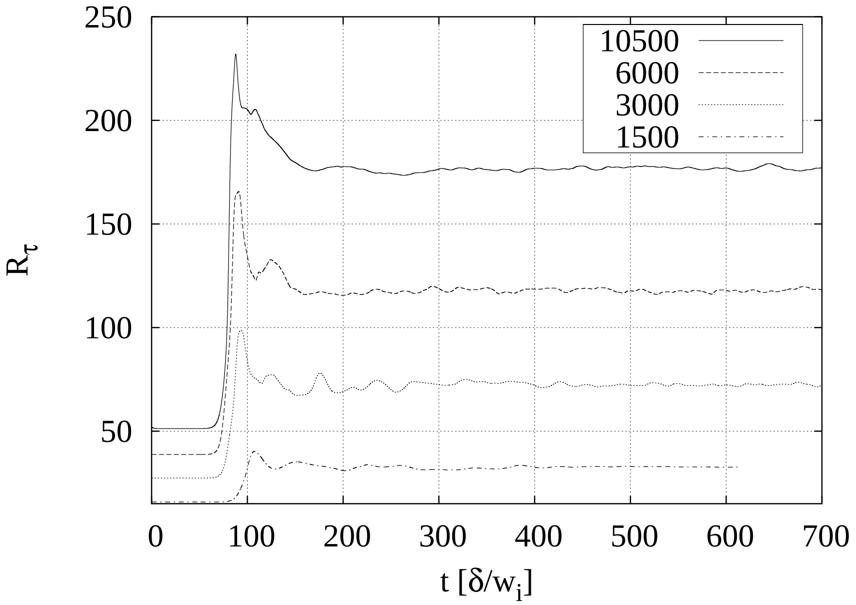

Figure 5.1: $R_\tau(t)$ for $R_o = 0$ at various R_i: 10500 (continuous line), 6000 (dashed line), 3000 (dotted line), 1500 (dashed-dotted).

quasi-streamwise vortices) which cooperate to the self-sustained cycle [56] of turbulence. In TCF large-scale vortical structures exist, which fill the central part of the gap and redistribute the shear on the walls. It is not obvious therefore how to separate this effect from those produced by turbulence, since the friction velocity takes into account and mixes up both contributions.

In fig. 5.1 the temporal behaviour of R_τ is plotted for various values of R_i and $R_o = 0$. The signal shows a transient of around two hundreds time units, which are necessary for the turbulent regime to settle from the (initial) perturbed laminar solution. In the fist part of the signal at $t \approx 100\delta/w_i$, an overshoot around $30 - 40\%$ higher than the long-time mean value appears. After the overshoot, R_τ decreases and it takes another hundred time units to reach a statistically steady plateau for $t > 200\delta/w_i$.

In tab. 5.1 for various pairs (R_i, R_o) the time-averaged values of $R_{\tau,i}$, $R_{\tau,o}$ and R_τ, computed after discarding the transient, are reported.

Since no previous DNS is available for a turbulent TCF at such high values of the Reynolds number, a comparison can be given just with the plane turbulent Couette flow. The DNS carried out by [61] has R_i which corresponds to our case (b); and R_τ is found to be approximatively 52. This suggests that the large-scale structures induced by curvature increase the shear significantly on both walls; as a first and rough approximation, we can

case	(R_i, R_o)	$R_{\tau,i}$	$R_{\tau,o}$	R_τ
a	1500,0	34.9	31.3	33.0
b	3000,0	77.0	68.5	72.5
c	6000,0	125.6	111.5	118.1
d	6000,300	122.4	108.7	115.1
e	6000,-300	129.0	114.4	121.2
f	10500,0	188.1	164.6	176.1

Table 5.1: R_τ for various values of (R_i, R_o).

estimate the contribution of TTV as the relative difference between R_τ for the present case and the plane Couette flow, this value is around 40%.

It is easy to see, from the above-mentioned table, that the effect of increasing R_i at a fixed R_o, is to make all $R_{\tau,i}$, $R_{\tau,o}$ and R_τ grow. The behaviour of the local Reynolds number $R_{\tau,i}$ and $R_{\tau,o}$ is depicted in fig. 5.2 as a function of the R_i for the case of steady outer cylinder. At high value of R_i both $R_{\tau,i}$ and $R_{\tau,o}$ seem to follow an almost linear behaviour. Moreover the data of the numerical simulation by [61] and [7] for the plane Couette flow have been added, so that the effect of the curvature can be better appreciated. A counter-rotating ($R_o < 0$) outer cylinder produces a further, small increase in the three strain-related Reynolds numbers, the opposite is true for a co-rotating ($R_o > 0$) outer cylinder. This result is consistent with what is expected in the Couette case, where the Reynolds number depends on the difference between the velocity on the two walls, so that counter-rotating walls produce an effective higher Reynolds number.

Though, as already stated, no previous DNS exist at such high R_i, a comparison is however possible with the experimental data available in literature. In fact, the value of the torque $G(\mathcal{R}_i)$ non dimensionalized by $\pi \rho w_i^2 \mathcal{R}_i^2 H$ can be derived from the Wendt's empirical formula (by [119] and also cited in [34]):

$$G(\mathcal{R}_i) = 0.46 \left[\frac{1-\eta}{\eta^2} \right]^{0.25} R_i^{-0.5}, \tag{5.3}$$

and compared with the results of our experiments, as done in tab. 5.2. The relative error $(G^W - G^{DNS})/G^W$ is within few percent for all the cases considered.

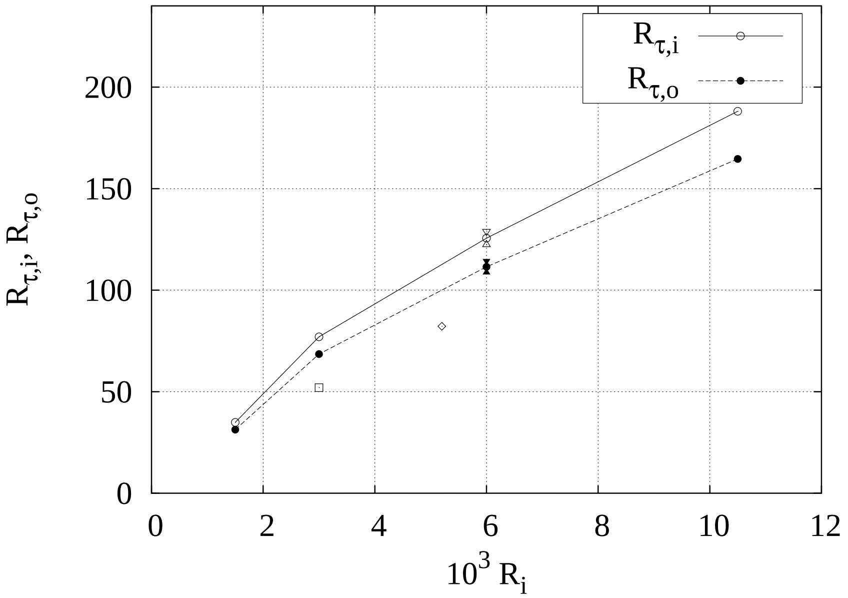

Figure 5.2: $R_{\tau,i}$ (continuous line) and $R_{\tau,o}$ (dashed line) as a function of R_i, for $R_o = 0$ (◯), $R_o = 300$ (△), and $R_o = -300$ (▽). The □ refers to the simulation by [61] and the ◇ to [7], both performed in a plane Couette flow.

case	(R_i, R_o)	here	Wendt	rel. err.
b	3000,0	372	370	-0.006
c	6000,0	495	523	0.053
f	10500,0	635	687	0.076

Table 5.2: Torque $G(\mathcal{R}_i)$ at various R_i. The comparison is made with the experimental data from Wendt's formula 5.3.

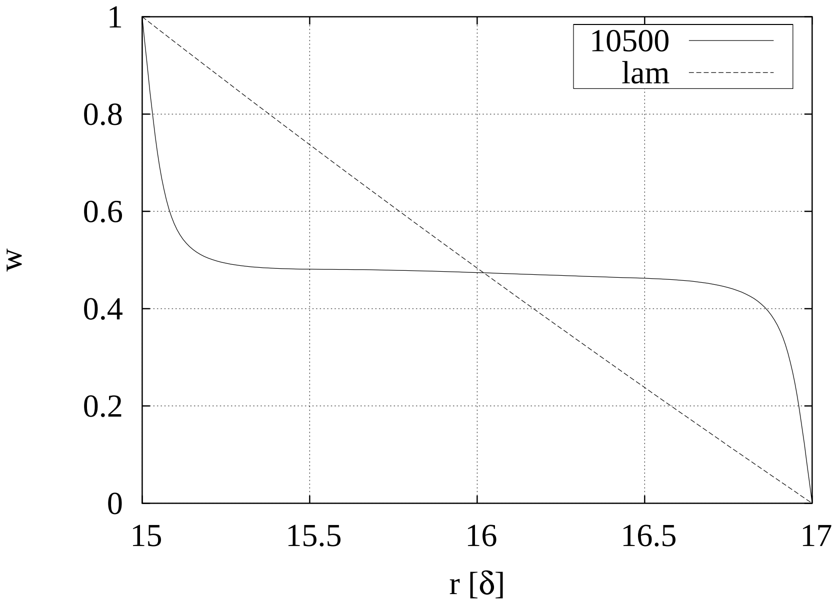

Figure 5.3: Comparison between the mean azimuthal velocity $\overline{w}(r)$ at $(R_i, R_o) = (10500, 0)$ (continuous line) and the laminar solution (dashed line) eq. (1.1) as a function of r.

5.4 Low-order turbulence statistics

5.4.1 *Mean profile*

In fig. 5.3 the radial profile of the azimuthal component $\overline{w}$ of the velocity vector, averaged in time and in (z, θ) directions, is shown for the highest Reynolds number tested, i.e. $(R_i, R_o) = (10500, 0)$. A comparison is made with the laminar solution represented by the equation (1.1). A region of slowly decreasing velocity appears in the central region of the gap,

The angular momentum $r\overline{w}$ has been depicted in fig. 5.4; the central region has almost constant $r\overline{w}$, which means a nearly constant circulation (see [116], [106], [102]). The shear layers at the walls become thinner as R_i increases. These results are in agreement with the experimental observations of [94], though our simulations are carried out at lower Reynolds number.

As pointed out by Bradshaw [16], an analogy exists between the effect of buoyancy and that of rotation. As a consequence, a parameter which is commonly used to characterize the effect of buoyancy has been re-casted in order to represent the effect of rotation (see [116]): the Richardson flux

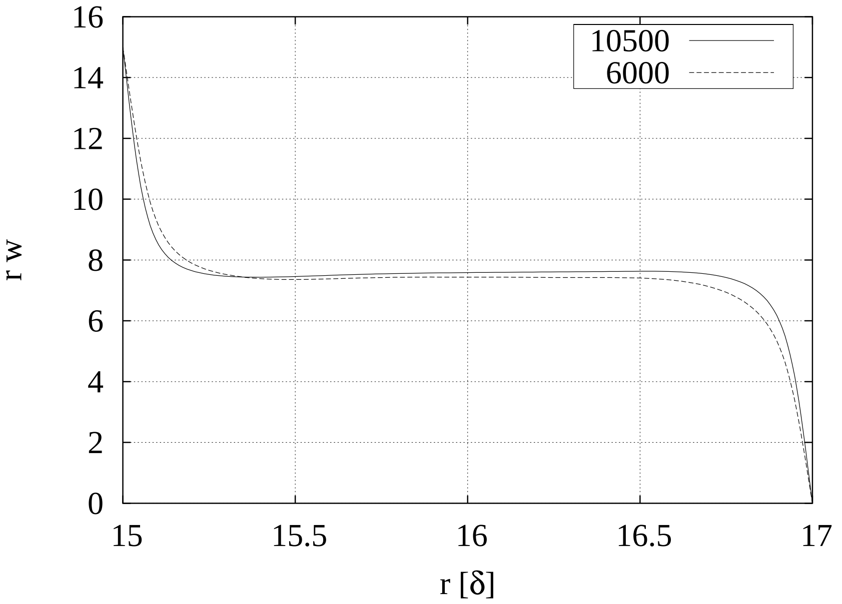

Figure 5.4: Angular momentum $r\overline{w}(r)$ for $R_i = 10500$ (continuous line) and $R_i = 6000$ (dashed line), with outer cylinder at rest.

number

$$R_f = \frac{-2\overline{v'w'}\,\overline{w}r^{-1}}{-\overline{v'w'}[\partial\overline{w}/\partial r - \overline{w}r^{-1}]}, \tag{5.4}$$

where the prime the turbulent fluctuation; it represents the ratio between the streamwise and radial production term in the turbulent kinetic energy equation. In fig. 5.5 the behaviour of R_f is plotted as a function of the radial position $\Delta r = r - r_i$ for $R_i = 6000$ and 10500; both curves show an asymmetry and a minimum value in the inner part of the channel which gets closer to the inner radius as R_i increases. As a consequence, the relative importance of the streamwise production increases with R_i and the region of high production is shifted towards the inner cylinder, as R_i grows.

In fig. 5.6 the azimuthal velocity has been plotted in logarithmic scale and in local wall units. Both walls have been drawn in the same graph. We notice that a viscous sublayer exists on both walls, where $\overline{w}^+$ equals r^+; the velocity profile is fairly similar on both walls up to $\Delta r^+ \approx 40$, but in the central part of the channel the velocity in the outer part is slightly higher than in the inner part.

The presence of a logarithmic law for the mean azimuthal velocity is investigated in fig. 5.7. We note that no DNS exist for the TTV, so the data are compared with the plane Couette and channel flow. The velocity profile

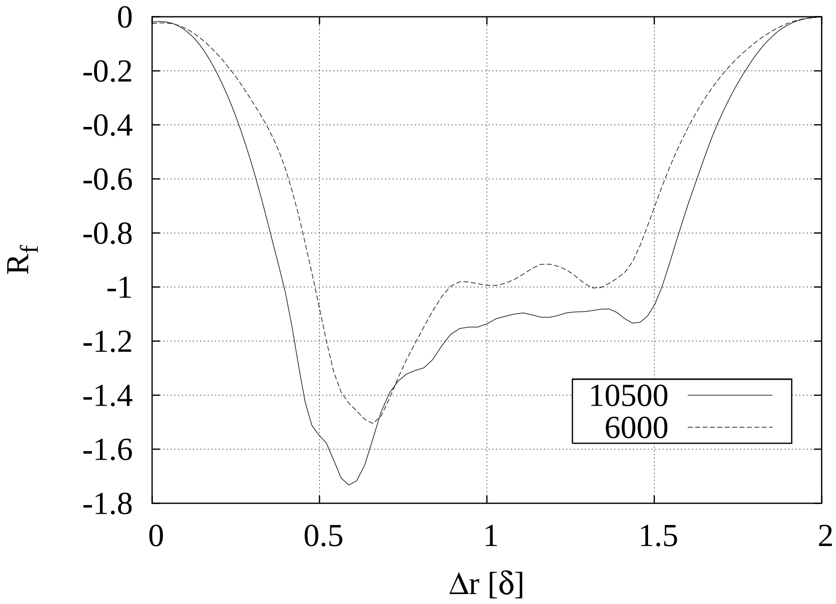

Figure 5.5: Richardson equivalent flux number R_f for $R_i = 10500$ (continuous line) and $R_i = 6000$ (dashed line), with outer cylinder at rest.

$\overline{w}^+$ at the inner wall is plotted in logarithmic (local) scale and compared with three logarithmic laws proposed in literature: (1) $2.55 \ln \Delta r^+ + 4.7$ by [7] for a plane Couette flow at $R_\tau = 52$; (2) $2.5 \ln \Delta r^+ + 4.6$ by [61] for a plane Couette flow at $R_\tau = 82.2$; (3) $2.5 \ln \Delta r^+ + 5.5$ by [59] for a plane channel flow at $R_\tau = 180$. The first law seems to agree best with our data, but just for few, around 20, wall units, since the velocity profile becomes very flat in the central part of the channel (see fig. 5.3) and cannot follow a logarithmic profile.

The reason for the lack of logarithmic law can be ascribed to the low value of R_i. As noted in [106], “no significant region of logarithmic variation of velocity can exist” for “any flow of Reynolds number less than 20000” in a TCF with outer cylinder at rest [2]. This means that owing to the large-scale structures that occupy the central part of the gap, a logarithmic equilibrium layer exists only very near the wall when the Reynolds number is large enough. We are planning to carry out in the near future cases with $R_\tau \approx 200 - 250$, in order to analyse whether at this R_τ, which guarantees a fully developed turbulence for the plane channel flow, a logarithmic layer does indeed appear.

---

[2] For the sake of completeness we note that the logarithmic layer proposed in [106] is $2.44 \ln \Delta r^+ + 4.4$ valid for each wall.

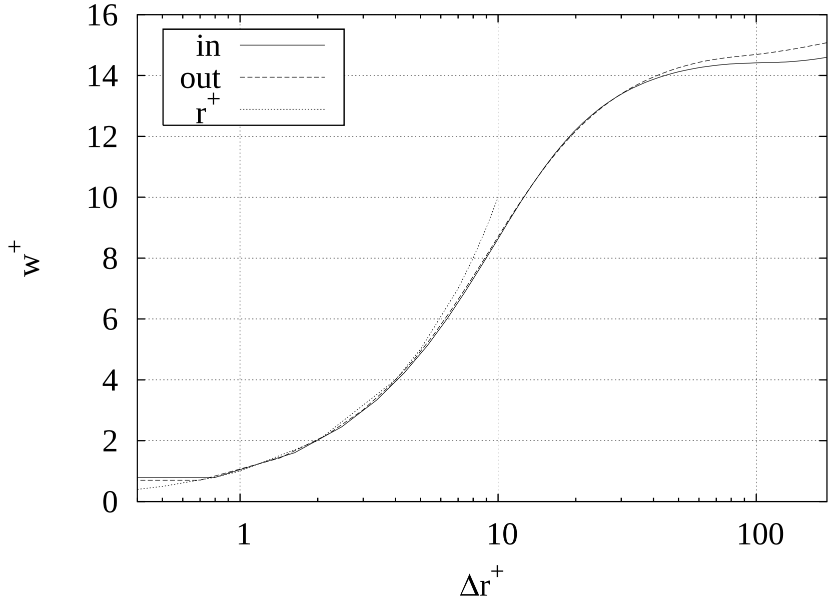

Figure 5.6: Mean azimuthal velocity $\overline{w}^{+}(\Delta r^{+})$ in local logarithmic scale for $(R_i, R_o) = (10500, 0)$, at the inner (continuous line) and outer (dashed line) wall. Comparison with the sub-layer law r^{+} (dotted line).

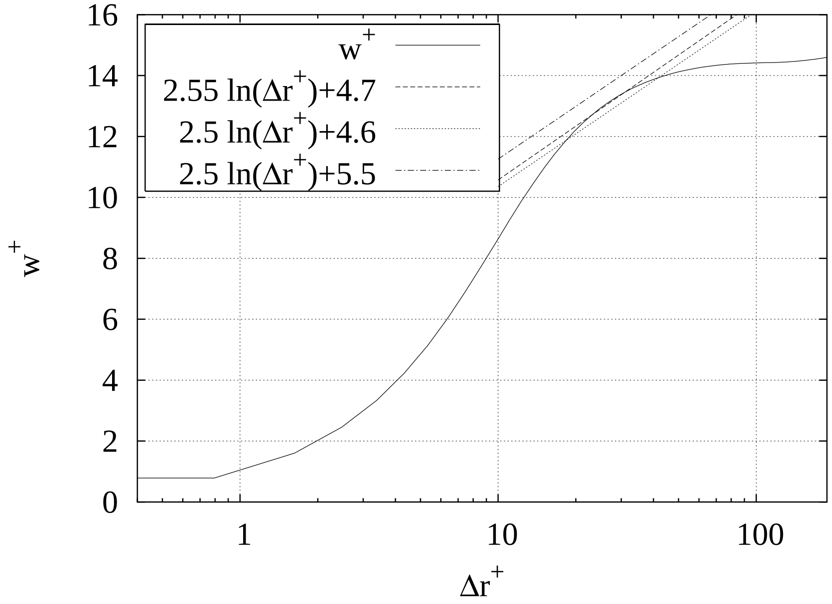

Figure 5.7: Logarithmic plot of the mean azimuthal velocity $\overline{w}_i^{+}(\Delta r^{+})$ (continuous line) for inner cylinder at $(R_i, R_o) = (10500, 0)$. Comparison with logarithmic laws proposed in literature.

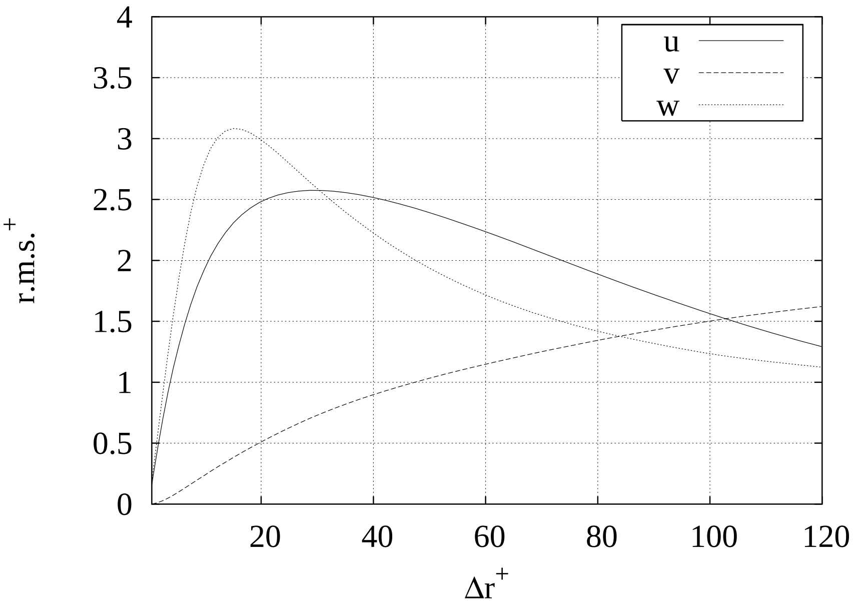

Figure 5.8: r.m.s. values of velocity vector non-dimensionalized by local u_τ, at the inner wall, for $(R_i, R_o) = (10500, 0)$: u is the continuous line, v is the dashed line, and w is the dotted line.

5.4.2 Statistical moments

We have also analysed the behaviour of flow through the root mean square (r.m.s., hereinafter) value of the velocity and vorticity fluctuations. The r.m.s. defines the squared root of the average of the quadratic difference between the instantaneous flow and the mean flow; here, as mean flow we consider an average in time as well as in the homogeneous directions.

In figs 5.8 and 5.9 we have plotted the behaviour of the three components of the velocity vector on the inner and outer walls, scaled with the local friction velocities at $R_i = 10500$. At the outer wall the turbulence intensities are higher than at the inner one. The azimuthal component is the predominant one near both walls, and shows a peak at $r^+ \approx 15$ for both walls; moreover, close to the walls, it assumes slightly higher values than in the plane Couette channel (see fig. 5.10 by [61]), which is the limit for $\eta \to 1$ of our problem. The axial and radial components too have r.m.s. values that are remarkably higher than in the case of Couette channel. This fact could depend on a redistribution of the turbulence intensities of the azimuthal component operated by the large-scale structures. We note that the behaviour of the turbulence intensities is in accordance with that supposed by MacPhail and cited in Townsend [116].

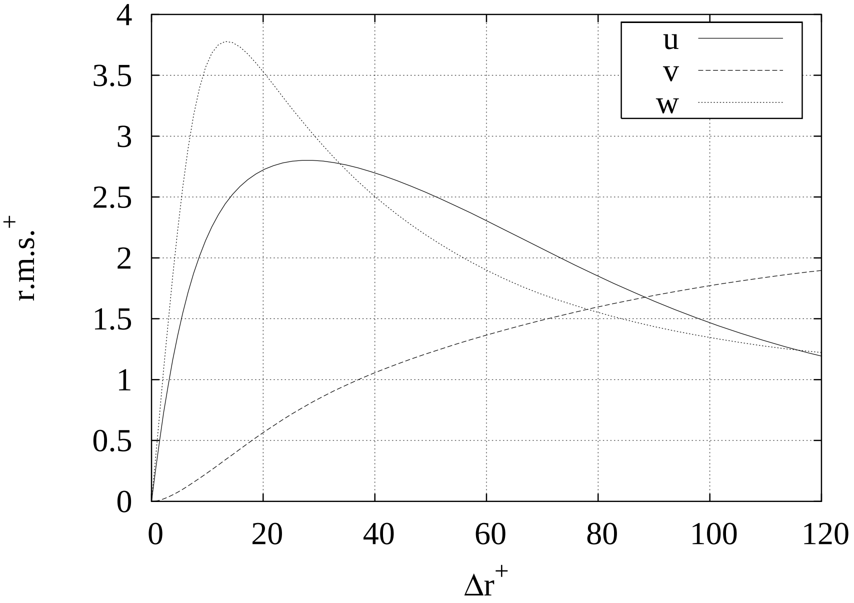

Figure 5.9: r.m.s. values of velocity vector non-dimensionalized by local u_τ, at the outer wall, for $(R_i, R_o) = (10500, 0)$: u is the continuous line, v is the dashed line, and w is the dotted line.

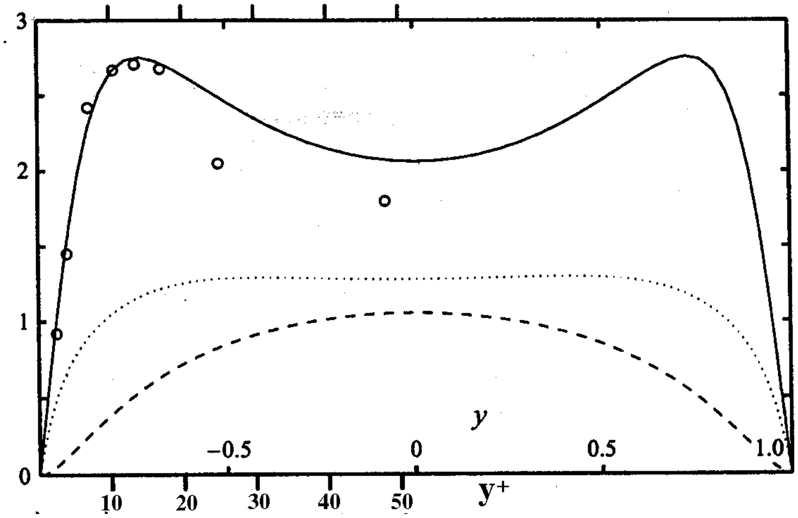

Figure 5.10: r.m.s. values of velocity components, non-dimensionalized by u_τ, by [61] ($R_\tau = 52$): the continuous line is the streamwise component, the dashed line is the radial conponent, and the dotted line is the spanwise component.

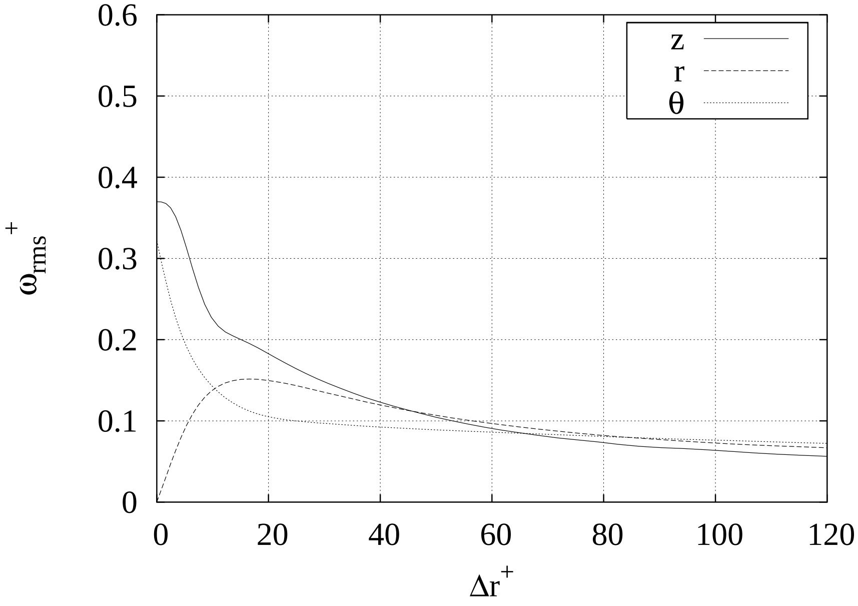

Figure 5.11: r.m.s. value of the vorticity $\overline{\omega}^{+}_{rms}$ for the z- (continuous line), r- (dashed line), and θ-component (dotted line) at the inner wall, for $(R_i, R_o) = (10500, 0)$.

The r.m.s. of the three components of the vorticity vector, scaled in viscous local units, are shown in figs 5.11 and 5.12. The analysis of these plots suggests that the azimuthal and axial component of the vorticity vector are higher near the outer wall than near the inner, whereas the opposite is true for the radial component. The behaviour of the axial and radial components is quite similar to those of the same component for the $\eta = 1$ limiting case computed by [61], however the azimuthal streamwise component is different. This effect too could be a consequence of the mean motion generated by the large-scale structures.

While in the case of flow in straight channels it is possible to derive an analytical expression for the total shear, sum of Reynolds stress and mean flow contribution, as a function of the wall-normal coordinate, in this case such a simple relation does not exist. In fact, starting from the azimuthal component of the momentum equation written for a turbulent flow, if we make the hypothesis of a statistically stationary turbulent flow and use the continuity equation, the relation

$$\nu \frac{\partial}{\partial r}\left[\frac{1}{r}\frac{\partial}{\partial r}(r\overline{w})\right] - \frac{1}{r^2}\frac{\partial}{\partial r}\overline{[r^2 v' w']} = 0, \tag{5.5}$$

can be obtained (see Stuart [110]), which cannot be integrated to give the

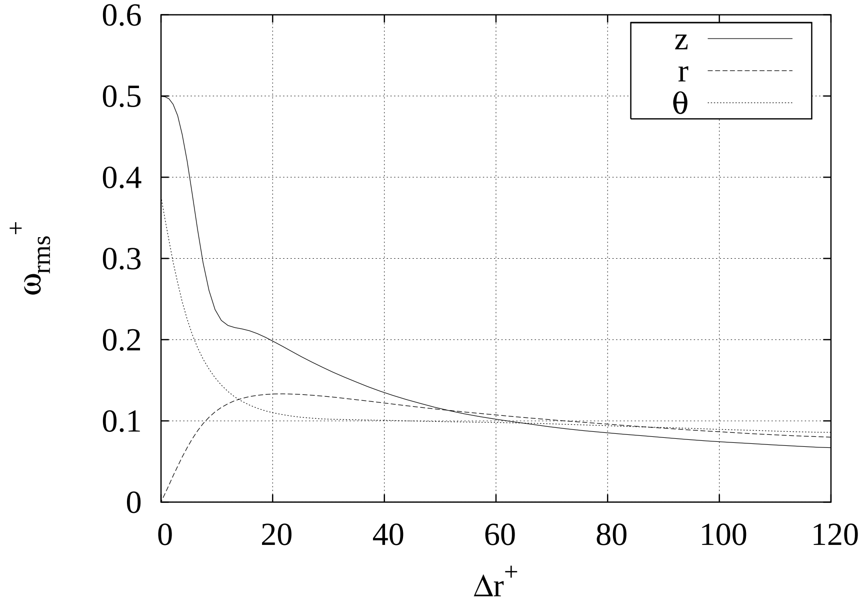

Figure 5.12: r.m.s. value of the vorticity $\overline{\omega}^+_{rms}$ for the z- (continuous line), r- (dashed line), and θ-component (dotted line) at the outer wall, for $(R_i, R_o) = (10500, 0)$.

total strain. The turbulent Reynolds stress $-\overline{v'w'}$, together with the viscous stress $\nu r[\partial(\overline{w}r^{-1})/\partial r]$ and the total stress, sum of the two previous terms, are plotted in fig. 5.13. An asymmetry can be easily observed, particularly in the centre of the gap for the turbulent stress and at the walls for the viscous stress, however when non-dimensionalized for the proper local u_τ, the latter asymmetry almost disappears.

Higher order statistics, i.e. the skewness (S) and flatness (F) factor, are depicted respectively in figs 5.14 and 5.15. From the results of the corresponding planar case by [61], we know that S is anti symmetric to the channel centreline, while F is symmetric. The present results do not show a particular symmetry for S, though the azimuthal component is almost anti-symmetric, while F is almost symmetric for all but the azimuthal component. We note that the skewness of the radial and azimuthal components of the velocity vector is quite different from the value of 0 which is that of a Gaussian distribution. As in the case of plane Couette flow the z component should be zero for symmetry reasons. Its very small values assesses the adequacy of the statistical sample. The flatness factor is nowhere close the value of 3 corresponding to a Gaussian probability distribution function. The flatness of the r component has its maximum value at the outer cylinder wall, the θ

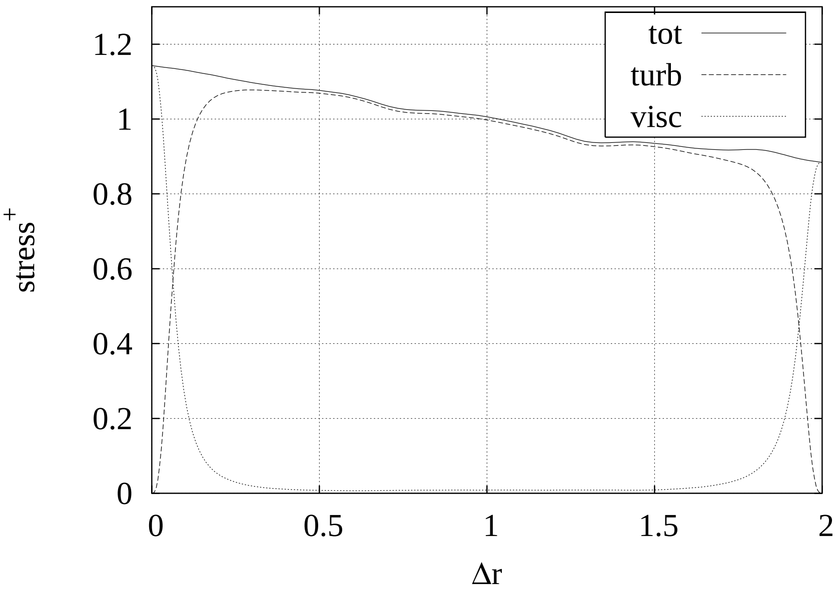

Figure 5.13: Total stress (continuous line), turbulent Reynolds stress (dashed line) and viscous stress (dotted line) non-dimensionalized by global u_τ, for $(R_i, R_o) = (10500, 0)$.

component shows two local maxima at a distance $\Delta r^+ \approx 85$ from both the walls, and the z component has its maximum slightly above the centre of the gap.

5.5 Turbulent Taylor vortices

5.5.1 Correlations and spectra

The axial monodimensional power spectral density functions of the velocity components,

$$\Phi_{\alpha,p}(\alpha; r) = \int_{-m_M}^{m_M} |\hat{u}_p(\alpha, m; r)|^2 \frac{\mathrm{d}m}{r}, \tag{5.6}$$

where $p = r, z, \theta$, are shown in fig. 5.16, for the $R_i = 10500$ case evaluated at the centre of the gap; we note that the radial and azimuthal components show peaks at multiple of the basic wavenumber, as a consequence of the large-scale structures; the axial component has a smooth behaviour at low α, at least in this radial position at the centre of the gap. All the spectra show a rapid decay for small-scales with approximatively 8 order of magnitude between the energy-containing scales and the smallest resolved scales.

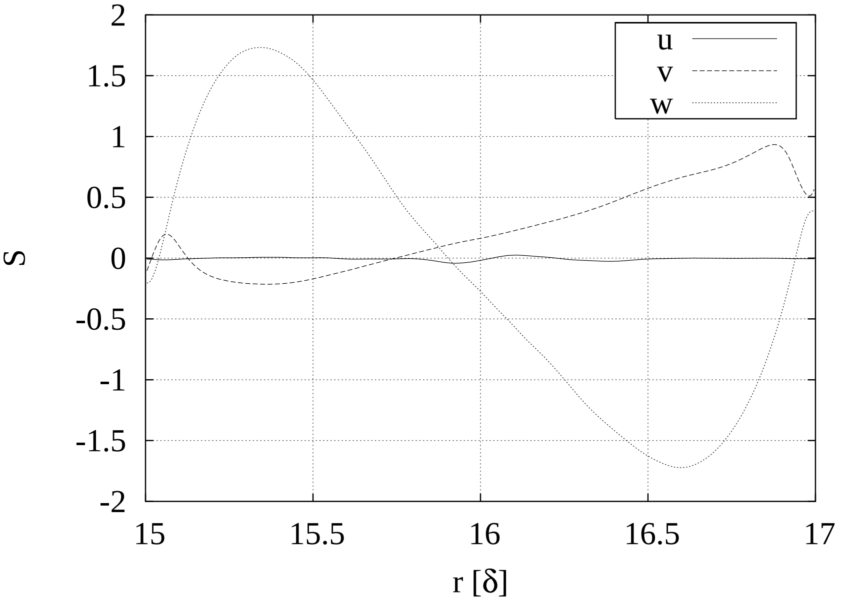

Figure 5.14: Skewness factor $S(r)$ of velocity vector for $(R_i, R_o) = (10500, 0)$: u (continuous line), v (dashed line), and w (dotted line) component.

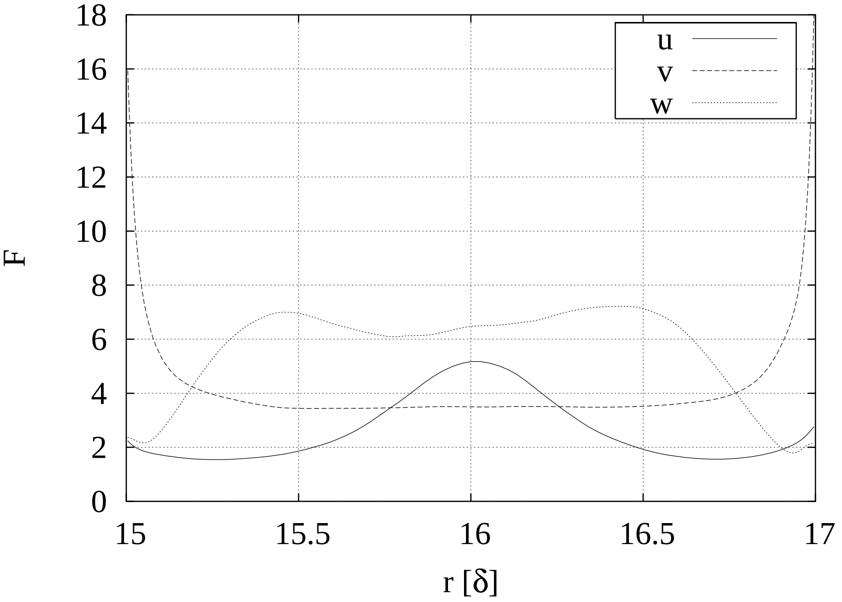

Figure 5.15: Flatness factor $F(r)$ of the velocity vector for $(R_i, R_o) = (10500, 0)$: w (continuous line), v (dashed line), and w (dotted line) component.

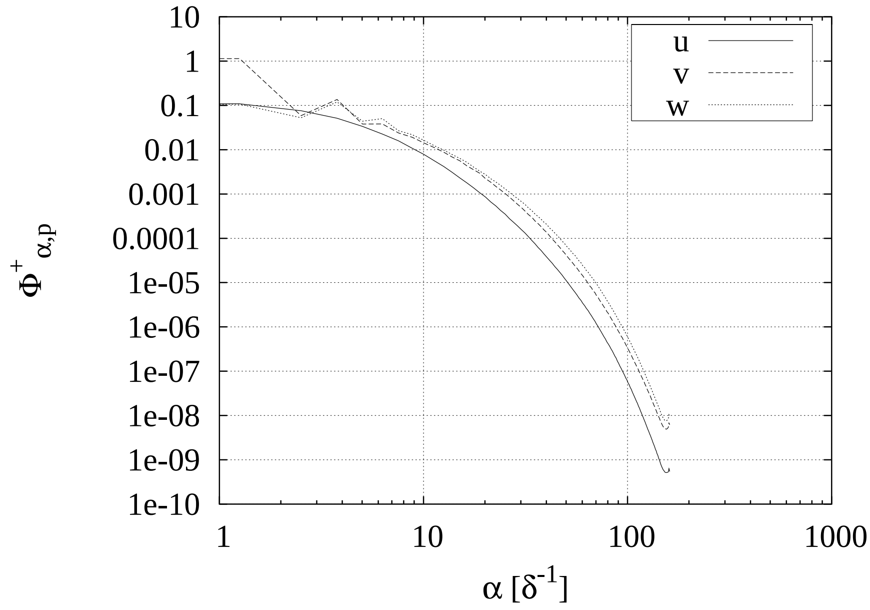

Figure 5.16: Monodimensional spectra of velocity $\Phi^+_{\alpha,p}(\alpha;\mathcal{R}_c)$ as a function of the axial wavenumber α, for $(R_i, R_o) = (10500, 0)$.The continuous line is u, the dashed line is v and the dotted line is w.

The azimuthal monodimensional power spectral density functions of the velocity components is defined as:

$$\Phi_{m,p}(m;r) = \int_{-\alpha_M}^{\alpha_M} |\hat{u}_p(\alpha, m; r)|^2 \mathrm{d}\alpha. \tag{5.7}$$

The azimuthal spectra are shown in fig. 5.17, for the $R_i = 10500$ case evaluated at the centre of the gap; they do not show any pile-up at high wavenumbers, and the difference between the energy-containing scales and the smallest scales is 5 order of magnitude.

The mono-dimensional correlation coefficients can be easily obtained from the power spectra, by recalling that they form a Fourier-transformed pair:

$$R_{z,p}(z;r) = \int_{-\alpha_M}^{\alpha_M} \Phi_{\alpha,p}(\alpha;r) e^{\iota\alpha z} \frac{\mathrm{d}\alpha}{2\pi}, \tag{5.8}$$

$$R_\theta(\theta;r) = \int_{-m_M}^{m_M} \Phi_{m,p}(m;r) e^{\iota m\theta} \frac{\mathrm{d}m}{2\pi}. \tag{5.9}$$

$R_{z,v}$ evaluated at a distance from the inner wall of 4.3 wall units shows a minimum at a distance of around 27 wall units (see fig. 5.18), which is in good agreement with the value of 30 evaluated for the dimension of the quasi

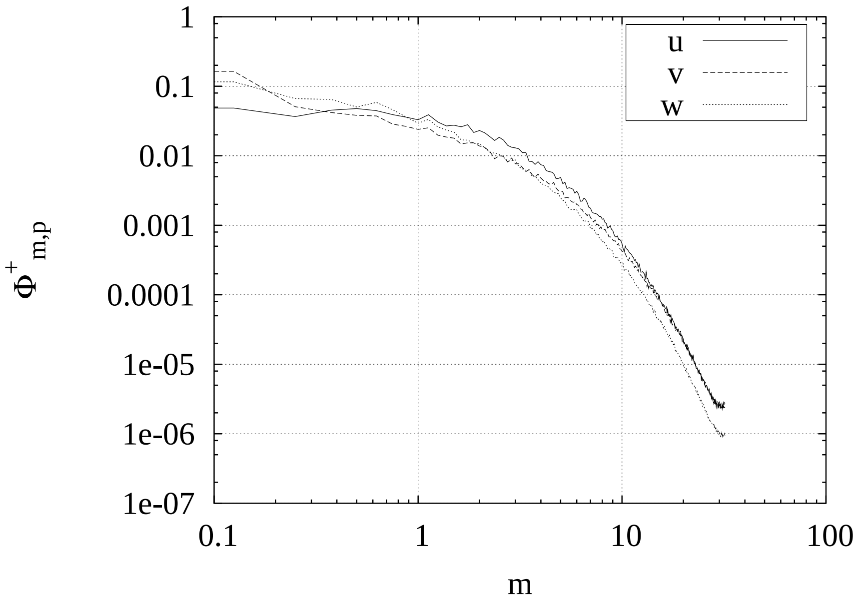

Figure 5.17: Monodimensional spectra of the velocity $\Phi^+_{m,p}(m;\mathcal{R}_c)$ as a function of the azimuthal wavenumber m, for $(R_i, R_o) = (10500, 0)$. The continuous line is u, the dashed line is v and the dotted line is w.

streamwise vortices in the plane channel flow (see [59]); the $R_{z,u}$ and $R_{z,w}$, at the same distance, have both non zero values for the large-scale correlation. While in a standard channel flow this would be an indication of insufficient length of the computational domain, we recall that in the present case the presence of large-scale structures with very large longitudinal size makes this picture less clear. This issue will be addressed in the next section when the contribution of the large-scale structures will be removed from the statistics.

$R_{\theta,v}$ evaluated at 4.3 wall units reaches a plateau, which is slightly above the zero value, at around 180 wall units (see fig. 5.19). The $R_{\theta,u}$ and $R_{\theta,w}$ have both non zero values for the large-scale correlation. As discussed above, the large-scale structures are envisaged as responsible for this behaviour.

5.5.2 The tracking of TTV

As stated above, a possible explanation for the non-zero value of the correlation coefficients at large distance, as in figs 5.18 and 5.19, is the presence of large-scale structures that fill the gap. As shown by the axial spectra these structures corresponds to the first axial mode, moreover they are slowly dependent from the azimuthal direction, so we could track the behaviour of these structures by analysing the phases and amplitudes of the $(1, 0)$-mode

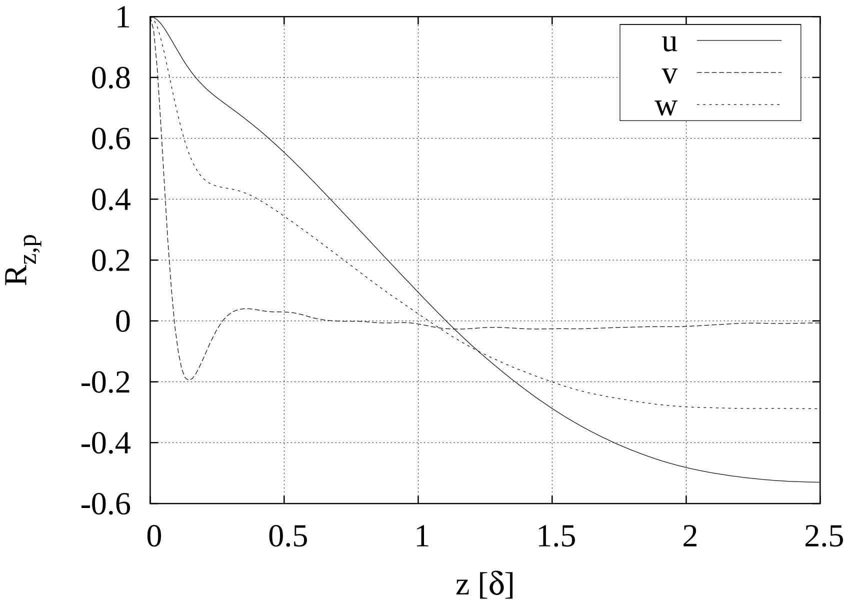

Figure 5.18: Monodimensional correlation the velocity $R_{z,p}(z)$ as a function of the axial distance at $\Delta r^+ = 4.3$ from the inner wall for $(R_i, R_o) = (10500, 0)$. The continuous line is u, the dashed line is the v and the dotted line is the w.

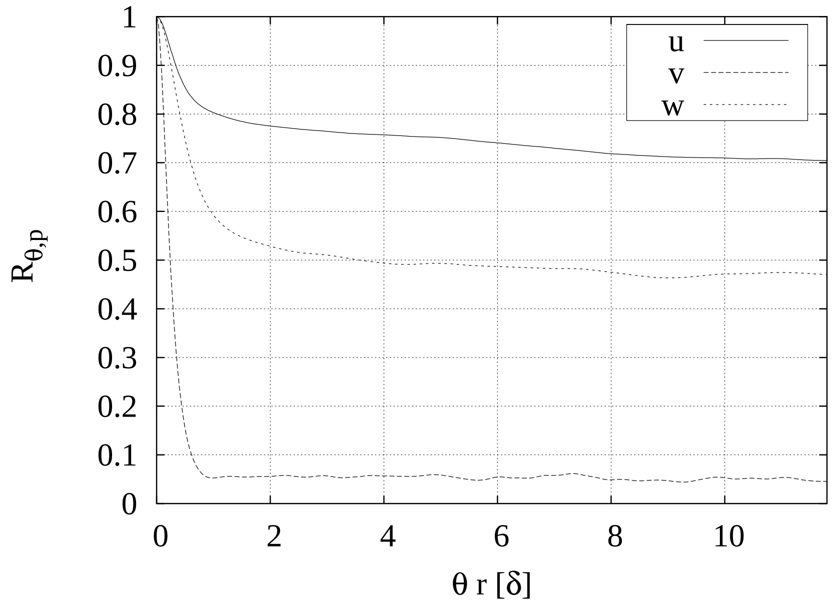

Figure 5.19: Monodimensional correlation the velocity $R_{\theta,p}(\theta r)$ as a function of the azimuthal distance at $\Delta r^+ = 4.3$ from the inner wall for $(R_i, R_o) = (10500, 0)$. The continuous line is u, the dashed line is the v and the dotted line is the w.

of the velocity vector. We note that we should consider also the $(-1,0)$-mode, but the properties of the Fourier transform guarantee that $\hat{\mathbf{v}}_{1,0} = \hat{\mathbf{v}}^*_{-1,0}$, where the star means the complex conjugated; so the $(-1,0)$-mode has a π-shift in the phase diagram, and the same amplitude of the $(1,0)$-mode. In figs 5.20(a)–5.22(a) we have plotted the phases $\phi(\hat{\mathbf{v}}_{1,0})(r,t)$ of the three components of the $(1,0)$-mode velocity vector for various times; we can see that the phases $\phi(\hat{v}_{1,0}$ and $\phi(\hat{w}_{1,0}$ change slightly with both time and radial position, which is an indicator that the structures do not have a large drift in time. The large jump in the fig. 5.20(a) is due to π-shift experienced by the $(1,0)$-mode axial velocity in the passage from the inner half to the outer one. The amplitudes $|\hat{\mathbf{v}}_{1,0}|(r,t)$ of the three components of the the $(1,0)$-mode velocity vector for various times have been plotted in figs 5.20(b)–5.22(b). Consistently with our interpretation of this mode as a TTV related, the axial (see fig. 5.20(b)) and azimuthal (see fig. 5.22(b)) component show maxima close to the wall, whereas the radial component (see fig. 5.21(b)) has a maximum in the centre of the gap; all the components do not vary substantially in time.

5.5.3 TTV contribution to turbulence statistics

Once established that the large-scale structures are almost steady in time, we want to isolate their effect from those of the surrounding turbulence. By following [85] and [124], who have used the same strategy for the turbulent Dean flow, we decompose the velocity field $u_p = u_p(z,r,\theta,t)$ in a mean and fluctuating part by means of different operators:

$$u_p(z,r,\theta,t) = u_p^{'}(z,r,\theta,t) + \overline{u}_p(r), \tag{5.10}$$

$$u_p(z,r,\theta,t) = u_p^{''}(z,r,\theta,t) + \tilde{u}_p(z,r), \tag{5.11}$$

where the former (over-bar) is a global average over homogeneous coordinates and time, and the latter (tilde) is an average in the streamwise direction and in time. The latter average keeps alive the large-scale contributes, while the former filters it. From equations (5.10) and (5.11) it is possible to derive

$$u_p^{'} = (\tilde{u}_p - \overline{u}_p) + u_p^{''}, \tag{5.12}$$

which expresses the instantaneous flow field $u_p^{'}$ as a sum of two contributions: the former $(\tilde{u}_p - \overline{u}_p) = (u_p^{'} - u_p^{''})$ depends on the TTV structures, and the latter $u_p^{''}$ is the filtered turbulence contribution. The $(\tilde{u}_p - \overline{u}_p)$ field is a function of just the axial and radial coordinates, so it is a two-dimensional field for which a streamfunction $\Psi(z,r)$, as in eq. (3.5), can be obtained easily. In fig. 5.23 the streamfunction $\Psi(z,r)$ is plotted. Two regions, associated respectively

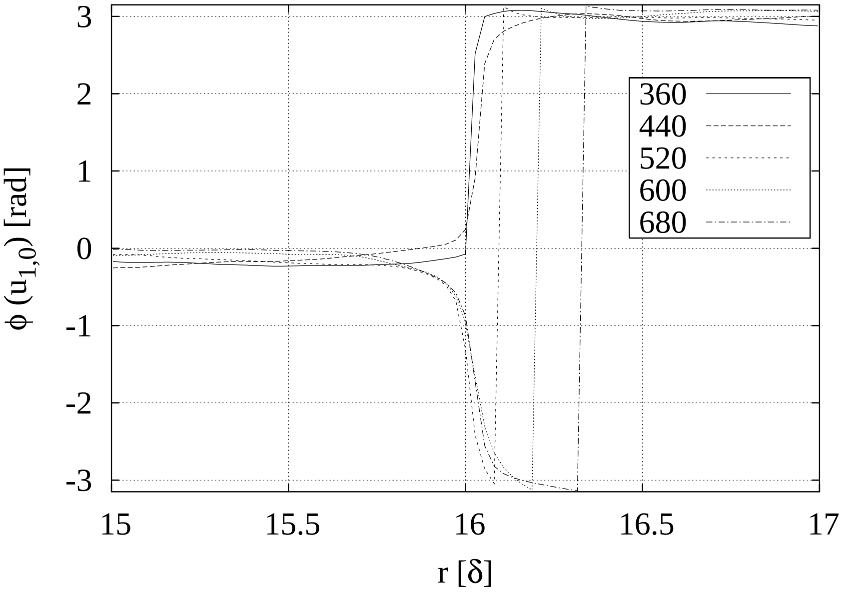

(a) $\phi(\hat{u}_{1,0})$

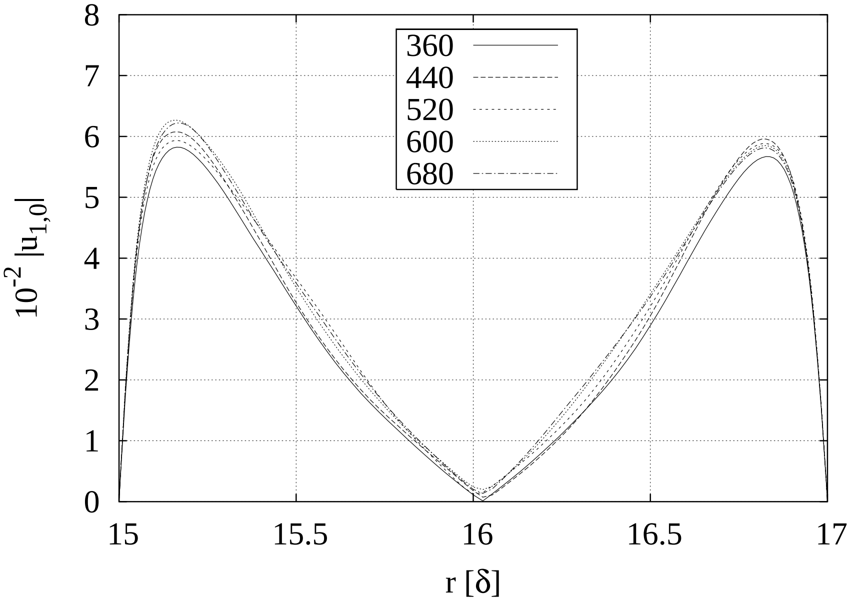

(b) $|\hat{u}_{1,0}|$

Figure 5.20: Phase and amplitude of the axial component of the $(1,0)$-mode velocity vector as a function of the radial position and for various time instants.

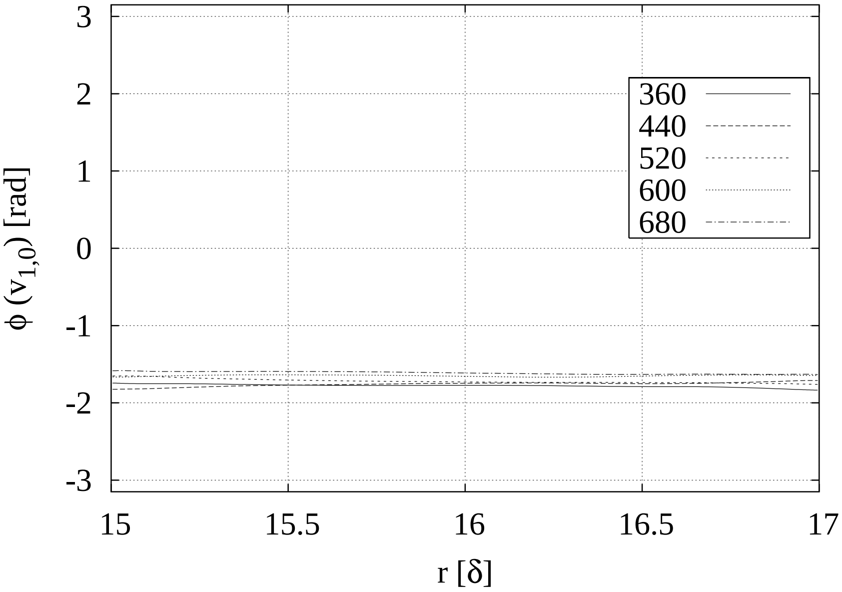

(a) $\phi(\hat{v}_{1,0})$

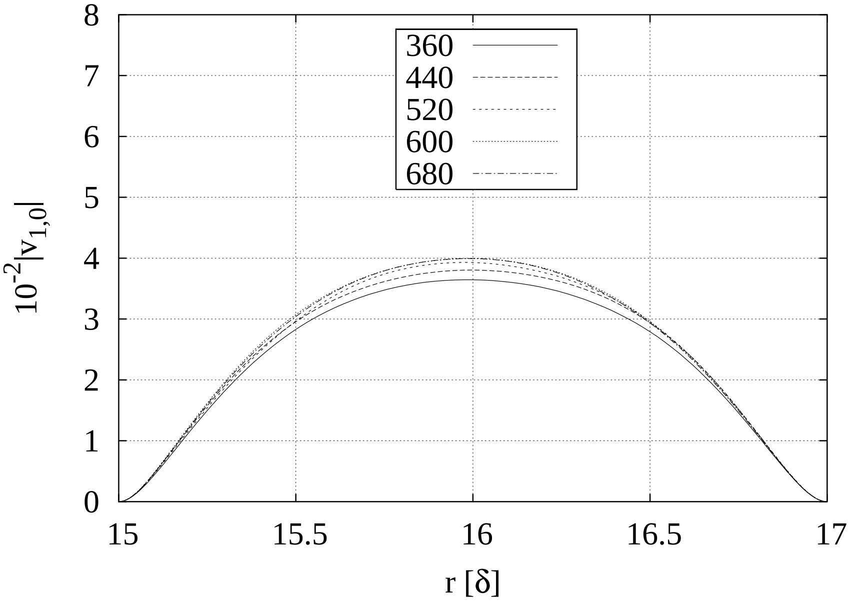

(b) $|\hat{v}_{1,0}|$

Figure 5.21: Phase and amplitude of the radial component of the $(1, 0)$-mode velocity vector as a function of the radial position and for various time instants.

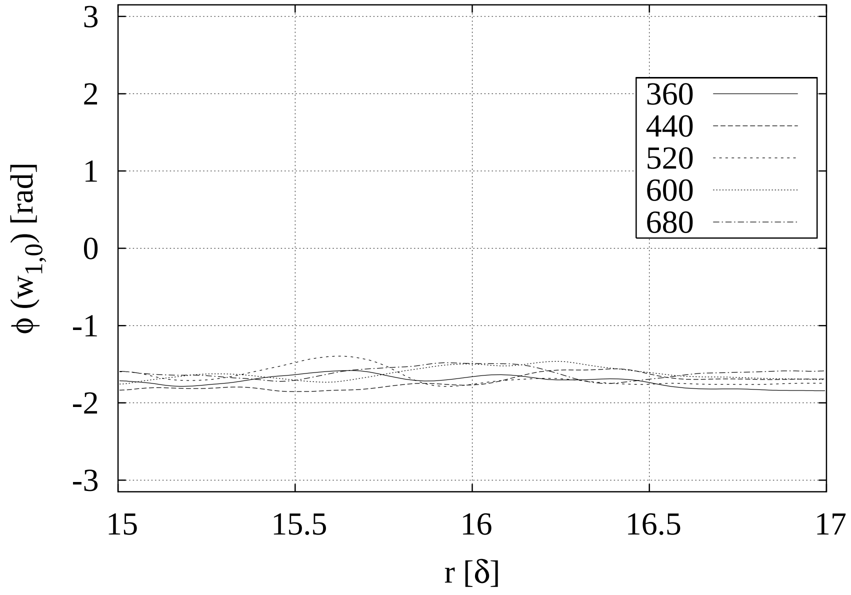

(a) $\phi(\hat{w}_{1,0})$

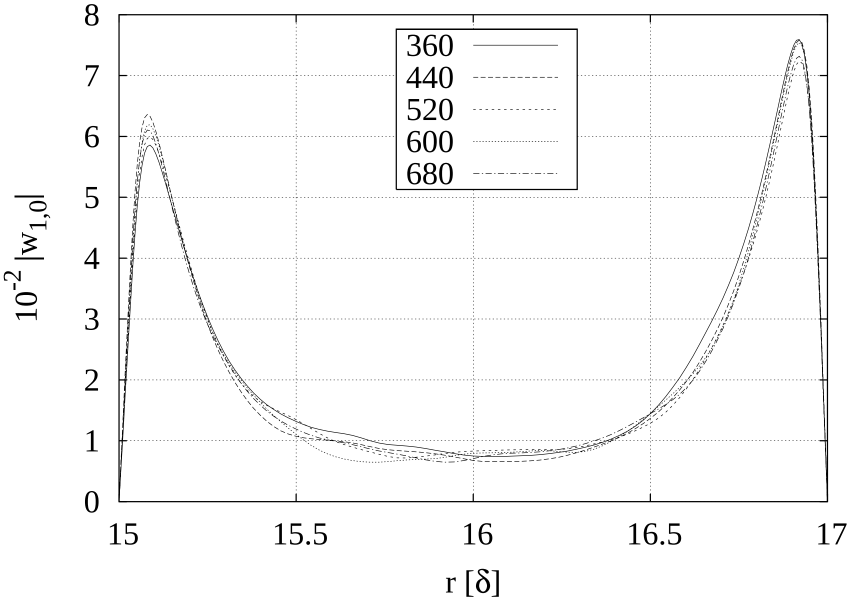

(b) $|\hat{w}_{1,0}|$

Figure 5.22: Phase and amplitude of the azimuthal component of the $(1, 0)$-mode velocity vector as a function of the radial position and for various time instants.

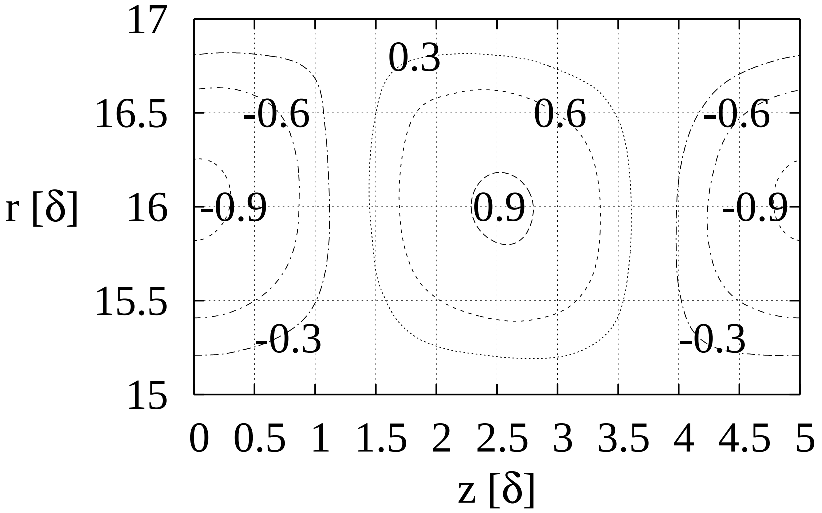

Figure 5.23: Streamfunction $\Psi(z, r)$ of the average velocity field $(\tilde{u}_p - \overline{u}_p)$. The numbers represent the values of the corresponding iso-streamfunction loci.

with positive and negative values of Ψ, appear and fill the most part of the gap. They have the typical shape of the counter-rotating vortex pair and a comparison with the streamfunction resulting from the computation by [42] (as in fig. 7b) for a smaller R_i shows that these large-scale structures can be confidently interpreted as TTV. Both regions are not symmetric to the centreline; the jet-like structures already observed by [42] and [19] are present in correspondence of the outflow region, at $z \approx 1.2\delta$. Thus the above-described averaging procedures could prove itself to be effective in capturing the main features of the TTV structures.

By applying the eq. (5.12) we can recast the second order statistics for the p-component of the velocity vector as,

$$\overline{(u_p')^2} = \overline{(u_p' - u_p'')^2} + \overline{(u_p'')^2}, \tag{5.13}$$

where the squared root of the left-hand-side are the r.m.s. of the velocity vector, already plotted in figs 5.8 and 5.9. The right-hand-side in eq. (5.13)

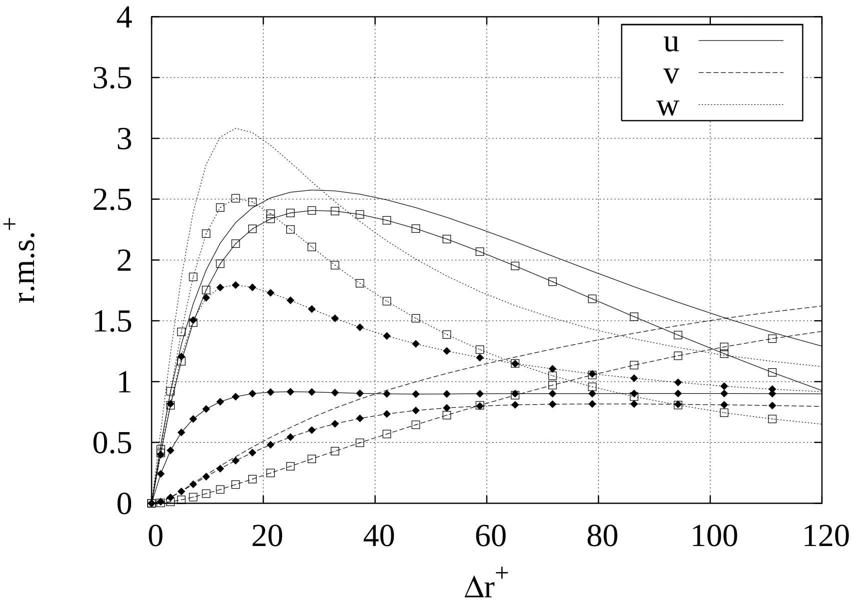

Figure 5.24: r.m.s. values of velocity at the inner wall non dimensionalized with the local u_τ, for $(R_i, R_o) = (10500, 0)$: u (continuous line), v (dashed line), and w (dotted line). The symbol □ represents $[\overline{(u'_p - u''_p)^2}]^{1/2}$, while the ⧫ symbol is $[\overline{(u''_p)^2}]^{1/2}$.

can be viewed as the sum of a TTV-dependent contribute $\overline{(u'_p - u''_p)^2}$ plus a filtered turbulent one $\overline{(u''_p)^2}$. If we want to analyse the contribution of the TTV and of the filtered turbulence to the r.m.s. of the velocity, we can simply calculate $[\overline{(u'_p - u''_p)^2}]^{1/2}$ and $[\overline{(u''_p)^2}]^{1/2}$; we note, however, that the two contributions do not sum up to give the overall r.m.s because no linear law relates them. In figs 5.24 and 5.25 the two contributions have been plotted together with the $[\overline{(u'_p)^2}]^{1/2}$, as function of the radial dimension, in the proximity of both walls. The TTV contribution $[\overline{(u'_p - u''_p)^2}]^{1/2}$ (white squares) to the turbulence intensities of the axial and azimuthal components is by far more important than the filtered turbulent one $[\overline{(u''_p)^2}]^{1/2}$ (black diamonds). However, close to the walls, the radial component v depends most on the turbulent contribution. While the TTV contribution is not symmetric at all, the turbulent contribution is almost symmetric on both walls, and appear as not dependent on the distance form the wall, at least for $\Delta r^+ > 60$; besides, the azimuthal component overwhelms the other two for all the gap width, and at the centre of the channel the three components do not differ very much. These results suggest that the great part of the turbulence intensities in the proximity of the walls is due to the presence of

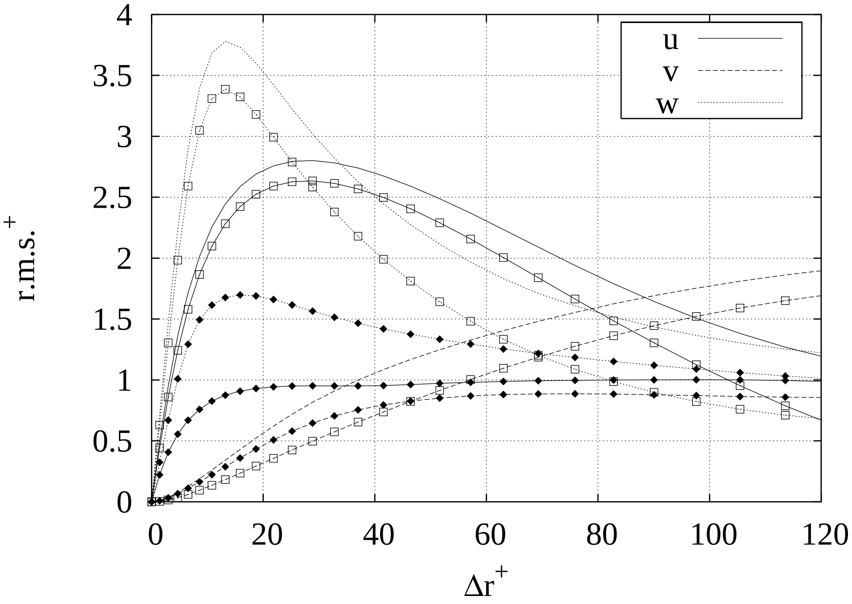

Figure 5.25: r.m.s. values of velocity at the outer wall non dimensionalized with the local u_τ, for $(R_i, R_o) = (10500, 0)$: u (continuous line), v (dashed line), and w (dotted line). The symbol $\square$ represents $[\overline{(u'_p - u''_p)^2}]^{1/2}$, while the ♦ symbol is $[\overline{(u''_p)^2}]^{1/2}$.

the TTV, whose effects are completely different form those produced by the surrounding turbulence which becomes, at least for the axial and azimuthal components, the most important factor in the centre of the channel. A comparison between the filtered contribution and fig. 5.10 shows a qualitative agreements between the turbulent Couette plane flow and the filtered part of the present simulation.

Also the turbulent contribution to the total viscous stress can be analysed by dividing the contribution in terms of TTV and filtered-turbulence; in fact, the relation

$$-\overline{(v'w')} = -\overline{(v'-v'')(w'-w'')} - \overline{v''w''}, \tag{5.14}$$

holds. In fig. 5.26 the left-hand-side, already plotted in fig. 5.13, has been drawn together with the two right-hand-side contributions: the former depends from the TTV and the latter results from the filtered turbulence. It appears that the TTV contribution is higher than the filtered turbulence one for all the gap length except a thin layer ($\Delta r^+ < 10$) close to the inner wall; the TTV-related shear stress is higher on the outer wall than on the inner in all the gap width, and this characteristic transfers to the overall shear due to the overwhelming importance of TTV. The filtered turbulence contribution is higher on the inner wall region than on the outer one, however once the central region of the gap is reached ($\Delta r^+ > 80$) the relative importance switches.

The same approach used for the second-order turbulence statistics can be applied to the high-order ones; in fact, by decomposing the third- and forth-order statistics through the relation given by eq. (5.12) the following expression can be derived,

$$\overline{(u_p')^3} = \overline{(u_p'-u_p'')^3} + \overline{(u_p'')^3} + 3\overline{(u_p'-u_p'')(u_p'')^2}, \tag{5.15}$$

$$\overline{(u_p')^4} = \overline{(u_p'-u_p'')^4} + \overline{(u_p'')^4} + 6\overline{(u_p'-u_p'')^2(u_p'')^2} + 4\overline{(u_p'-u_p'')(u_p'')^3}, \tag{5.16}$$

From these statistics the skewness $S = \overline{(u_p')^3}/[\overline{(u_p')^2}]^{3/2}$ and flatness $F = \overline{(u_p')^4}/[\overline{(u_p')^2}]^2$ factors can be derived easily. In fig. 5.27 we have plotted the contribution of the TTV $\overline{(u_p'-u_p'')^3}/[\overline{(u_p')^2}]^{3/2}$ and those of the filtered turbulence $\overline{(u_p'')^3}/[\overline{(u_p')^2}]^{3/2}$, together with the total skewness, already portrayed in fig. 5.14. The dependence on the TTV is again strong, though also the other contributes are now important; in particular the TTV imposes their shape to the total skewness in the central part of the gap. More than the contribution of u_p'' to the total skewness is important to analyse the skewness factor of the filtered turbulence velocity field, defined as $\overline{(u_p'')^3}/[\overline{(u_p'')^2}]^{3/2}$, which has been plotted in fig. 5.28. It is possible to observe that the three components

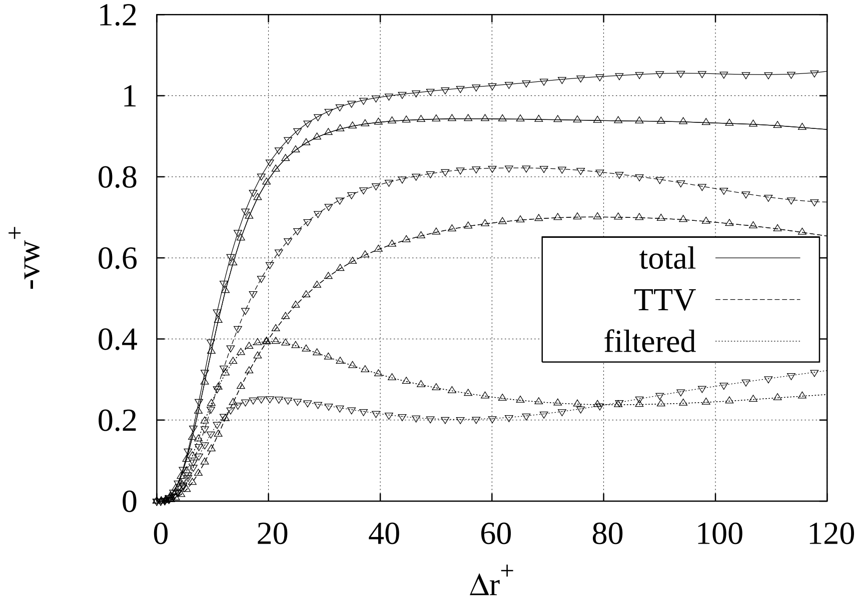

Figure 5.26: Viscous stress contribution at the inner ($\triangle$) and outer ($\bigtriangledown$) wall, for $(R_i, R_o) = (10500, 0)$. The continuous line is the total viscous stress $-\overline{(v'w')}$, the dashed line is the TTV contribution $-\overline{(v'-v'')(w'-w'')}$, and the dotted line is the filtered turbulent contribution $\overline{v''w''}$.

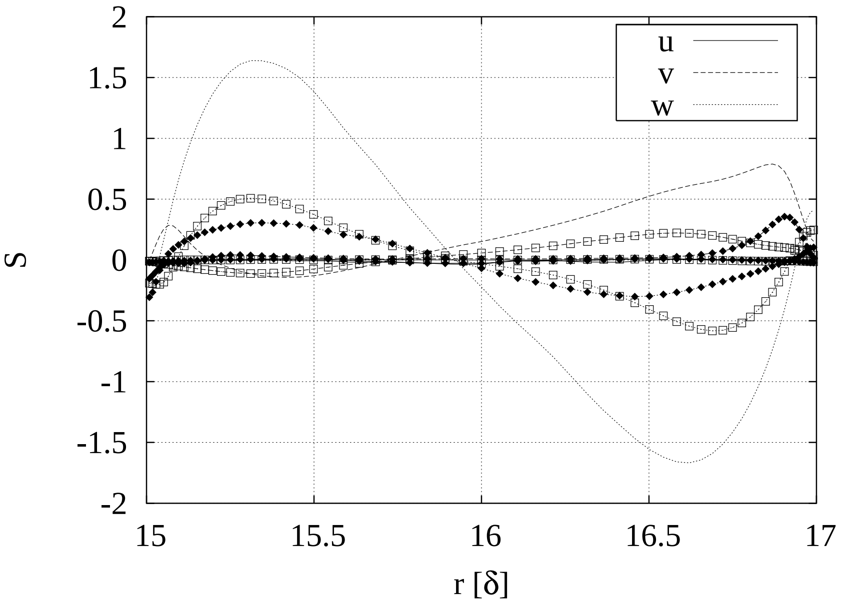

Figure 5.27: Skewness factor $S(r)$ of velocity vector for $(R_i, R_o) = (10500, 0)$: u (continuous line), v (dashed line), and w (dotted line) component. The symbol □ represents $\overline{(u'_p - u''_p)^3}/[\overline{(u'_p)^2}]^{3/2}$, while the ◆ is $\overline{(u''_p)^3}/[\overline{(u'_p)^2}]^{3/2}$.

qualitatively agree with the turbulent Couette plane flow data given by [61].

In fig. 5.29 we have plotted the contribution of the TTV $\overline{(u'_p - u''_p)^4}/[\overline{(u'_p)^2}]^2$ and those of the filtered turbulence $\overline{(u''_p)^4}/[\overline{(u'_p)^2}]^2$, together with the total flatness, already portrayed in fig. 5.15. The dependence on the TTV is now very feeble and the turbulence-related contribution is now more important for all the flatness factor components. By plotting, as in fig. 5.30, the flatness factors of the filtered velocity field alone $\overline{(u''_p)^4}/[\overline{(u''_p)^2}]^2$ it appears that the three components of the filtered velocity field have a behaviour which is qualitatively similar to the turbulent Couette plane flow.

By subtracting the contribution of the TTV $(\tilde{u}_p - \overline{u}_p)(z, r)$ from the velocity fields it is also possible to study the behaviour of the monodimensional correlation coefficients $R''_{z,p}(z)$ and $R''_{\theta,p}(\theta r)$, which depend just on the filtered-turbulence u''_p. In figs 5.31 and 5.32 the correlation coefficients have been plotted and the large-scale correlations observed in figs 5.31 and 5.31 are now almost completely disappeared, which is consistent with the idea that the TTV have a big influence on the flow properties. However, we observe that the $R''_{z,u}$ and $R''_{\theta,u}$ still conserve some important large-scale contribution which means that not all the large-structures have been successfully elimi-

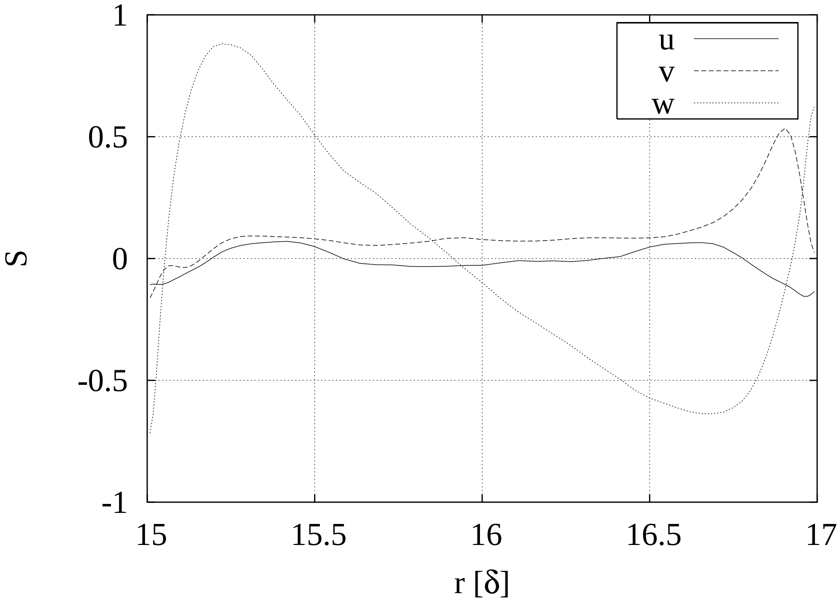

Figure 5.28: Skewness factor of the filtered turbulent velocity field $\overline{(u''_p)^3}/[\overline{(u''_p)^2}]^{3/2}$ for $(R_i, R_o) = (10500, 0)$: u (continuous line), v (dashed line), and w (dotted line) component.

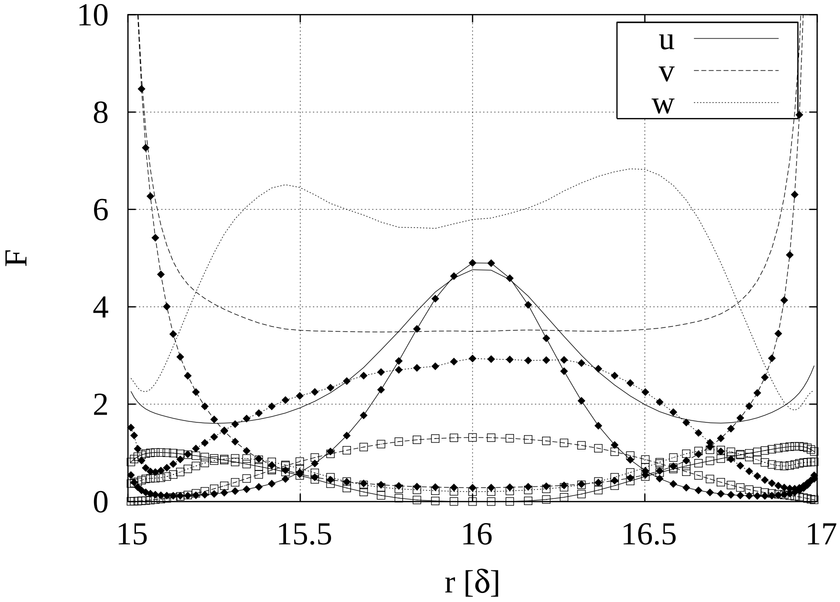

Figure 5.29: Flatness factor $F(r)$ of velocity vector for $(R_i, R_o) = (10500, 0)$: u (continuous line), v (dashed line), and w (dotted line) component. The symbol $\Box$ represents $\overline{(u'_p - u''_p)^4}/[\overline{(u'_p)^2}]^2$, while the ♦ symbol is $\overline{(u''_p)^4}/[\overline{(u'_p)^2}]^2$.

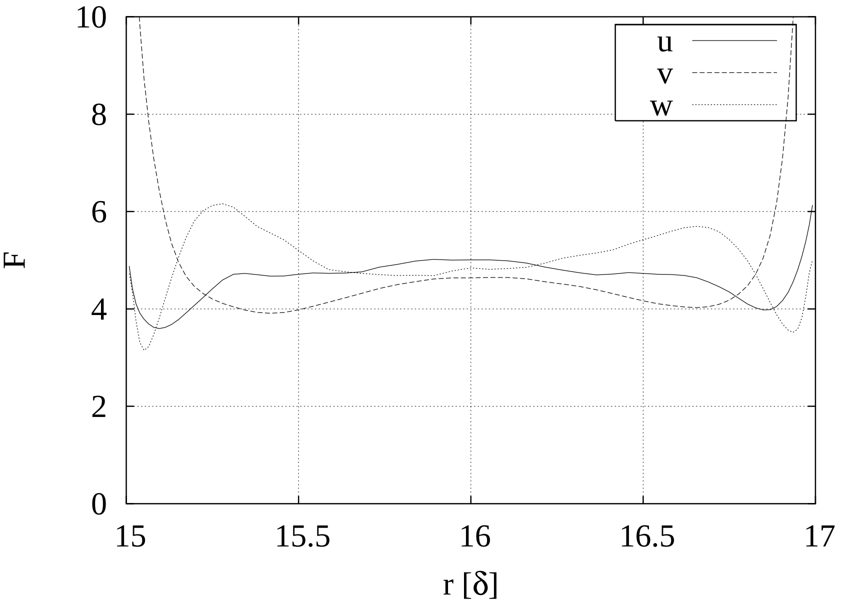

Figure 5.30: Flatness factor of the filtered turbulent velocity field $\overline{(u''_p)^4}/[\overline{(u''_p)^2}]^2$ for $(R_i, R_o) = (10500, 0)$: u (continuous line), v (dashed line), and w (dotted line) component.

nated; besides, the $R''_{z,w}$ has a local (positive) minimum around 50 wall units, which is followed by a small increase and successively leads to an almost-zero correlation.

From the filtered monodimensional correlation coefficients $R''_{z,p}(z)$ and $R''_{\theta,p}(\theta r)$, by simply inverting the formula (5.8) and (5.9), the filtered monodimensional spectra

$$\Phi''_{\alpha,p}(\alpha;r) = \int_0^{L_z} R''_{z,p}(z;r)e^{-\iota\alpha z}\mathrm{d}z, \tag{5.17}$$

$$\Phi''_{m,p}(m;r) = \int_0^{l_\theta} R''_{\theta,p}(\theta;r)e^{-\iota m\theta}\mathrm{d}\theta, \tag{5.18}$$

can be obtained. In fig. 5.33 we have plotted the axial monodimensional spectra evaluated at the centre of the gap $r = \mathcal{R}_c$. The peaks at the multiple of the first wavelength which were present in fig. 5.16 have almost completely disappeared, as expected after an average process which substantially eliminates the structures responsible for those peaks; at high wavelengths no significative change has occurred. The small peak which can be observed for $\Phi''_{\alpha,w}$ are probably a consequence of large-scale structures which have escaped from our filtering process. The azimuthal spectra $\Phi''_{m,p}(m;r)$ differs from the

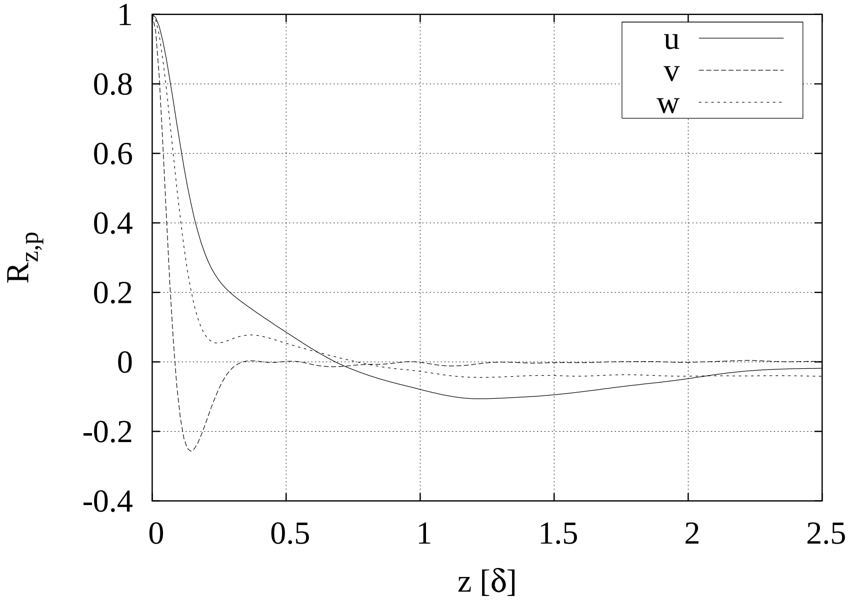

Figure 5.31: Monodimensional correlation of filtered velocity, $R''_{z,p}(z)$, as a function of the axial distance at $\Delta r^+ = 4.3$ from the inner wall for $(R_i, R_o) = (10500, 0)$. The continuous line is u, the dashed line is v and the dotted line is w.

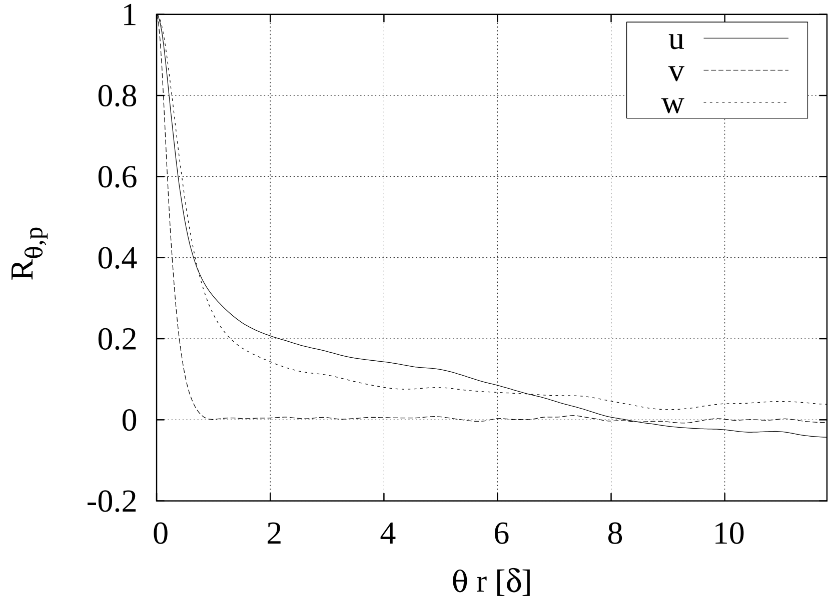

Figure 5.32: Monodimensional correlation of filtered velocity, $R''_{\theta,p}(\theta r)$, as a function of the azimuthal distance at $\Delta r^+ = 4.3$ from the inner wall for $(R_i, R_o) = (10500, 0)$. The continuous line is u, the dashed line is v and the dotted line is w.

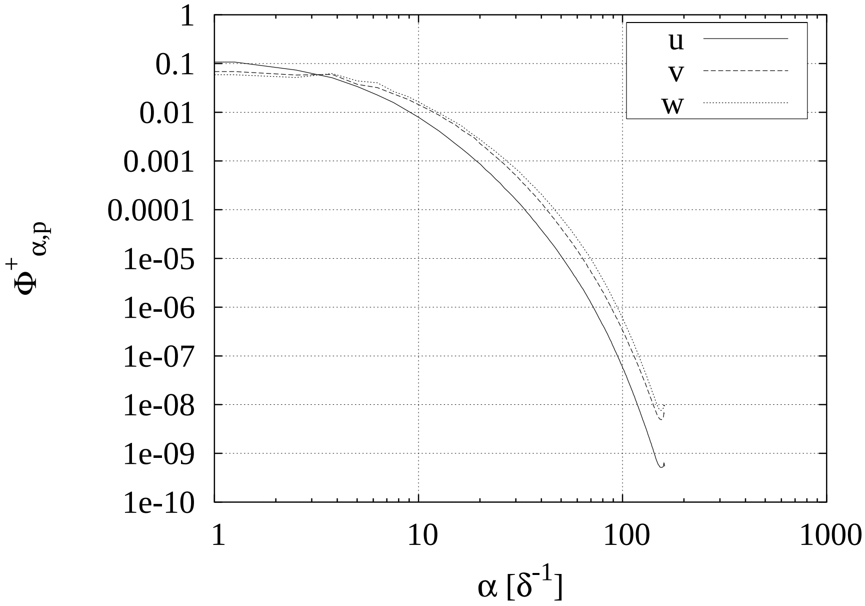

Figure 5.33: Monodimensional spectra of filtered velocity $\Phi''^{+}_{\alpha,p}(\alpha;\mathcal{R}_c)$ as a function of the axial wavenumber α, for $(R_i, R_o) = (10500, 0)$. The continuous line is u, the dashed line is v and the dotted line is w.

previously evaluated $\Phi_{m,p}(m;r)$, plotted in fig. 5.17 just for its $m = 0$ component, which disappears in a logarithmic scale and so has not been plotted again.

5.5.4 Large-scale structures visualisation

As shown in our previous analysis, and as remarkably pointed out by Barcilon et al. [5] and Barcilon & Brindley [4], the large-scale TTV and small-scale vortical structures co-exist for this geometry in turbulent regime. Besides, [4] believe that the small-scale structures "were the inflow and outflow of Görtler vortices existing in the wall-boundary-layer region", which appear close to the inner and outer walls.

In fig. 5.34 a meridional plane of iso-azimuthal velocity $w(z,r)$ for an instantaneous flow field in the case of $(R_i, R_o) = (10500, 0)$ has been plotted. The azimuthal direction has been straightened, in fig. 5.34, for the purpose of a better representation. Close to the inner and outer walls two regions of respectively high and low azimuthal velocity tend towards the centre of the channel. These regions are the outflow and inflow boundaries of a pair of TTV. Two surfaces of iso-streamfunction Ψ (see equation (3.5) and [18]), one positive (blue/dark coloured) and the other negative (yellow/grey coloured), are depicted; they appear quite similar to a pair of TTV which counter-rotate.

The inflow and outflow boundaries of the TTV push fluid from one side of the channel towards the opposite wall. By referring to fig. 5.34, on the inner wall we can trace the inflow region as a region of impinging fluid coming from the opposite half-channel, which determines high value of local wall shear stress, and the outflow one as an area of local low shear stress, determined by the movement of high azimuthal velocity from the inner wall to the centre of the channel. The first region corresponds to the blue/dark coloured stripe of fig. 5.35 where the fluctuating part of the shear at the inner wall $\tau^{'}(z,\theta;\mathcal{R}_i,t) = \tau(z,\mathcal{R}_i,\theta,t) - \overline{\tau}_i$ for an instantaneous flow field is plotted. The red/grey area corresponds to the outflow boundary of the TTV pair. It is characterized by two features: (1) red/grey coloured, wide ($50-70$ wall units), elongated (around 1000 wall units) streaks; (2) small-scale (around 200 wall units of length and 40 wall units of width) tilted ($8-10°$ in streamwise direction) structures which do not appear in the blue region. The first structures resembles those observed by [61], while the value of the tilting angle of the second is comparable with that shown in [4], instead their width is bigger than those presented in the above mentioned article, but we have to notice that our R_i is more than two times lesser than the lower limit of those considered there.

5.6 Final remarks

Direct numerical simulations of a TCF in turbulent regime have been carried out at a Reynolds number up to $R_\tau \approx 180$ based on friction velocity, viscosity of the fluid and half gap width.

The experimentally observed TTV have been recognized, for the first time to our knowledge, in a numerical simulation, and the effects produced on mean and instantaneous turbulence statistics have been analysed. An almost constant-circulation structure fills the central part of the gap, its size growing with R_i; to satisfy the boundary conditions, two shear layers develop at the cylinders walls, the thicknesses of which decrease with R_i. A viscous sublayer exists on both walls, whereas the presence of a logarithmic law for the average azimuthal velocity cannot be assessed with the present data, since the logarithmic profile in this flow should be observable only at very high Reynolds numbers. Turbulence intensities are significant not only for the azimuthal velocity, but also for the radial and axial velocity components. This last effect is a consequence of the presence of large-scale structures which contribute heavily on low-order and high order statistics. We have implemented a simple method to filter the flow fields, to the aim of separating

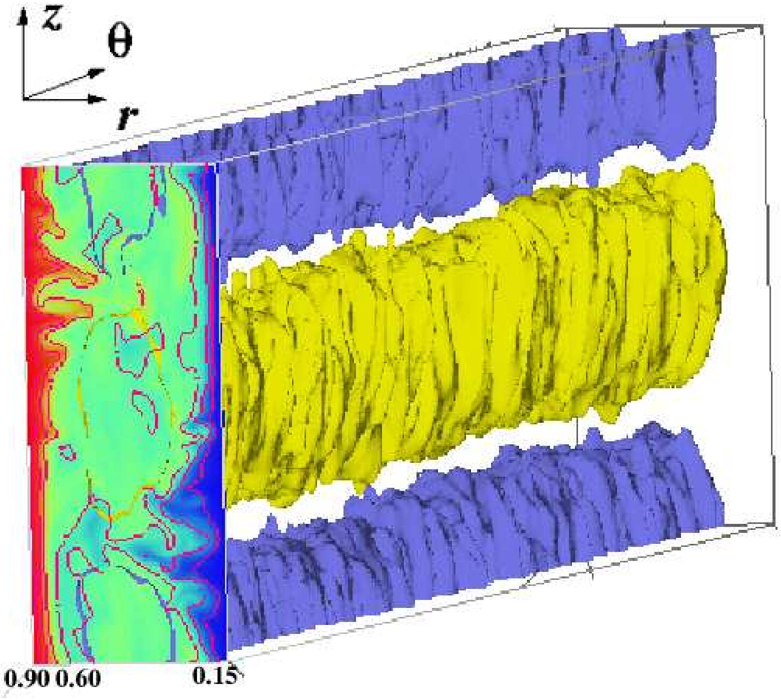

Figure 5.34: Azimuthal velocity in a plane, $w(z,r;\theta)$ (with $\Delta w = 0.15 w_i$) and iso-streamfunction surfaces for $(R_i, R_o) = (10500, 0)$: positive (yellow/grey, 0.45) and negative (blue/dark, -0.45).

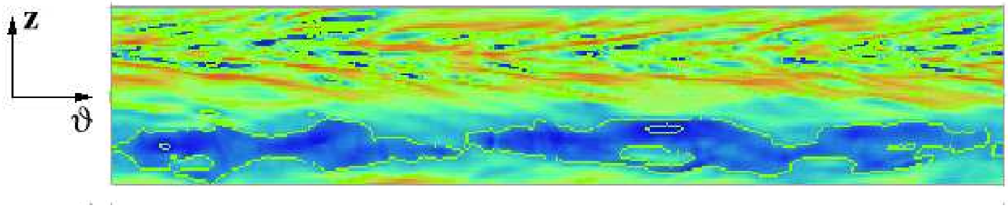

Figure 5.35: Instantaneous shear around the mean value at the inner wall $\tau'^{+}(z,\theta;\mathcal{R}_i,t)/\mu$ for $(R_i, R_o) = (10500, 0)$ ($\Delta\tau^{+} = 0.15$; positive values are depicted in blue/dark and negative in red/grey).

large- and small-scales contributions. Though the filtering process can still be improved, the obtained results show how large the effects of TTV are, and how they can be separated from the smaller scale turbulence structures.

Small-scales structures, hypothesized on theoretical consideration and observed in experiments, have also been captured. They have been observed close to the cylinders walls and they resemble the typical structures of the wall-turbulence.

CHAPTER 6

TURBULENT DEAN FLOW

In this chapter Direct Numerical Simulations of the Dean flow in turbulent regime are described. Different cases with mild and strong curvature are considered; the effect of the curvature on mean and instantaneous properties of the flow is analysed. In particular, the behaviour of the friction coefficient on the convex and concave walls is studied as a function of the curvature, and a comparison with the few existent data is reported.

6.1 Background

The basic geometry of a curved channel, where an azimuthal pressure gradient drives the flow in the gap between an outer concave and an inner convex wall, is pivotal both as a paradigmatic case for the study of flow on streamwise curved surface and for its central role in engineering applications. Since the fundamental study of Dean [31], this flow, which is today commonly referred to as Dean flow [102], has been the subject of several analyses which aimed at a general understanding of the underlying physics of turbulence in presence of streamwise curvature.

As pointed out by Bradshaw [16], curvature effects on the average properties of a flow in turbulent regime are heavily nonlinear: in particular, the effects of the extra rate of strain imposed by streamwise curvature turns out to be one order of magnitude larger than would be inferred from an analysis of the equations of motion.

As a consequence, massive differences exist between the turbulent straight channel flow and the curved channel flow. Experimental [44] as well as numerical [85] analyses of the Dean flow have been carried out in the past to elucidate how streamwise curvature affects the transition to turbulence and eventually the turbulence itself; however, some fundamental aspects still remain obscure.

It is generally recognized [102] that, above a critical value of the Reynolds number, the laminar solution becomes centrifugally unstable, and counter-rotating structures, known as Dean vortices (DV), appear close to the concave surface. Though the feature of DV resembles the TV discussed in the previous chapters, the pattern of transition experienced by the Dean flow is by far less rich than that of the TCF (see [112]). The first stage of the transition can be reached by one of these mechanisms: (1) by triggering an instability that leads to the merging or the splitting of the DV (see [13], [47]); (2) by the deformation of the the streamwise vortices in azimuthal direction with the successive appearance of two kind of travelling waves, undulating vortices and twisting vortices (see [44], [68]).

When the turbulent regime is reached, some observers [52] have discovered that large-scale structures similar to DV are present, in a clear parallel with what has been observed in TCF [63]; however both typical dimension and spatial extension of TDV and TTV are different, having the former smaller axial wavelength and radial extension, and a less steady position in space. On the other hand, others (see [96] for a complete review on the subject) believe that TDV do not exist at all. As a general statement, we emphasize that the portrayed pattern of transition depends heavily on the degree of curvature of the channel as well as on end-effects.

The numerical difficulties related to the cylindrical geometry have prevented a massive use of direct numerical simulations for the study of the Dean flow [84]. The large number of results obtained by the scientific community through the DNS of turbulent straight channels, including the analysis of turbulence statistics [59] as well as the discovery of a of self-sustained mechanism for the wall turbulence [56] and the implementation of various control strategies [73], appears as a mirage for the DF community.

In fact, in spite of its above-mentioned importance, only few direct numerical simulations at the Dean flow exist. Moser & Moin [85] carried out one simulation for a small curvature DF at Reynolds number of 2900, based on centreline mean velocity and channel half-width. Nagata & Kasagi [91] recently considered a range of curvatures, by simulating a flow with constant friction velocity, which is not probably at such an high Reynolds number to show a fully developed turbulence, and examined how the friction coefficient depends on the curvature. Xu, Choi & Sung [124] considered a small-curvature channel, proposing a strategy for turbulence control.

The results presented in literature seem to disagree on some aspects: for example Moser & Moin [85] sustain that the value of the curvature should have small effect on the turbulent intensities, while Nagata & Kasagi [91] show the opposite to be true. Moreover, sometimes they remain at a preliminary stage on other issues which we believe should deserve a deeper analysis.

For example, the behaviour of the friction coefficient as a function of the curvature is found in [91] to be monotonic for the concave wall, but non-monotonic for the convex wall. Besides, the question of the existence of a logarithmic law for the streamwise velocity near both the walls does not seem to have received any profitable answer.

In this work, through direct numerical simulations of the Navier–Stokes equation for an incompressible fluid, we investigate the DF in turbulent regime at various degrees of curvature, adding some contributions on various aspects of the problem which are still considered as open question by the scientific community, and presenting details on turbulence statistics.

6.2 The numerical simulations

As already seen in chapter §1, in the Dean flow a streamwise pressure gradient drives a flow in a channel curved in the streamwise direction. The azimuthal pressure gradient $\partial p/\partial\theta$ is written with the concise notation P_θ. This flow admits (see eq. (1.2)) a laminar solution

$$w^l(r) = \frac{P_\theta}{2\nu}\left[r\log r + Ar + Br^{-1}\right],$$

where A and B depends on the geometry. By integrating the laminar solution along the radial direction, the mass flow per unit of axial length Q can be expressed as a function of the pressure gradient:

$$Q = \frac{P_\theta}{2\nu}\left[\frac{(\log\mathcal{R}_o - \log\mathcal{R}_i)^2}{1/\mathcal{R}_i^2 - 1/\mathcal{R}_o^2} - \frac{\mathcal{R}_o^2 - \mathcal{R}_i^2}{4}\right]. \tag{6.1}$$

From eqs (1.2) and (6.1), and defining a bulk velocity U_b as $Q/(2\delta)$, the laminar solution can be recasted in terms of U_b

$$w^l_\theta(r) = \frac{U_b}{2\delta}\left[r\log r + Ar + Br^{-1}\right]\left(\frac{(log\mathcal{R}_o - log\mathcal{R}_i)^2}{1/\mathcal{R}_i^2 - 1/\mathcal{R}_o^2} - \frac{\mathcal{R}_o^2 - \mathcal{R}_i^2}{4}\right)^{-1}. \tag{6.2}$$

In this chapter we consider as characteristic dimensions the channel half-width δ and the bulk velocity U_b; the curvature degree is defined as $\gamma = \delta/\mathcal{R}_c$, where $\mathcal{R}_c$ is the radius at the centreline.
The numerical method used has been presented in chapter §2.

By considering a periodic box we are aware that the experimental condition of a flow in curved duct cannot be properly simulated, since the effects of the lateral walls are removed, and periodic boundary conditions in both the homogeneous directions are employed.

We can confidently get rid of the end-effects, by comparing our results with those obtained in the central region of an experimental domain with a large aspect ratio (the ratio between the spanwise dimension and the channel width), and by making sure that the streamwise L_θ and spanwise extension L_z are large enough for all the turbulent (small- and large-scale) structures to develop.

Another problem is related to the high computational cost of a DNS. In fact, the required computational effort forces us to consider the shorter computational domain which is not lacking the basic aspects of the real turbulent flow. So, the choice of the proper streamwise L_θ and spanwise extension L_z is not trivial. In fact, by choosing L_θ we should guarantee that this distance is long enough for the streamwise-elongated turbulent structures to be uncorrelated, and the selection of L_z forces the wider structure of the flow to be shorter than L_z, and moreover we have to guarantee that L_z is large enough for the small structures to be uncorrelated. Besides, if we want to study the phenomenon of merging and splitting of DV, and more generally if we are studying the effect of a mutual interaction between couples of vortices which are far the one from the other, we should consider computational domain comprehending several pairs of vortices.

For all the above mentioned considerations, we have decided to use a domain with an axial dimension $L_z = 4/3\pi\delta$ and a streamwise dimension $L_\theta = 8\pi\delta$. To guarantee the adequate spatial resolution, 516×128 modes are used in the streamwise and spanwise direction respectively; in radial direction 129 points are used on a non-uniform mesh. The dimensions of the computational stencil, scaled with the inner layer quantities (u_τ, ν), has a spanwise width of $4.3 - 7$ wall units, a streamwise extension of $4.8 - 13$, where the two values take into account the lowest and highest local R_τ at the inner and outer walls of all the simulations. The non-uniform mesh used for the radial direction produces a minimum distance, between consecutive points close to the walls, of $0.55 - 0.89$ wall units and a maximum distance, in the centre of the channel, of 5.4 wall units. The time advancement is $\Delta t = 0.015\delta/U_b$, corresponding to $\Delta t^+ \approx 0.10 - 0.24$.

The Reynolds number is defined as $Re = U_b\delta/\nu$, and the chosen value is $Re = 2800$ (see [59]). Four different curvatures have been considered, covering the range between large to small curvature and are reported in tab. 6.1. As initial field for the case with minimum curvature γ_1 we have used a fully developed turbulent flow in a straight channel with a 128×128 modes and 129 radial points, which has been spectrally interpolated to obtain all the required modes; all the other simulations have been started from a γ_1 fully developed turbulent flow. The typical time required for a simulation is of the order of a week on a cluster of 10 SMP Personal Computer, each equipped

case	η	γ	$R_{\tau,i}$	$R_{\tau,o}$	R_τ	$C_{f,i}10^{-3}$	$C_{f,o}10^{-3}$
1	0.975	0.0126	162.3	189.6	176.8	6.721	9.166
2	0.875	0.066	135.8	200.5	175.8	4.705	10.25
3	0.778	0.125	132.7	208.0	184.7	4.495	11.04
4	0.6	0.25	132.6	213.6	201.5	4.487	11.64

Table 6.1: Comparison between Reynolds number, R_τ, and local friction coefficients, C_f, for various curvature, expressed as η and γ.

with a 2 Intel Xeon 2.66 GHz CPU, and 512MB of 266 MHz SDRAM. The simulation have been run for a total time of $800\delta/U_b$ units and the first $200\delta/U_b$ have been discarded for the computation of the statistics, which have been computed on 30 fields stored every $20\delta/U_b$.

6.3 Curvature effects on wall-shear stress

The imposed pressure gradient drives the flow between the curved walls in such a way that the velocity profile is no more symmetric about the centreline of the channel, contrarily to straight channel flow. Besides, the mean azimuthal velocity profile has different slopes over the inner and outer wall. A suitable parameter for the description of the wall turbulence, related to the shear stress, is the local Reynolds number,

$$R_{\tau,p} = \frac{u_{\tau,p}\delta}{\nu} = \sqrt{\frac{\overline{\tau}_p}{\rho}}\frac{\delta}{\nu},$$

where $u_{\tau,p}$ are the local friction velocity, and $\overline{\tau}_p$ represents the shear stress at the inner ($p = i$) and outer ($p = o$) wall.

From the balance of the mean forces in azimuthal direction [124] a global friction velocity

$$u_\tau = \sqrt{\frac{P_\theta}{\rho \mathcal{R}_c}} = \sqrt{\frac{(1-\gamma)^2\overline{\tau}_i + (1+\gamma)^2\overline{\tau}_o}{2\rho}} \tag{6.3}$$

can be defined as well.

In tab. 6.1 a comparison of the cases at various curvature is presented in terms of different mean flow parameters. As the curvature increases, from the top to the bottom, the asymmetry of the flow grows too, in fact the $R_{\tau,i}$ decreases and $R_{\tau,o}$ increases.

Figure 6.1 reports the behaviour of the local friction Reynolds number versus curvature: as the curvature grows, at the inner cylinder the Reynolds

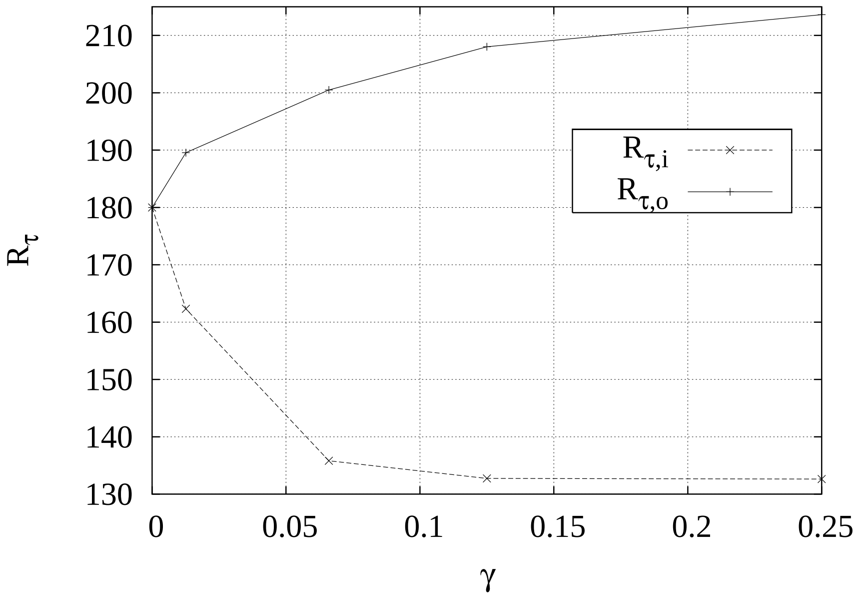

Figure 6.1: Behaviour of the local R_τ at the inner and outer wall as a function of the curvature parameter. The dashed curve is the $R_{\tau,i}$ and the continuous line the $R_{\tau,o}$.

number decreases and eventually it seems to reach a plateau, while at the outer wall the local Reynolds number increases and perhaps reaches a plateau for curvature slightly higher than those considered here.

By following the definition of the friction velocity is easy to see that the local friction coefficient C_f can be written as

$$C_{f,p} = \frac{\overline{\tau}_p}{\rho U_b^2/2} = 2\left(\frac{R_{\tau,p}}{Re}\right)^2 .$$

A monotonic behaviour of C_f over the upper wall can be observed in tab. 6.1, and confirms qualitatively the results presented by [91], while the behaviour at the inner wall shows a significant difference with the above mentioned article, where C_f is reported as non-monotonic.

In fig. 6.2 the ratio between the local friction coefficient for a fixed γ and the friction coefficient $C_{f0} = 8.18 \cdot 10^{-3}$ for the plane channel at the same $Re = 2800$ (see [59]) is plotted and compared with the results obtained by [91], who have conducted simulations at $R_\tau = 150$. At low curvature the results agree, however as γ increases both quantitative and qualitative differences appear. This difference is a consequence of the diverse hypotheses under which the two simulation have been carried out. In [91] a constant R_τ

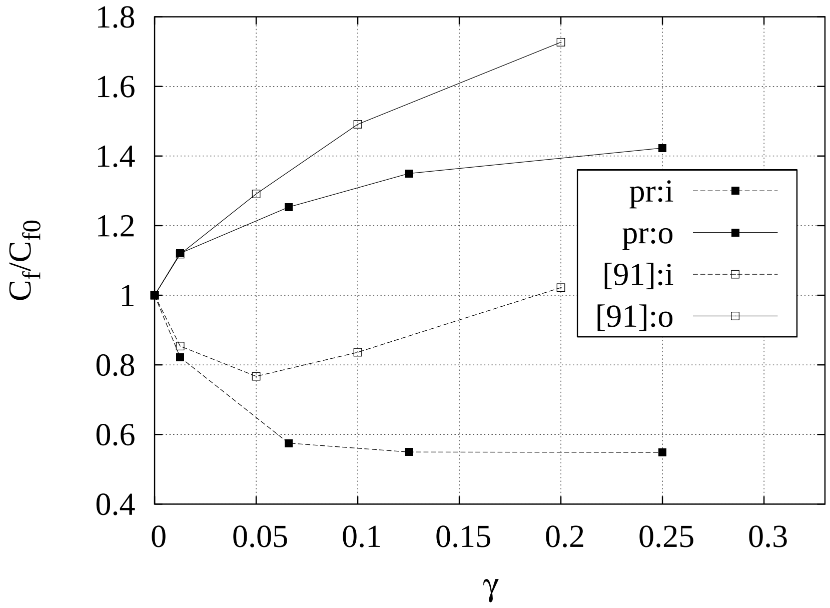

Figure 6.2: Behaviour of the relative friction coefficient C_f to C_{f0} at the inner (dashed line) and outer wall (continuous line) as a function of the curvature parameter. Comparison between [91] (□) and the present simulations (■).

was assumed, however this (see eq. (6.3)) does not guarantee that a significant physical parameter such as the pressure gradient or the mass flow, as in our simulation, is held constant for different curvature: we can thus conclude that on both walls the behaviour of the friction coefficients is monotonic with γ.

6.4 Low-order turbulence statistics

The slopes at the wall are, obviously, just a small part of the story. In fact, looking at the average profile of azimuthal velocity, fig. 6.4, we can see how large is the asymmetry between the upper ($r > \mathcal{R}_c$) and lower ($r < \mathcal{R}_c$) part of the channel, and how this asymmetry increases with γ. In order to compare cases with different inner radii we have rescaled the radial coordinate as $\Delta r = r - \mathcal{R}_i$. It is important to note that the maximum of the streamwise velocity, which for the laminar case lies in the inner part of the channel, exhibits here an unexpected non-monotonic behaviour as shown in fig. 6.3. For small curvatures it shifts towards the outer part of the channel, and only when γ increases further it eventually moves towards the inner part of the channel. This behaviour can probably be observed in fig. 4 by [91], however it is not noticed nor discussed.

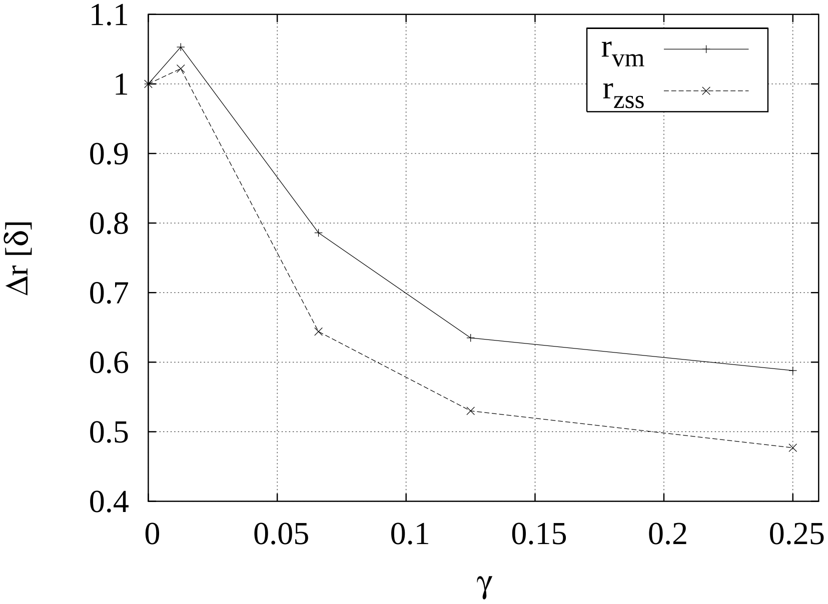

Figure 6.3: Radial position of the maximum of mean azimuthal velocity $\overline{w}$ (continuous line) and zero shear stress point (dashed line) as a function of γ.

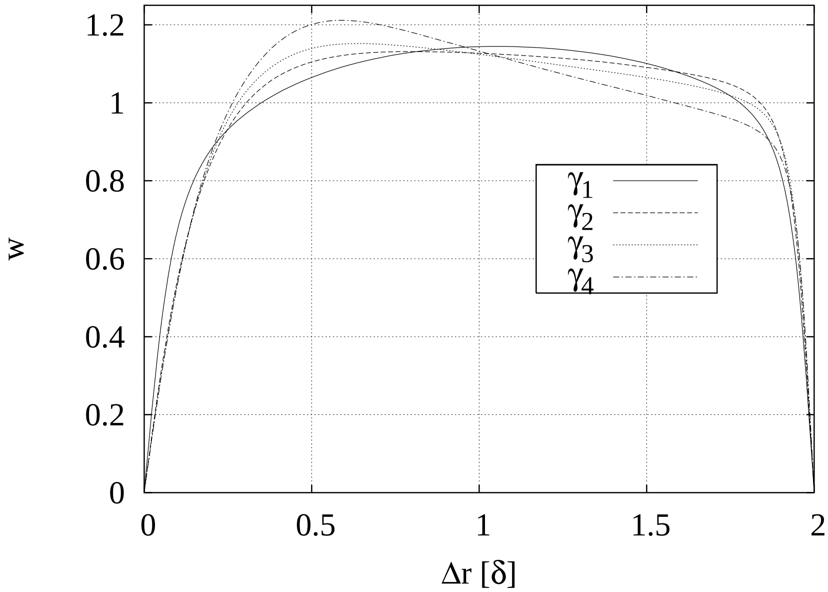

Figure 6.4: Average azimuthal velocity $\overline{w}$ as a function of the radial position, for various γ: γ_1 is the continuous line, γ_2 is the dashed line, γ_3 is the dotted line, and γ_4 is the dashed-dotted line.

case	η	γ	k	k^{-1}	C
1	0.975	0.0126	0.58	1.71	8.52
2	0.875	0.066	1.08	0.92	10.98
3	0.778	0.125	1.08	0.92	10.00
4	0.6	0.25	0.97	1.03	8.44

Table 6.2: Parameters of the logarithmic law $k^{-1}\log(\Delta r^+) + C$ for various curvature, expressed as η and γ.

We now come to discuss the issue of the existence, for the average azimuthal velocity $\overline{w}^+$, of a logarithmic law of the form $k^{-1}\log(\Delta r^+) + C$. As reported in [96] various laws have been proposed for small curvature: (1) $k = 0.42, C = 5.45$ from the experimental data of Patel; (2) $k = 0.4, C = 5.5$ form the DNS data by Moser & Moin; and (3) $k = 0.41, C = 4.9$ from boundary layer experiments by Bandyopadhyay. However all of them fit the velocity profile for just a small range of Δr^+ and for the only concave wall.

In fig. 6.5 we report, in logarithmic scale and for the small-curvature case γ_1, the average azimuthal velocity non-dimensionalized with the proper local friction velocity as a function of Δr^+. In this graph a logarithmic law should appear as a straight line for a conspicuous range of Δr^+ in the region $30 < \Delta r^+ < 100$ (e.g. [59] for the plane channel flow). The values $k = 0.4, C = 5.5$ proposed in literature [85] fit reasonably well in the concave region (outer wall), whereas $C = 7.5$ has been used to fit the velocity profile in the convex part (inner wall) of the channel. We note that a viscous sublayer definitely exists for $\Delta r^+ < 5$, where the azimuthal velocity scale with the radial dimension: $\overline{w}^+ = \Delta r^+$. These results are in good agreement with those presented by [85] for the same value of the curvature parameter, but do not allow to drawn conclusion about the existence of the law of the wall.

In figs 6.6 and 6.7 we plot the azimuthal velocity $\overline{w}^+$ versus Δr^+ for various values of curvature. In the outer part of the channel, and especially for the higher curvature, a logarithmic law can be observed to exist (see fig. 6.8) but it depends heavily on the curvature and, in particular, an increase of the k parameter and a corresponding decrease of C occur, as shown in tab. 6.2; however in the mild curvature regime the k parameter keeps constant with γ. Moreover we notice that the logarithmic region shifts towards the wall as the curvature increases, and its extension expand as well.

No logarithmic law seems to be present for the inner wall. Our general conclusion on the existence of the logarithmic law is that for the concave wall it could exist with the (k, C) parameters depending on γ, while for the inner wall the existence of such a law seems less plausible.

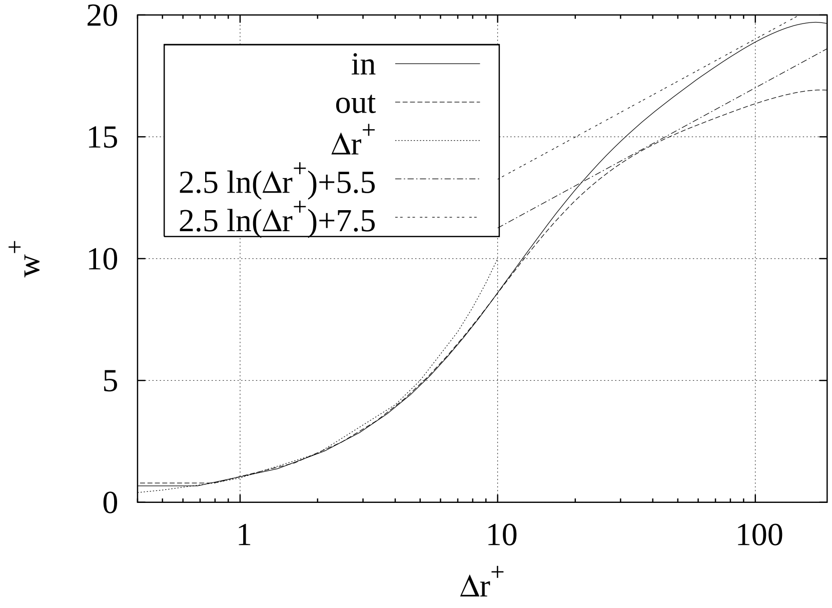

Figure 6.5: Average azimuthal velocity $\overline{w}^+(\Delta r^+)$ at the inner (continuous line) and outer (dashed line) walls, expressed in logarithmic scale for γ_1. The sublayer velocity law $w+ = \Delta r^+$ (dotted line) and the two logarithmic law $2.5\log(\Delta r^+)+5.5$ (dashed-dotted line) and $2.5\log(\Delta r^+)+7.5$ (double-dashed line) are also plotted.

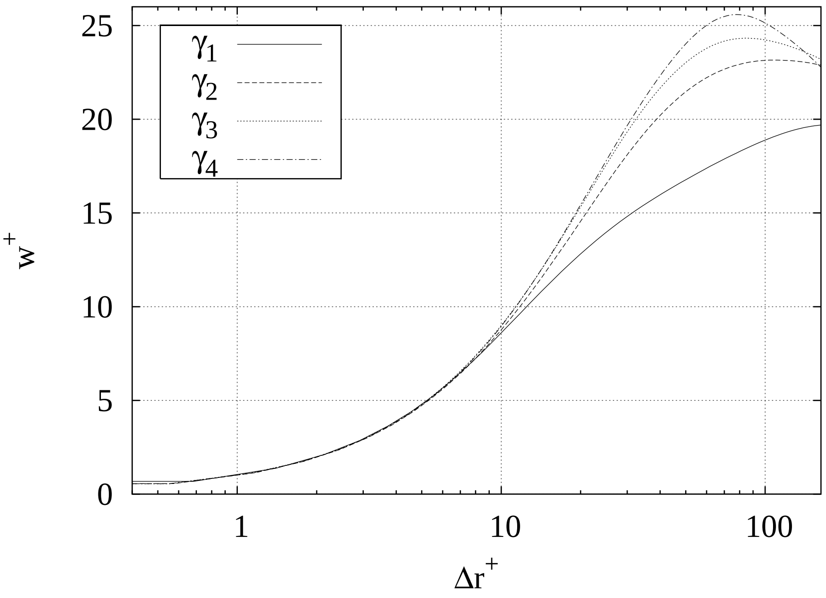

Figure 6.6: Average azimuthal velocity $\overline{w}^+(\Delta r^+)$ at the inner wall expressed in logarithmic scale, at various γ: γ_1 is the continuous line, γ_2 is the dashed line, γ_3 is the dotted line, and γ_4 is the dashed-dotted line.

As pointed out by Townsend [116], shear flows in curved geometry manifest regions of constant circulation, in which the streamwise velocity has constant angular momentum. In fig. 6.9 we have plotted the product $r\overline{w}$ as a function of Δr for various γ, non-dimensionalized with the maximum of $r\overline{w}$ for each γ. We note that in the case of large and mild curvature a wide region of constant angular momentum exists in the outer part of the channel, while for small curvature this region is very thin. This fact confirms, for the first time in a numerical simulation, the observations made in various experiments (see [41]) which, however, were conducted at Re ten to twenty times larger than ours. Being this region of almost-constant angular momentum close to the outer wall, the shear layer near the outer wall becomes thinner as curvature grows. On the contrary, at the inner wall a thicker layer is formed.

Starting from the analogy between the effect of the buoyancy and that of rotation, Bradshaw [16] derived the rotational counterpart of the Richardson equivalent flux number

$$R_f = \frac{2\overline{w}r^{-1}}{r\partial(\overline{w}r^{-1})/\partial r}, \tag{6.4}$$

which represents the ratio between the streamwise and radial production term in the turbulent kinetic energy equation as shown in eq. (5.4). Besides, R_f

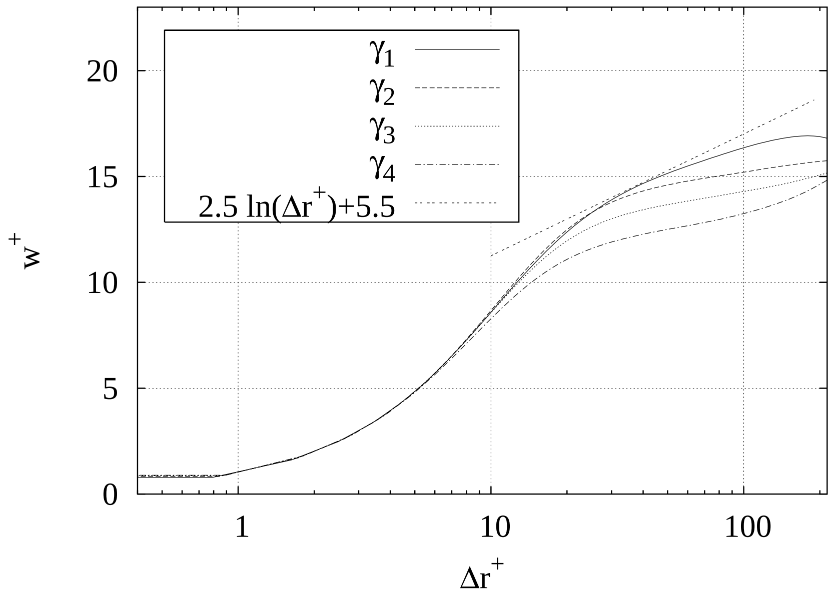

Figure 6.7: Average azimuthal velocity $\overline{w}^+(\Delta r^+)$ at the outer wall expressed in logarithmic scale, at various γ: γ_1 is the continuous line, γ_2 is the dashed line, γ_3 is the dotted line, and γ_4 is the dashed-dotted line. The logarithmic law $2.5\log(\Delta r^+) + 5.5$ is plotted with a double-dashed line.

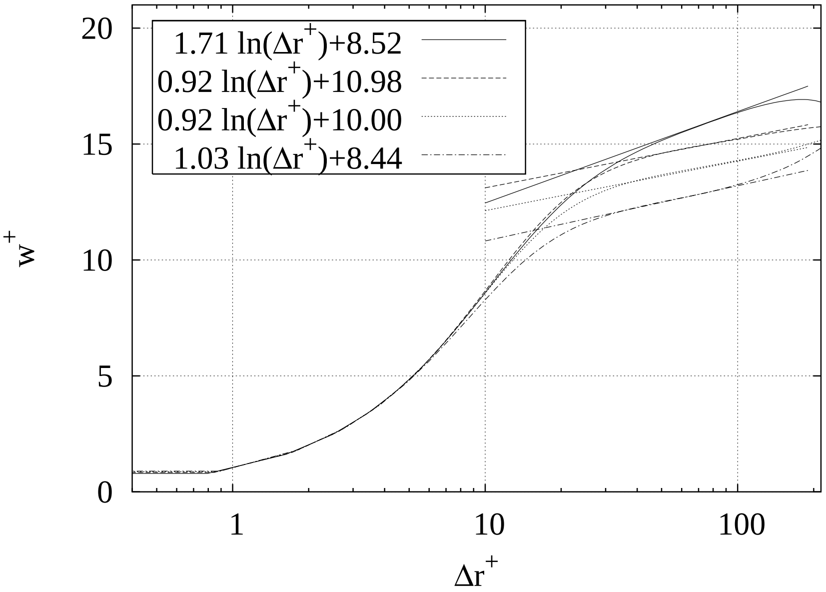

Figure 6.8: Logarithmic laws $k^{-1}\log(\Delta r^{+})+C$ and average azimuthal velocity $\overline{w}^{+}(\Delta r^{+})$ at the outer wall expressed in logarithmic scale, at various γ: γ_1 is the continuous line, γ_2 is the dashed line, γ_3 is the dotted line, and γ_4 is the dashed-dotted line.

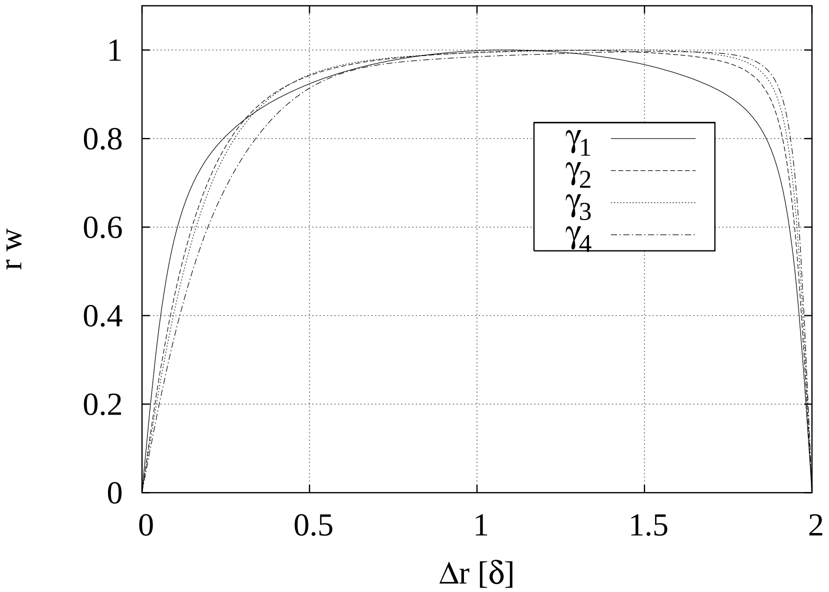

Figure 6.9: Angular momentum $r\overline{w}(\Delta r)$ for various γ: γ_1 is the continuous line, γ_2 is the dashed line, γ_3 is the dotted line, and γ_4 is the dashed-dotted line.

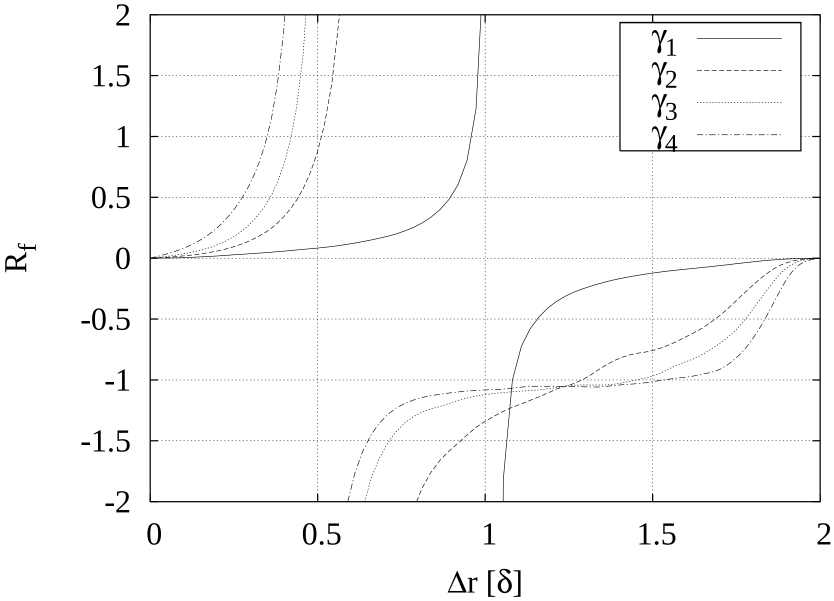

Figure 6.10: Richardson equivalent flux number $R_f(\Delta r)$ for various γ: γ_1 is the continuous line, γ_2 is the dashed line, γ_3 is the dotted line, and γ_4 is the dashed-dotted line.

can be interpreted as two times the ratio between the static pressure gradient in radial direction and the total pressure gradient in the radial direction, and it is used as a suitable weight for the dissipation lengths, being in so a useful parameter for RANS or LES modelling. If the angular momentum is constant with r, it is easy to show that $R_f = -1$. The Richardson equivalent flux parameter is represented, as a function of the radial position Δr, in fig. 6.10. It is possible to see that for a mild curvature there exists a region in the upper half of the channel where $R_f = -1$. Moreover when the denominator of eq. (6.4) goes to zero, R_f goes to infinity and this particular value of r is called the zero shear stress point, which depends heavily on γ [41] as can be observed in fig. 6.3.

The turbulence intensities for the three velocity components are plotted in figs 6.11 and 6.12 for the regions respectively close the inner and the outer wall and for the curvatures γ_1 and γ_2. We note that: (1) the r.m.s. are asymmetric, and this aspect is enhanced at higher curvatures; (2) the general behaviour of the r.m.s. near the convex wall does not change as γ grows, however a reduction of the θ component and a magnification of the r, z appear; (3) at the concave wall the behaviour of the r.m.s. changes for all the three components; (4) at least close to the wall, the θ component is predominant on z and r, the last being the smallest of the three; (5) in the

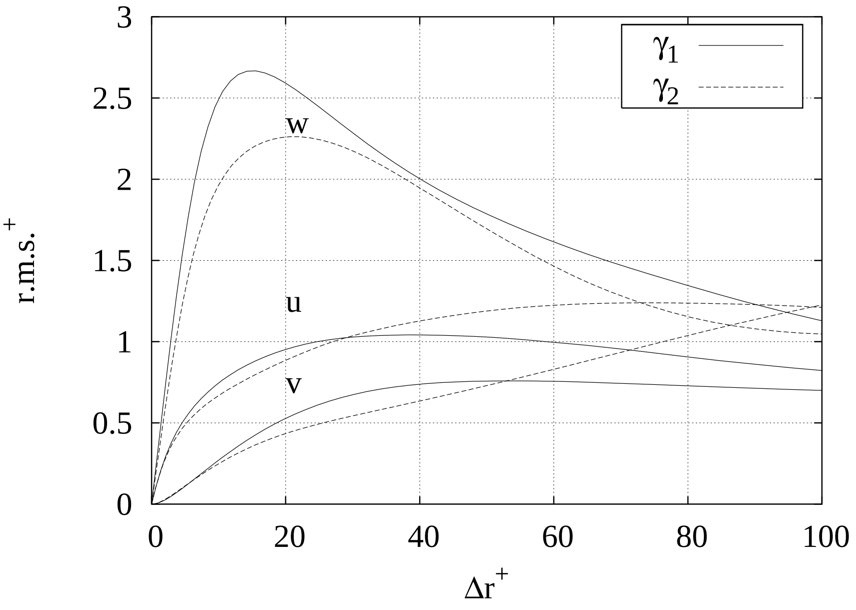

Figure 6.11: r.m.s. values of velocity components non-dimensionalized by local u_τ, at the inner wall for various γ: γ_1 is the continuous line, γ_2 is the dashed line.

concave region the maximum of r.m.s. for the θ component gets closer to the outer wall as γ increases, while for the convex region the movement of the maximum is towards the centre of the channel; (6) for mild curvature the z and r component became greater than θ at a distance from the wall of around 90 wall units.

As a general conclusion, and comparing the results with the simulation conducted for a straight channel [59] (plotted in fig. 6.13), we can state that the turbulence intensity for the streamwise component decreases, as γ grows, while the spanwise and radial components increase, and eventually overwhelm the azimuthal component. Our results confirm the qualitative observation by [91] that the curvature has a large effects on turbulence intensities.

The r.m.s. of the vorticity vector ω is plotted, non-dimensionalized with the local wall units, as a function of the radial position and for γ_1 and γ_2 curvature, in figs 6.14 and 6.15. We use the same scale to make a valuable comparison. At the concave wall the r.m.s. are bigger than at the convex wall for all the components of the vector. The curvature has large effects on both walls; in particular, the asymmetry increases as the curvature grows.

The high-order turbulence statistics, skewness S and flatness F factors, are derived for different curvature degrees. In figs 6.16 and 6.17 the skewness

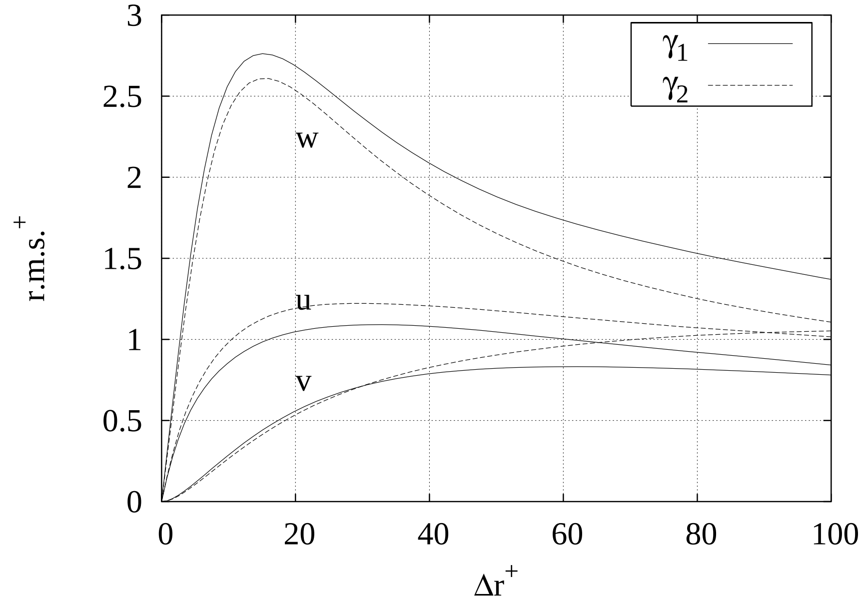

Figure 6.12: r.m.s. values of velocity components non-dimensionalized by local u_τ, at the outer wall for various γ: γ_1 is the continuous line, γ_2 is the dashed line.

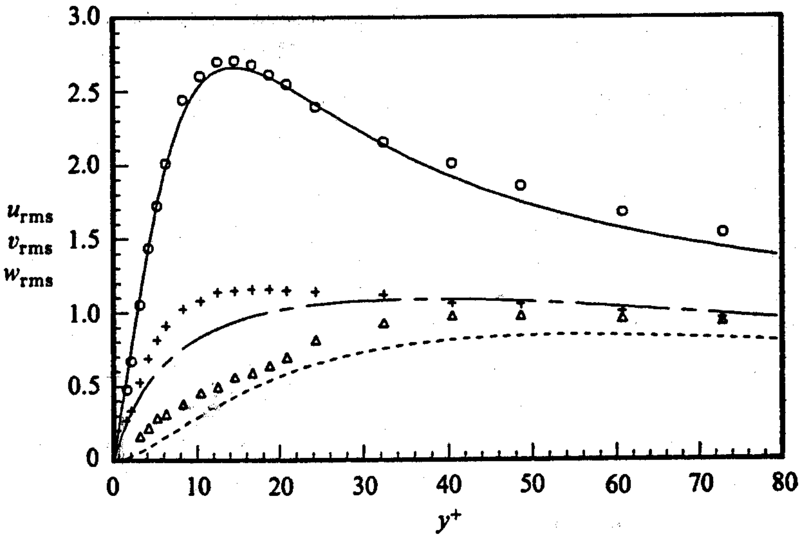

Figure 6.13: r.m.s. values of velocity components for a channel flow; the symbols refer to experimental results at $R_\tau = 180$ from [59]. The continuous line is u, the long-dashed line is v, and the small-dashed line is w; the symbols refer to experimental results.

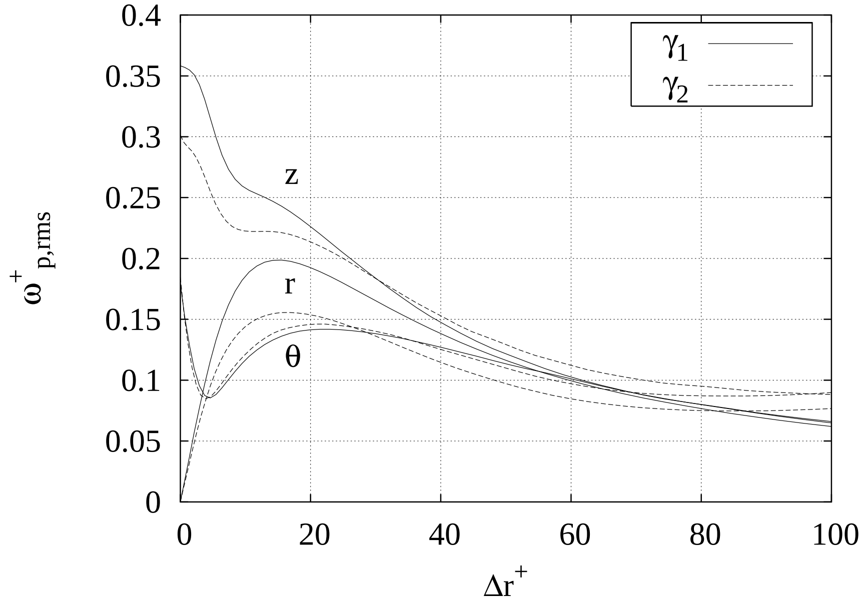

Figure 6.14: r.m.s. value of the vorticity $\overline{\omega}^+_{rms}$ non-dimensionalized by local u_τ, at the inner wall, at various γ: γ_1 is the continuous line, γ_2 is the dashed line.

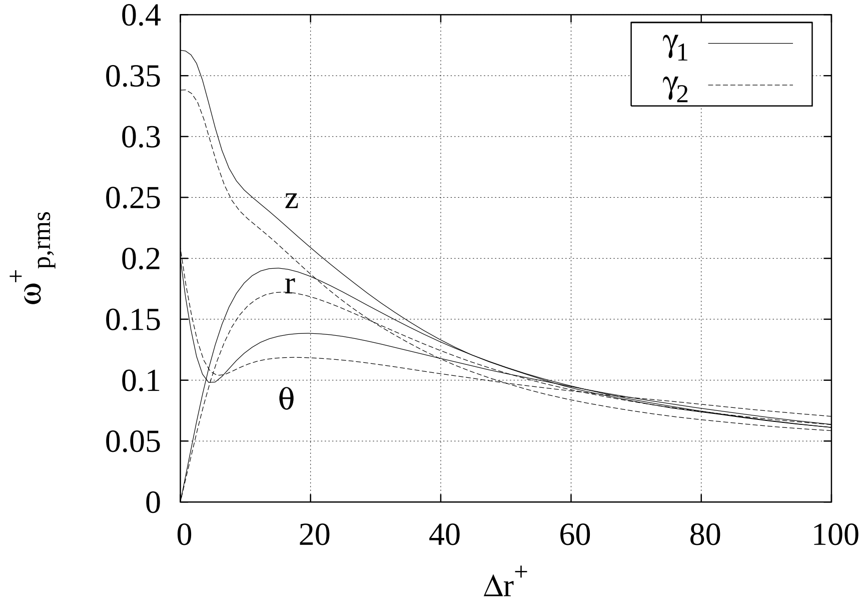

Figure 6.15: r.m.s. value of the vorticity $\overline{\omega}^+_{rms}$ non-dimensionalized by local u_τ, at the outer wall, at various γ: γ_1 is the continuous line, γ_2 is the dashed line.

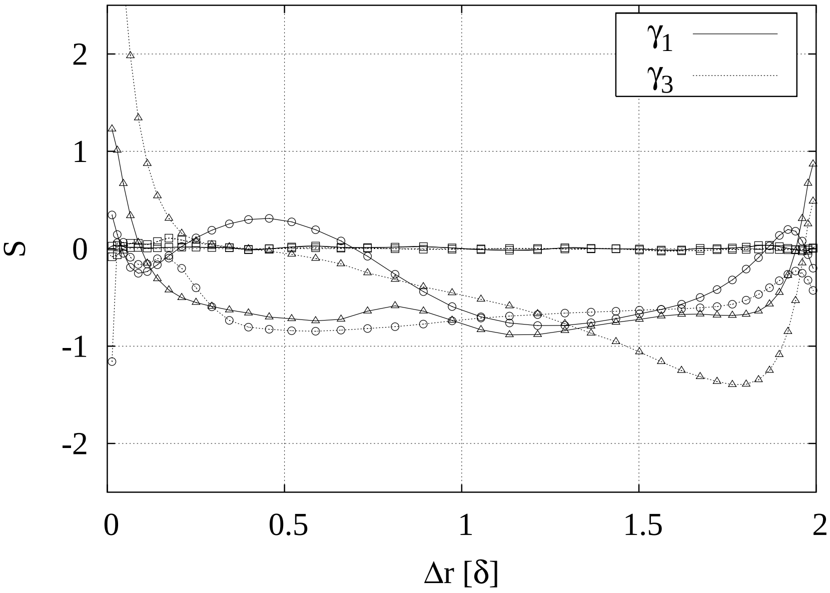

Figure 6.16: Skewness factor $S(r)$ of axial (◯), radial (□), and azimuthal (△) component of velocity vector for various γ: γ_1 is the continuous, and γ_3 is the dotted line.

and flatness are respectively plotted for γ_1 and γ_3. The results of our simulations show good agreement with the data available in literature for the γ_1 case, for both the skewness and the flatness factor. We can notice that as the curvature increases skewness and flatness becomes more asymmetric too.

6.5 Turbulence structures

The mono-dimensional spectra of velocity $\Phi_{\alpha,p}$ and $\Phi_{m,p}$, defined in eqs (5.6) and (5.7), are depicted respectively in figs 6.18 and 6.19 for the curvature γ_4 valuated at 59 wall units from the concave (outer) wall. We note that $\Phi_{\alpha,p}$ in fig. 6.18 is plotted with a linear scale. They both show no pile-up of energy associated with the small-scale, decaying vortices, so they have been correctly described in our simulation; moreover the axial spectrum $\Phi_{\alpha,p}$ shows for all its components a peak. Visualisations have shown that this peak is associated with elongated large-scale structures which can be possibly connected with the TDV; these structures are not steady as the previously seen TTV, and so are partially erased by the temporal and azimuthal mean process. We have not conducted further analyses on these structures.

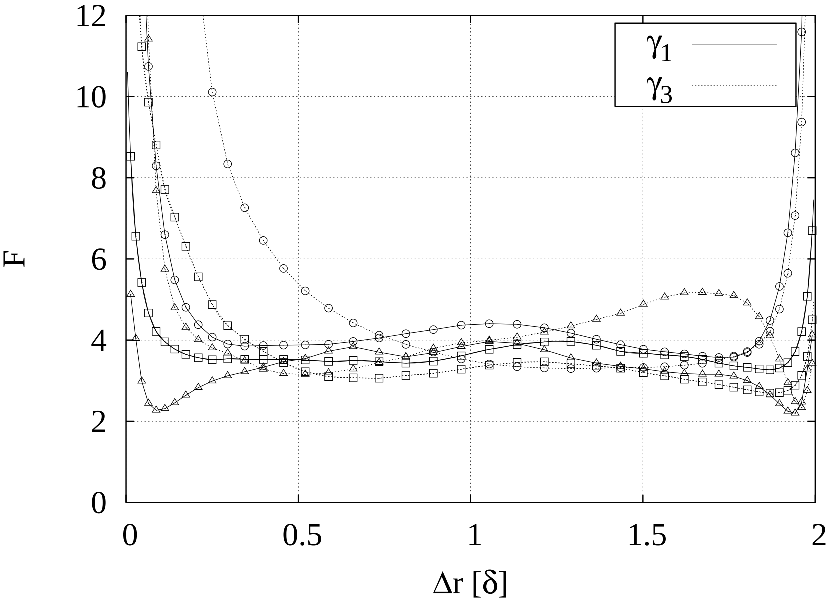

Figure 6.17: Flatness factor $F(r)$ of axial (◯), radial (□), and azimuthal (△) component of the velocity vector for various γ: γ_1 is the continuous, and γ_3 is the dotted line.

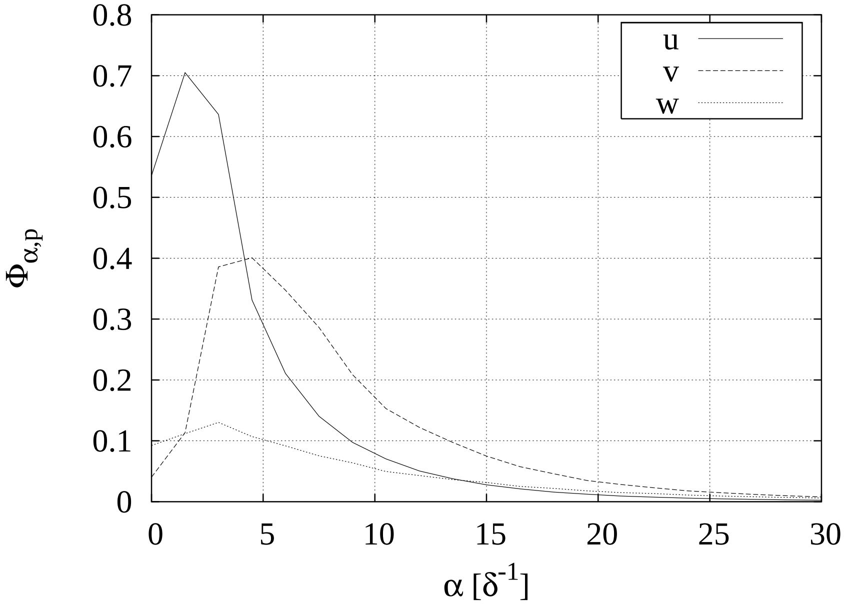

Figure 6.18: Mono-dimensional energy spectra $\Phi^+_{\alpha,p}(\alpha)$ of velocity at a distance $\Delta r^+ = 59$ from the concave wall at γ_4. The continuous line is u, the dashed line is v and the dotted line is w.

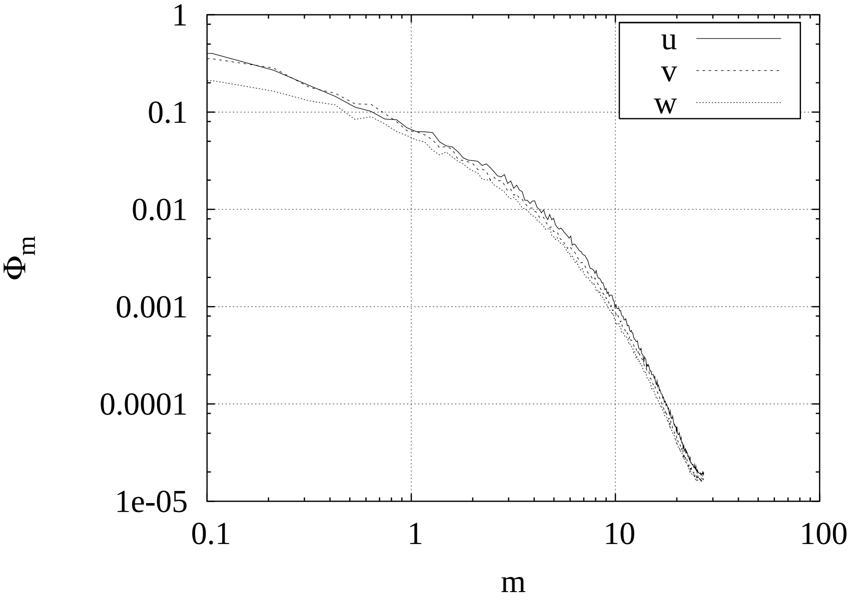

Figure 6.19: Mono-dimensional energy spectra $\Phi^+_{m,p}(m)$ of velocity at a distance $\Delta r^+ = 59$ from the concave wall at γ_4. The continuous line is u, the dashed line is v and the dotted line is w.

The mono-dimensional correlation coefficients $R_{z,p}$ and $R_{\theta,p}$ are depicted in figs 6.20-6.22 and 6.23-6.25, respectively. We have pictured the mono-dimensional correlation coefficient $R_{z,p}$ and $R_{\theta,p}$ for different values of the curvature from γ_1 to γ_4, at a distance from the outer wall which is between the value 4.3 (for small curvature) and 4.9 (for high curvature) wall units. The $R_{z,p}$ and $R_{\theta,p}$ of all the three component go to zero in half the axial period.

The points at which $R_{z,v}$ and $R_{z,w}$ reach their minimum are related, respectively, to the spanwise dimension Δz^+_v of the predominant, quasi-streamwise, near-wall, vortical structure, and to the half spacing Δz^+_s between the near-wall high- and low-velocity streaks. The zero-curvature data, reported in fig. 6.26, are taken from fig. 23 by [59]. Both the dimensions of the streaks and of the vortices are observed to grow with the curvature; the growth of the streaks as a function of γ is larger than that of the vortices.

An analysis of the fluctuating part of the shear at the inner $\tau'(z, \theta; \mathcal{R}_i, t)$ and outer $\tau'(z, \theta; \mathcal{R}_o, t)$ wall can produce a vivid image of the behaviour of the small-scale structures in the proximity of the walls. Preliminary, we have to observe that the Reynolds number at the outer wall is higher than that at the inner wall, so the outer wall is more turbulent.

In the case of small curvature γ_1, the shear stress at the inner and outer

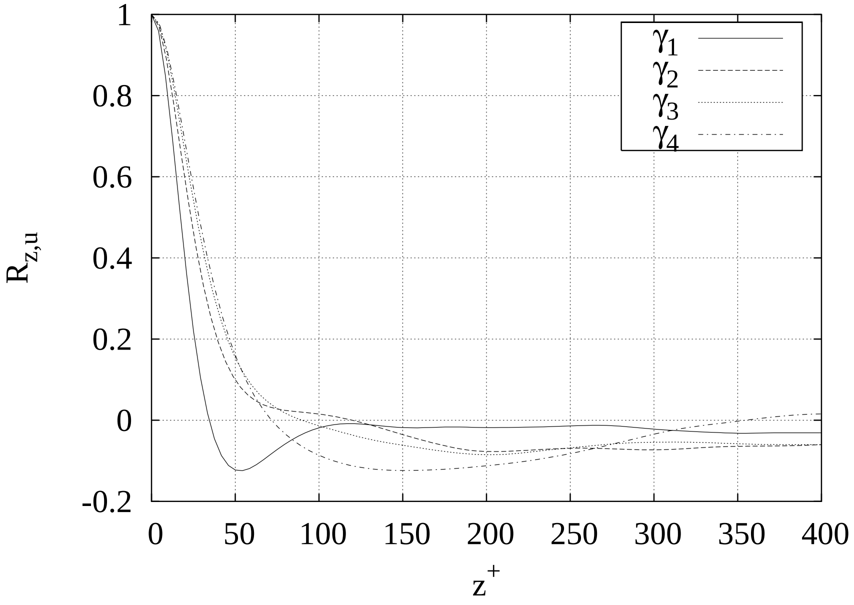

Figure 6.20: Mono-dimensional correlation coefficients $R_{z,u}(z)$ at the concave wall ($\Delta r^+ = 4.3-4.9$) for various γ: γ_1 is the continuous line, γ_2 is the dashed line, γ_3 is the dotted line, and γ_4 is the dashed-dotted line.

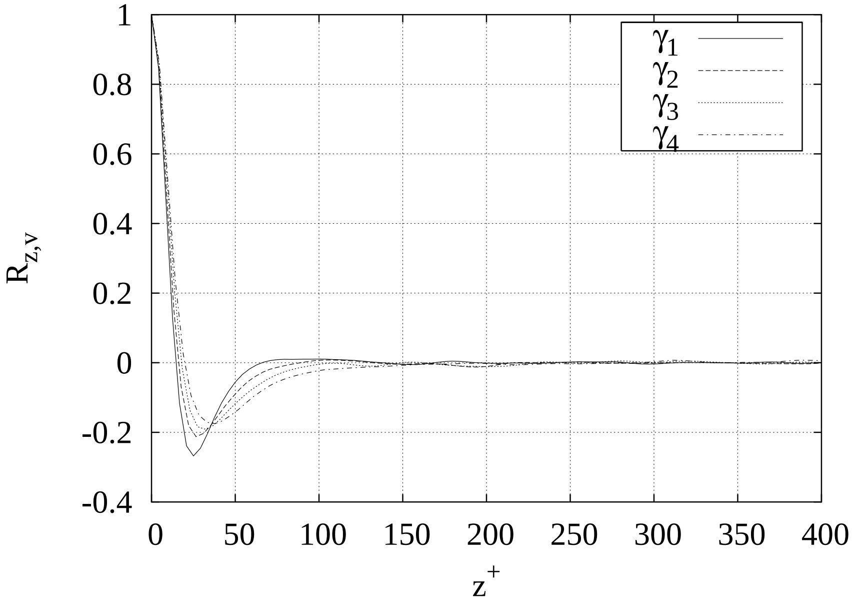

Figure 6.21: Mono-dimensional correlation coefficients $R_{z,v}(z)$ at the concave wall ($\Delta r^+ = 4.3 - 4.9$) for γ_1 is the continuous line, γ_2 is the dashed line, γ_3 is the dotted line, and γ_4 is the dashed-dotted line.

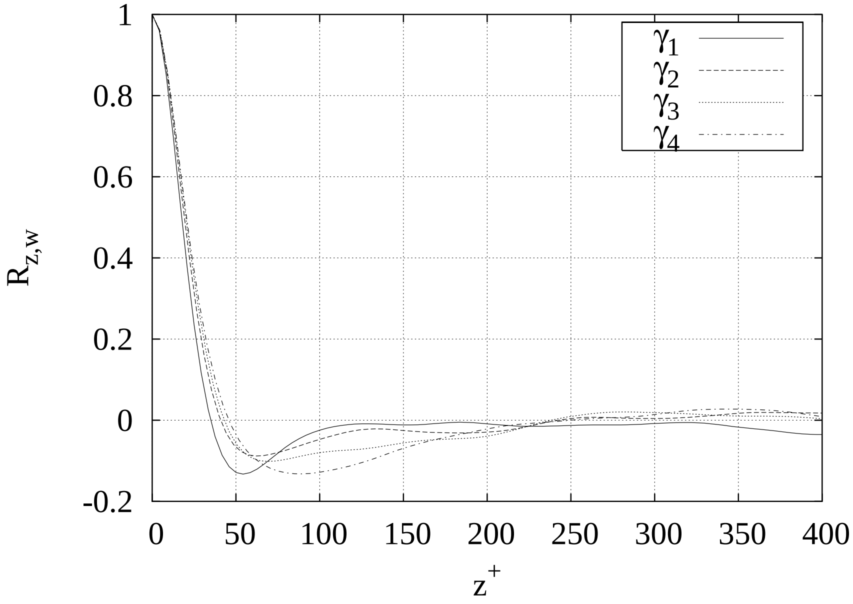

Figure 6.22: Mono-dimensional correlation coefficients $R_{z,w}(z)$ at the concave wall ($\Delta r^+ = 4.3 - 4.9$) for γ_1 is the continuous line, γ_2 is the dashed line, γ_3 is the dotted line, and γ_4 is the dashed-dotted line.

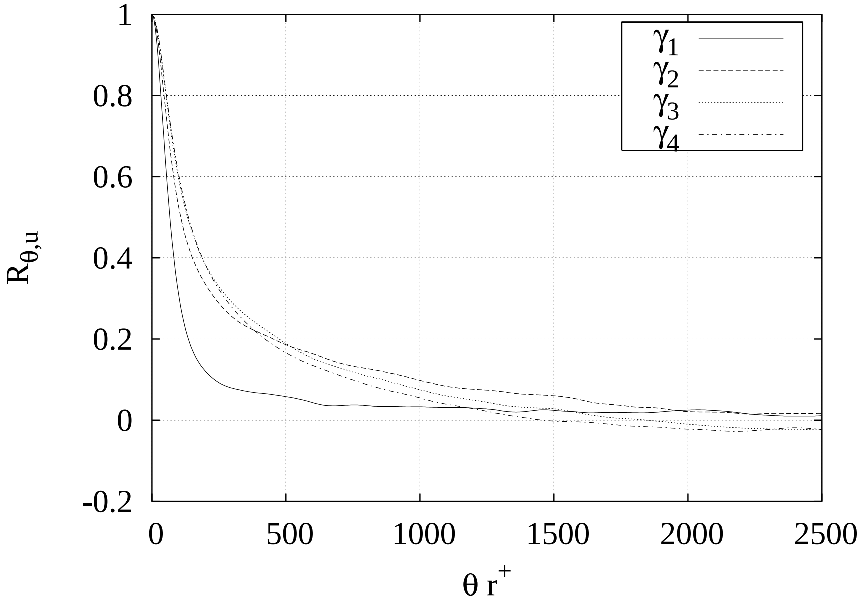

Figure 6.23: Mono-dimensional correlation coefficients $R_{\theta,u}(\theta r)$ at the concave wall ($\Delta r^+ = 4.3 - 4.9$) for γ_1 is the continuous line, γ_2 is the dashed line, γ_3 is the dotted line, and γ_4 is the dashed-dotted line.

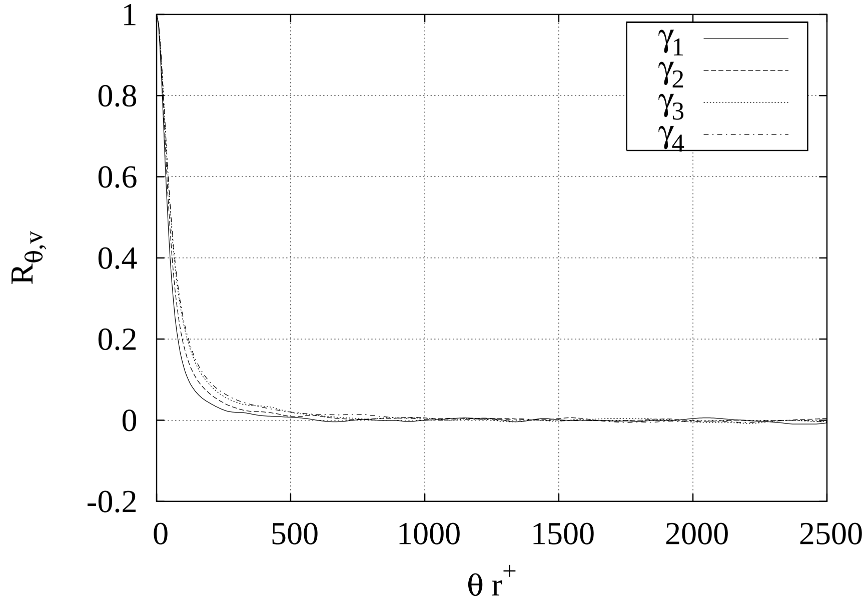

Figure 6.24: Mono-dimensional correlation coefficients $R_{\theta,v}(\theta r)$ at the concave wall ($\Delta r^+ = 4.3 - 4.9$) for γ_1 is the continuous line, γ_2 is the dashed line, γ_3 is the dotted line, and γ_4 is the dashed-dotted line.

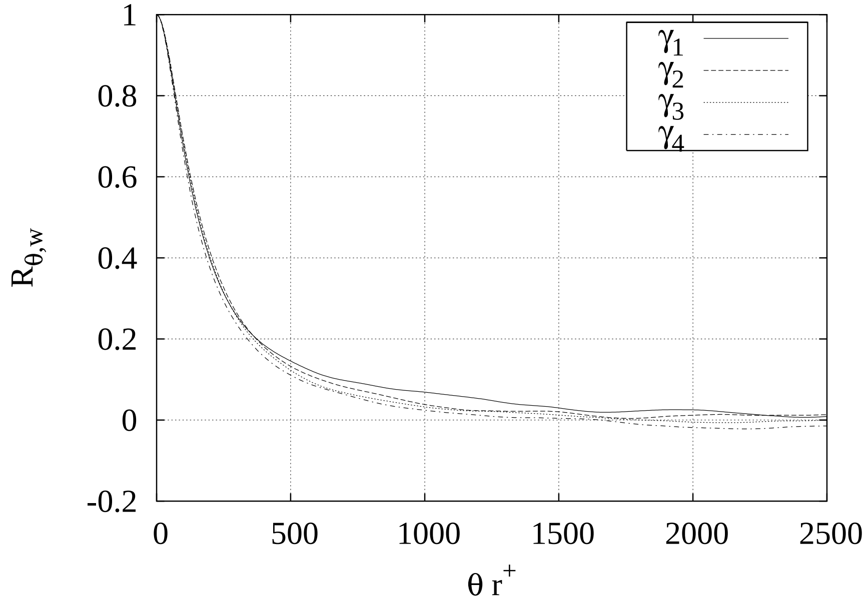

Figure 6.25: Mono-dimensional correlation coefficients $R_{\theta,w}(\theta r)$ at the concave wall ($\Delta r^+ = 4.3 - 4.9$) for γ_1 is the continuous line, γ_2 is the dashed line, γ_3 is the dotted line, and γ_4 is the dashed-dotted line.

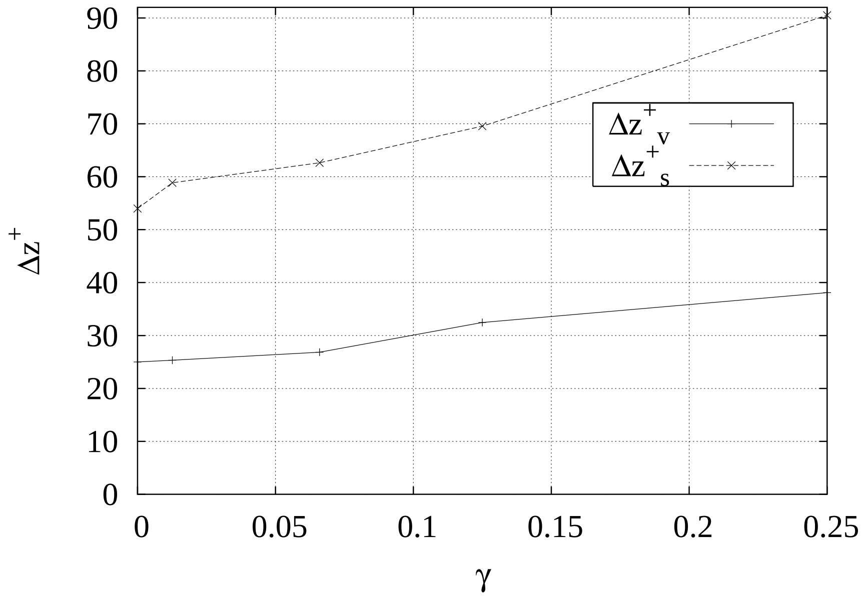

Figure 6.26: Dimension of the turbulent wall structures: streamwise vortices Δz_v^+ (continuous line) and streaks Δz_s^+ (dashed line) as a function of the curvature measured from the minima of the correlation functions.

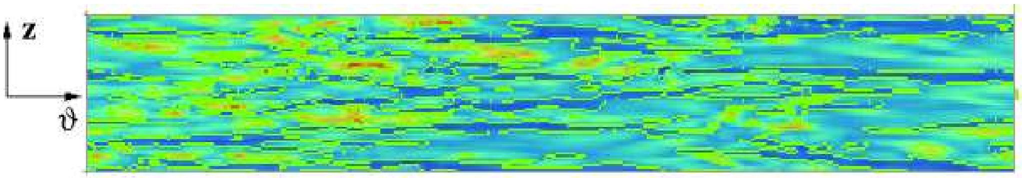

Figure 6.27: Instantaneous shear around the mean value $\tau'^{+}(z,\theta;\mathcal{R}_i,t)/\mu$ at the convex wall for an instantaneous flow field, at γ_1 ($\Delta\tau^+ = 0.2$, the positive values are red-coloured, the negative blue-coloured).

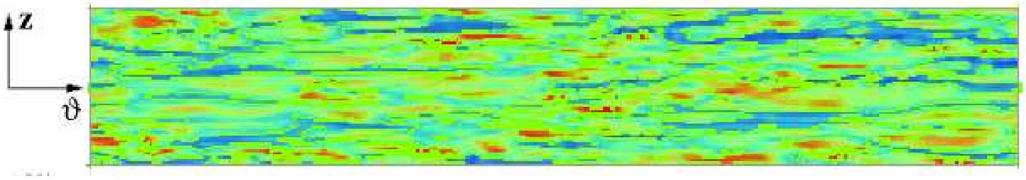

Figure 6.28: Instantaneous shear around the mean value $\tau'^{+}(z,\theta;\mathcal{R}_o,t)/\mu$ at the concave wall, for an instantaneous flow field, at γ_1 ($\Delta\tau^+ = 0.2$, the positive values are red-coloured, the negative blue-coloured).

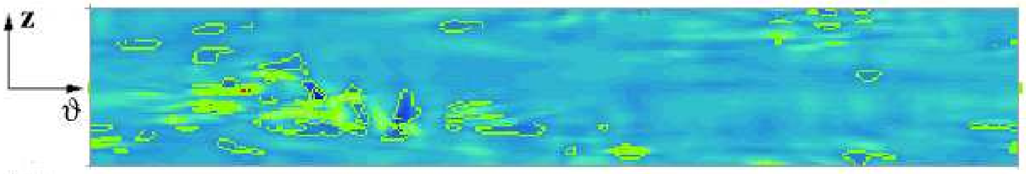

Figure 6.29: Instantaneous shear around the mean value $\tau'^{+}(z,\theta;\mathcal{R}_i,t)/\mu$ at the convex wall for an instantaneous flow field, at γ_3 ($\Delta\tau^{+}=0.2$, the positive values are red-coloured, the negative blue-coloured).

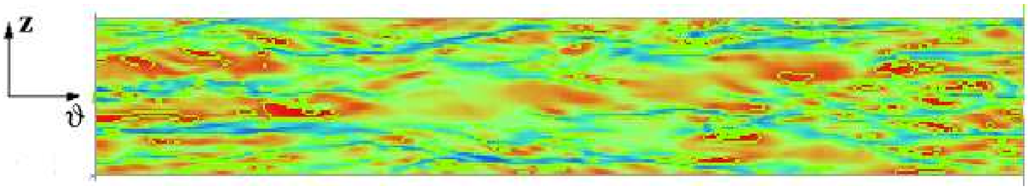

Figure 6.30: Instantaneous shear around the mean value $\tau'^{+}(z,\theta;\mathcal{R}_o,t)/\mu$ at the concave wall, for an instantaneous flow field, at γ_3 ($\Delta\tau^{+}=0.2$, the positive values are red-coloured, the negative blue-coloured).

wall, respectively figs 6.27 and 6.28, shows the presence of elongated (their streamwise extension is $400-900$ wall units) quasi-streamwise (with angle of $3-10°$) streaks of high (red) and low (blue) azimuthal velocity. As previously shown from the correlation coefficients (see fig. 6.26) in case of curvature γ_1, at a distance $\Delta r^{+}=4.3$ from the concave wall the minimum of $R_{z,w}$ suggests a streak spanwise half-spacing of around 50 wall units while the minimum of $R_{z,v}$ is in correspondence of around 30 wall units; both results show that these streaks are quite similar to the typical structures of the turbulent plane wall flows.

From the values of $R_{\tau,i}$ and $R_{\tau,o}$ in tab. 6.1 we have observed that an increase of γ has dramatic effects on the shear at the wall; the same conclusion can be inferred from an analysis of the shear at the inner (see fig. 6.29) and outer (see fig. 6.30) walls for a mild curvature (γ_3). By comparing these figures with their companions 6.27, 6.28 for the γ_1 curvature we can surmise that the streaks at the outer wall are longer than in the γ_1 case, which confirms the results in fig. 6.26; besides, at the inner wall the streaks do not appear anymore, which is a consequence of the low value of the local $R_{\tau,i}$.

6.6 Final remarks

Direct numerical simulations have been conducted in a curved channel flow at various degrees of curvature and for a Reynolds number which guarantees a fully developed turbulence. If we imagine to deform a straight channel flow by continuous bending of the streamwise axis, we recognize that the mean and instantaneous properties of the flow change dramatically with the increase of bending. In fact the profile of the streamwise velocity gains a strong asymmetry and the fluid is pumped, owing to centrifugal effects, from the inner to the outer wall. As the bending of the channel grows, the shear stress at the concave (outer) wall increases, while the opposite occurs for convex (inner) wall.

Moreover, as the curvature grows a large part of the channel in the external part of the gap is characterized by a nearly irrotational mean motion in which the angular momentum is almost constant with the radial position.

Both the wall layers are characterized by a viscous sublayer. For none of the considered curvature values the velocity profile near the convex wall shows a logarithmic law; on the other hand, the velocity profile over the outer wall does ineed show a logarithmic behaviour. The slope and the intercept of the fitting logarithmic line are strongly dependent on the amount of curvature.

As the curvature grows the turbulence intensity for the azimuthal components decreases, and its profile becomes more asymmetric. The radial and spanwise components exhibit increasing intensities which become higher than the streamwise component at large curvature. At the wall the flow presents elongated streaks and quasi-streamwise vortices which are similar to the widely recognized structures existent in the case of the straight channel.

CHAPTER 7

SUMMARY AND CONCLUSIONS

In this work various questions related to incompressible flows over solid surfaces with curvature in the streamwise direction have been considered. The issues of the pattern of transition to turbulence and the turbulent regime itself have been investigated. Two prototypical flows have been the subjects of our analysis: the Taylor-Couette flow, chosen for its physical importance, and the Dean flow, selected for its applicative relevance.

In the laminar regime both flows can be described by an exact solution of the incompressible Navier–Stokes equations. As a consequence of a centrifugal instability, above a critical value of the Reynolds number, these flows show the occurrence of elongated, streamwise-oriented, large-scale, vortical structures, superimposed on the laminar solution. These structures are known as Taylor vortices (TV) or Dean vortices (DV), in dependence of the flow geometry; they characterize also the transitional regime and, at least for the Taylor-Couette flow, the turbulent regime too. In fact, borne as azimuthally straight vortices, they deform as the Reynolds number grows, and gain azimuthal waviness. More complicate features appear as the Reynolds number increases further; once the turbulent regime is reached the large-scale structures eventually reappear, although immersed in a noisy background.

The effect of these structures on Taylor-Couette flow has not been satisfactory described in the literature, especially in the case of the fully turbulent regime, and together with the characterization of the turbulent Dean flow in terms of mean and instantaneous properties (i.e. friction coefficient, velocity profile, turbulence intensity, etc.) is the main motivations of the present work.

To this aim, we have performed both numerical simulations, in transitional and turbulent regime, and laboratory experiments. For the numerical simulations we have used a computer code designed for the parallel DNS of incompressible flows in cylindrical coordinates, a short description of which has been given in chapter §2, while the experiments have been conducted at the laboratories of the Manchester Centre for Nonlinear Dynamics, University of Manchester, with a newly designed Taylor-Couette apparatus .

The transitional regime has been studied in two different configurations of the Taylor-Couette flow, in order to assess the influence of temporal and spatial forcing, and to investigate a possible control strategy.

Direct numerical simulations have been used to study the effect of a temporal forcing on a large-gap Taylor-Couette system, as described in chapter §3. A wide range of Reynolds numbers and oscillation frequencies have been considered. We have concluded that the forcing delays the formation of the TV. Reversing and non-reversing TV flows have been recognized. A third regime, related to the oscillating Stokes' layer, has been moreover observed and described for the first time. The frequencies at which transition among these three regimes occurs have been found to depend on Reynolds number, and we have been able to describe this dependency in terms of a Landau's equation. As the Reynolds number increases further, for some particular frequencies, the axial period of the TV halves, and a sub-critical transition to a wavy regime takes place. The frequencies at which this last feature appears are approximately related to the typical period of the wavy TV in the zero-frequency limit, denoting a sort of quasi-resonant behaviour.

Once assessed that a time forcing influences the transition in TC flows, we have analysed, in chapter §4, whether the same is true for a spatial forcing, by investigating how the wavelength of a sinusoidally-shaped inner cylinder affects the characteristics of the TV.

The analysis has been carried out through a campaign of laboratory experiments, performed under the supervision of prof. Tom Mullin at the MCND during a six months stay. By slowly increasing the Reynolds number, we have been able to observe both steady and periodic flows which eventually lead to the turbulence regime. At the early stages of transition, the inner cylinder wavelength forces the appearance of a pair of counter-rotating vortices, similar to the classical TV, which develop in the region of the trough. They fill the whole gap but the crest region. As the Reynolds number increases, a pair of steady secondary vortices appears, made of counter-rotating structures which occupy the region of the crest and fill the outflow region of the primary vortices. At even higher Reynolds numbers, the secondary vortices experience an Höpf bifurcation and begin to oscillate; the amplitude of the oscillations grows with the Reynolds number, until they disappear, and a mono-cellular flow re-establish. However, these large vortices occupy the whole sinusoidal-wavelength. Successively, turbulence appears. We have also found that, above a certain threshold value of the Reynolds number, the uniqueness of the flow ceases to exist.

Our attention has then switched to the behaviour of the Taylor-Couette and Dean flows in the fully turbulent regime. We have carried out a number of direct numerical simulations for both flows to build a large database of several flow fields. They have been subsequently analysed, and particular attention has been dedicated to the issues of the presence of turbulent Taylor vortices (TTV), the behaviour of the friction coefficient versus curvature, and the presence of a logarithmic region for the streamwise velocity profile. In particular, the simulations of the Taylor-Couette flow in turbulent regime represent the first case of DNS at such an high value of Reynolds number, while the simulations of the Dean flow explore a wide range of curvature parameter in a fully turbulent flow for the first time.

In chapter §5 we have considered a small-gap Taylor-Couette flow in turbulent regime. The TTV have been observed, and their effects on low-order turbulence statistics have been analysed. The TTV produce, in the central part of the gap, a region of constant angular momentum; the velocity profile is asymmetric and the friction coefficient at the inner wall is higher than at the outer wall. The presence, if any, of a logarithmic layer for the average azimuthal velocity profile is confined to a very small region, but its very existence is subject to some degree of uncertainty. Another main effect of the TTV is the redistribution of turbulence intensity to the radial and axial velocity components. The contribution to the TTV-free turbulence statistics shows behaviours resembling, qualitatively, the plane turbulent Couette flow.

The Dean flow in turbulent regime has been considered in chapter §6 at various degrees of curvature. The friction coefficient changes dramatically as the curvature varies: on the convex wall it decreases while on the concave wall it increases. The azimuthal velocity profile becomes more and more asymmetric as the curvature increases. The point of maximum velocity moves from the centreline, but we have observed an unexpected range of relatively low curvatures, where this point approaches the outer wall, before crossing the centreline again and moving towards the inner wall, as commonly reported in literature. For none of the curvatures analysed, the mean velocity profile near the inner wall shows a logarithmic behaviour; however, the profile close to the outer wall shows indeed a logarithmic region, whose parameters are dependent on the curvature. The turbulence intensities are heavily asymmetric, too. At the wall, small-scale structures appear which have been recognised as the elongated streaks which characterize the flow in the case of the straight channel.

We conclude that large-scale structures represent the main elements of the flows on streamwise-curved surfaces, both in laminar and turbulent regime, in particular for TCF. A suitable temporal or spatial forcing is capable to affect the transition process efficiently. Once the turbulent regime is reached, the effect of large-scale structures on the flow properties is conspicuous and reflects in both mean and instantaneous properties. For the TCF, we have been able to quantify those effects, and to show that, when the large scale structures are removed, turbulence statistics have a behaviour more similar to the turbulent Couette flow. In the case of DF, the small-scale structures have shown characteristic dimensions which depends from the degree of curvature.

Finally, we want to give few hints on at least two further subjects that could represent an extension of the present thesis. The first deals with the interesting issue of spiral turbulence, which has been recognized in many experiments on Taylor-Couette apparatus with counter-rotating cylinders (see [70], [97]). Here, both laminar and turbulent regime coexist. To our knowledge this flow is still unexplored numerically, and a deep investigation could give better insights into the comprehension of the boundary between the laminar and turbulent regions. The second research is related to analysis and implementation of a suitable control strategy (e.g. blowing, suction, spatio-temporal modulated movement of the wall) for a DF in turbulent regime, and could provide some interesting application for engineering devices.

BIBLIOGRAPHY

[1] T. Alziary de Roquefort and G. Grillaud. Computation of Taylor Vortex Flow by a Transient Implicit Method. *Comp. Fluids*, 6:259–269, 1978.

[2] C. D. Andereck, S. S. Liu, and H. L. Swinney. Flow regimes in a circular Couette system with indipendently rotating cylinders. *J. Fluid Mech.*, 164:155–183, 1986.

[3] K. Atkhen, J. Fontaine, and J. E. Wesfreid. Highly turbulent Couette-Taylor bubbly flow patterns. *J. Fluid Mech.*, 422:55–68, 2000.

[4] A. Barcilon and J. Brindley. Organized structures in turbulent Taylor-Couette flow. *J. Fluid Mech.*, 143:429–449, 1984.

[5] A. Barcilon, J. Brindley, M. Lessen, and F. R. Mobbs. Marginal stability in Taylor-Couette flows at a very high Taylor number. *J. Fluid Mech.*, 94:453–463, 1979.

[6] G. K. Batchelor. *An Introduction to Fluid Dynamics*. Cambridge University Press, 1967.

[7] K. H. Bech, N. Tillmark, P. H. Alfredsson, and H. I. Andersson. An investigation of turbulent plane Couette flow at low Reynolds numbers. *J. Fluid Mech.*, 286:291–325, 1995.

[8] T. B. Benjamin. Bifurcation phenomena in steady flows of a viscous fluid 1. Theory. *Proc. R. Soc. London A*, 359:1–26, 1978.

[9] T. B. Benjamin. Bifurcation phenomena in steady flows of a viscous fluid 2. Experiments. *Proc. R. Soc. London A*, 359:27–43, 1978.

[10] T. B. Benjamin and T. Mullin. Notes on the multiplicity of flows in the Taylor experiment. *J. Fluid Mech.*, 121:218–230, 1982.

[11] S. B. Bland and W. H. Finlay. Transition toward turbulence in a curved channel. *Phys. Fluids A*, 3(1):106–114, 1991.

[12] O.N. Boratav and R.B. Pelz. Structure and structure functions in the inertial range of turbulence. *Phys. Fluids*, 9(5):1400–1415, 1997.

[13] A. Bottaro. On longitudinal vortices in curved channel flow. *J. Fluid Mech.*, 251:627–660, 1993.

[14] A. Bottaro, O. J. E. Matsson, and P. H. Alfredsson. Numerical and experimental results for developing curved channel flow. *Phys. Fluids A*, 3(6):1473–1476, 1991.

[15] A. Bouabdallah and G. Cognet. Laminar-turbulent transition in Taylor-Couette flow. In R. Eppler and H. Fasel, editors, *Laminar-turbulent transition*, pages 368–378. IUTAM Symposium, Springer-Verlag, 1980.

[16] P. Bradshaw. Effects of streamline curvature on turbulent flow. *AGARDograph*, 169, 1973.

[17] A. Brandstater and H. L. Swinney. Strange attractors in a weakly turbulent Couette-Taylor flow. *Phys. Rev. A*, 35(5):2207–2220, 1987.

[18] M. Brons, L. K. Voigt, and J. N. Sorensen. Streamline topology of steady axisymmetric vortex breakdown in a cylinder with co- and counter-rotating end-covers. *J. Fluid Mech.*, 401:275–292, 1999.

[19] J. E. Burkhalter and E. L. Koschmieder. Steady supercritical Taylor vortex flow. *J. Fluid Mech.*, 58:547–560, 1973.

[20] G. S. Bust, B. C. Dornblaser, and E. L. Koschmieder. Amplitudes and wavelengths of the wavy Taylor vortices. *Phys. Fluids*, 28(5):1243–1247, 1985.

[21] S. Carmi and J. I. Tustaniwskyj. Stability of modulated finite-gap cylindrical Couette flow: linear theory. *J. Fluid Mech.*, 108:19–42, 1981.

[22] S. Chandrasekhar. *Hydrodynamic and Hydromagnetic Stability.* Clarendon Press, Oxford, 1961.

[23] P. Chossat and G. Iooss. *The Couette-Taylor Problem.* Springer-Verlag, Berlin, 1994.

[24] K. A. Cliffe and T. Mullin. A numerical and experimental study of anomalous modes in the Taylor experiment. *J. Fluid Mech.*, 153:243–258, 1985.

[25] D. Coles. Transition in circular Couette flow. *J. Fluid Mech.*, 21:385–425, 1965.

[26] M. M. Couette. Sur un nouvel appareil pour l'étude du frottement des fluids. *Comptes Rendus*, 107:388–390, 1888.

[27] J. D. Crawford. Introduction to bifurcation theory. *Rew. Mod. Physics*, 63(4):991–1037, 1991.

[28] J. D. Crawford and E. Knobloch. Symmetry and Symmetry-Breaking Bifurcation in Fluid Dynamics. *Annu. Rev. Fluid Mech.*, 23:341–387, 1991.

[29] O. Czarny, E. Serre, P. Bontoux, and R. M. Lueptow. Interaction between Ekman pumping and the centrifugal instability in Taylor-Couette flow. *Phys. Fluids*, 15(2):467–477, 2003.

[30] A. Davey. The growth of Taylor vortices in flow between rotating cylinders. *J. Fluid Mech.*, 14:336–368, 1962.

[31] W. R. Dean. Fluid motion in a curved channel. *Proc. R. Soc. Lond. A*, 121:402, 1928.

[32] J. C. del Álamo and J. Jiménez. Spectra of the very large anisotropic scales in turbulent channels. *Phys. Fluids*, 15(6):L41–L44, 2003.

[33] R. Donnelly. *Evolution of instrumentation for Taylor-Couette flow*, volume 297 of *NATO ASI: Physics*, pages 1–27. Plenum Press, 1992.

[34] R. J. Donnelly and N. J. Simon. An empirical torque relation for supercritical flow between rotating cylinders. *J. Fluid Mech.*, 7:401–418, 1960.

[35] R.J. Donnelly. Experiments on the stability of viscous flow between rotating cylinders III, Enhancement of stability by modulation. *Proc. R. Soc. London Ser. A*, 281:130–139, 1964.

[36] P. G. Drazin and W. H. Reid. *Hydrodynamic Stability.* Cambridge University Press, 1982.

[37] S. Drozdov, M. Rafique, and S. Skali-Lami. An asymmetrical periodic vortical structures and appearance of the self-induced pressure gradient in the modified Taylor flow. *Theoret. Comput. Fluid Dyn.*, 18:137–150, 2004.

[38] S. Drozdov, S. Skali-Lami, and M. Rafique. An asymmetrical periodic vortical structures and the appearence of the self-induced pressure gradient in the modified Taylor flow. 13th International Couette-Taylor Workshop, 2003.

[39] S. M. Drozdov. A numerical investigation of a modified Couette-Taylor apparatus with application to industrial mixing. *Theoret. Comuput. Fluid Dyn.*, 16:17–28, 2002.

[40] B. Dubrulle and F. Hersant. Momentum transport and torque scaling in Taylor-Couette flow from an analogy with turbulent convection. *Eur. Phys. J. B*, 26:379–386, 2002.

[41] L. B. Ellis and P. N. Joubert. Turbulent shear flow in a curved duct. *J. Fluid Mech.*, 62:65–84, 1974.

[42] H. Fasel and O. Booz. Numerical investigation of supercritical Taylor-vortex flow for a wide gap. *J. Fluid Mech.*, 138:21–52, 1984.

[43] P. R. Fenstermacher, H. L. Swinney, and J. P. Gollub. Dynamical instabilities and the transition to chaotic Taylor vortex flow. *J. Fluid Mech.*, 94:103–128, 1979.

[44] W. H. Finlay, J. B. Keller, and J. H. Ferziger. Instability and transition in curved channel flow. *J. Fluid Mech.*, 194:417–456, 1988.

[45] M. Gorman and H. L. Swinney. Spatial and temporal characteristics of modulated waves in the circular Couette system. *J. Fluid Mech.*, 117:123–142, 1982.

[46] S. Grossmann and D. Lohse. Scaling in thermal convection: a unifying theory. *J. Fluid Mech.*, 407:27–56, 2000.

[47] Y. Guo and W. H. Finlay. Wavenumber selection and irregularity of spatially developing nonlinear Dean and Görtler vortices. *J. Fluid Mech.*, 264:1–40, 1994.

[48] D. Haim and L. M. Pismen. Performance of a photochemical reactor in the regime of the Taylor-Görtler vortical flow. *Chem. Eng. Sc.*, 49(8):1119–1129, 1994.

[49] P. Hall. The stability of unsteady cylinder flows. *J. Fluid Mech.*, 67:29–63, 1975.

[50] J. Hegseth, F. Daviaud, and P. Berge. *Intermittent turbulence in plane and circular Couette flow*, volume 297 of *NATO ASI: Physics*, pages 159–167. Plenum Press, 1992.

[51] S. Hirschberg. *Numerical simulation of turbulent Taylor-Couette flow*, volume 297 of *NATO ASI: Physics*, pages 149–157. Plenum Press, 1992.

[52] I. A. Hunt and P. N. Joubert. Effects of small streamline curvature on turbulent duct flow. *J. Fluid Mech.*, 91:663–658, 1979.

[53] J-Y. Hwang and K-S. Yang. Numerical study of Taylor-Couette flow with an axial flow. *Computers & Fluids*, 33:97–118, 2004.

[54] E. Ikeda and T. Maxworthy. Spatially forced corotating Taylor-Couette flow. *Phys. Rev. E*, 49(6):5218–5225, 1994.

[55] J. Jiménez. Computing high-Reynolds-number turbulence: will simulation ever replace experiments? *J. Turbulence*, 4:22, 2003.

[56] J. Jiménez and A. Pinelli. The autonomous cycle of near-wall turbulence. *J. Fluid Mech.*, 389:335–359, 1999.

[57] C. A. Jones. Nonlinear Taylor vortices and their stability. *J. Fluid Mech.*, 102:249–261, 1981.

[58] C. A. Jones. The transition to wavy Taylor vortices. *J. Fluid Mech.*, 157:135–162, 1985.

[59] J. Kim, P. Moin, and R. Moser. Turbulence statistics in fully developed channel flow at low Reynolds number. *J. Fluid Mech.*, 177:133–166, 1987.

[60] G. P. King, Y. Li, W. Lee, H. L. Swinney, and P. S. Marcus. Wave speeds in wavy Taylor-vortex flow. *J. Fluid Mech.*, 141:365–390, 1984.

[61] J. Komminaho, A. Lundbladh, and A. V. Johansson. Very large structures in plane turbulent Couette flow. *J. Fluid Mech.*, 320:259–285, 1996.

[62] E. L. Koschmieder. Turbulent Taylor vortex flow. *J. Fluid Mech.*, 93:515–527, 1979.

[63] L. Koschmieder. *Bénard Cells and Taylor Vortices.* Cambridge University Press, Cambridge, 1993.

[64] L. D. Landau and E. M. Lifshitz. *Fluid Mechanics, Course of Theorethical Physics*, volume 6. Pergamon Press, 1959.

[65] S. K. Lele. Compact finite difference schemes with spectral-like resolution. *J. Comp. Phys.*, 103:16–42, 1992.

[66] G.S. Lewis and H.L. Swinney. Velocity structure functions, scaling and transitions in high-Reynolds-number Couette-Taylor flow. *Phys. Rev. E*, 59(5):5457–4567, 1999.

[67] C.B. Liao, S.J. Jane, and D.L. Young. Numerical Simulation of Three-Dimensional Couette-Taylor Flows. *Int. J. Numer. Meth. Fluids*, 29:827–847, 1999.

[68] P. M. Ligrani, W. H. Finlay, W. A. Fields, S. J. Fuqua, and C. S. Subramanian. Features of wavy vortices in a curved channel from experimental and numerical studies. *Phys. Fluids A*, 4(4):695–709, 1992.

[69] T. T. Lim and K. S. Tan. A note on power-law scaling in a Taylor-Couette flow. *Phys. Fluids*, 16(1):140–144, 2004.

[70] H. Litschke and K. G. Roesner. New experimental methods for turbulent spots and turbulent spirals in Taylor-Couette flow. *Exp. Fluids*, 24:201–209, 1998.

[71] J. M. Lopez and F. Marques. Modulated Taylor-Couette Flow: onset of spiral modes. *Theoret. Comput. Fluid Dyn.*, 16:59–69, 2002.

[72] J. M. Lopez, F. Marques, and J. Shen. An efficient Spectral-Proiection Method for the Navier-Stokes Equations in Cylindrical Geometries. *J. Comp. Phys.*, 176:384–401, 2002.

[73] J. Lumley and P. Blossey. Control of Turbulence. *Annu. Rev. Fluid Mech.*, 30:311–327, 1998.

[74] E. Magere and M.O. Deville. Simulation of the Taylor-Couette flow in a finite geometry by spectral element method. *Applied Numerical Mathematics*, 33:241–249, 2000.

[75] K. Mahesh. A Family of High Order Finite Difference Schemes with Good Spectral Resolution. *J. Comp. Phys.*, 145:332–358, 1998.

[76] A. Mallock. Determination of the viscosity of water. *Proc. R. Soc. London Ser. A*, 45:126–132, 1888.

[77] M. Manna and A. Vacca. An Efficient Method for the Solution of the Incompressible Navier-Stokes Equations in Cylindrical Geometries. *J. Comp. Phys.*, 151:563–584, 1999.

[78] D.L. Marchisio. *Precipitation in turbulent fluids.* PhD thesis, Politecnico di Torino, 2002.

[79] P. S. Marcus. Simulation of Taylor-Couette flow. Part 1. Numerical methods and comparison with experiment. *J. Fluid Mech.*, 146:45–64, 1984.

[80] P. S. Marcus. Simulation of Taylor-Couette flow. Part 2. Numerical results for wavy-vortex flow with one travelling wave. *J. Fluid Mech.*, 146:65–113, 1984.

[81] P. S. Marcus. Turbulent Bursts in Couette-Taylor Flow. *Lecture Notes in Physics*, 566:183–200, 2001.

[82] F. Marques and J. M. Lopez. Taylor-Couette flow with axial oscillations of the inner cylinder: Floquét analysis of the basic flow. *J. Fluid Mech.*, 348:153–175, 1997.

[83] O. J. E. Matsson and P. H. Alfredsson. Experiments on instabilities in curved channel flow. *Phys. Fluids A*, 4(8):1666–1676, 1992.

[84] P. Moin and K. Mahesh. Direct numerical simulation: a tool in turbulence research. *Annu. Rev. Fluid Mech.*, 30:539–578, 1998.

[85] R. Moser and P. Moin. The effects of curvature in wall-bounded turbulent flows. *J. Fluid Mech.*, 175:479–510, 1987.

[86] R. D. Moser, J. Kim, and N. N. Mansour. Direct numerical simulation of turbulent channel flow up to Re_τ=590. *Phys. Fluids*, 11(4):943–945, 1999.

[87] R. D. Moser, P. Moin, and A. Leonard. A Spectral Numerical Method for the Navier-Stokes Equations with Application to Taylor-Couette Flow. *J. Comp. Phys.*, 52:524–542, 1983.

[88] T. Mullin. *Is chaos relevant to fluid mechanics?*, chapter 7, pages 167–185. Institute of Physics Publishing, 2003.

[89] T. Mullin, Y. Toya, and S. J. Tavener. Symmetry breaking and multiplicity of states in small aspect ratio Taylor-Couette flow. *Phys. Fluids*, 14(8):2778–2787, 2002.

[90] I. Mutabazi, A. Goharzadeh, and P. Laure. Spatiotemporal intermittency in Taylor-Dean and Couette-Taylor systems. *Lecture Notes in Physics*, 549:102–117, 2000.

[91] M. Nagata and N. Kasagi. Spatio-temporal evolution of coherent vortices in wall turbulence with streamwise curvature. *J. Turbulence*, 5(17), 2004.

[92] C. Normand. Stability of time-periodic flows in a Taylor-Couette geometry. *Lecture Notes in Physics*, 549:67–83, 2000.

[93] N. Ohmura, K. Kataoka, Y. Shibata, and T. Makino. Effective mass diffusion over cell boundaries in a Taylor-Couette flow system. *Chem. Eng. Sc.*, 52(11):1757–1765, 1997.

[94] S.-I. Pai. Turbulent Flow Between Rotating Cylinders. NACA TN 892, 1943.

[95] K. Park, C. Barenghi, and R. J. Donnelly. Subharmonic destabilization of Taylor vortices near an oscillating cylinder. *Phys. Lett.*, 78A(2):152–154, 1980.

[96] V.C. Patel and F. Sotiropoulos. Longitudinal curvature effecs in turbulent boundary layers. *Prog. Aerospace Sci.*, 33:1–70, 1997.

[97] A. Prigent and O. Dauchot. Spiral turbulence: long wavelength pattern of turbulent shear flow. 12th International Couette-Taylor Workshop, 2001.

[98] M. Quadrio and P. Luchini. Direct numerical solution of turbulent flow in a pipe with annular cross-section. *Eur. J. Mech. B-Fluids*, 21:413–427, 2002.

[99] M. Quadrio and P. Luchini. The numerical solution of the incompressible Navier–Stokes equations on a low cost dedicated, parallel computer. Technical Report DIA-SR 04-16, Politecnico di Milano, Dip. Ing. Aerospaziale, 2004.

[100] M. Rafique and S. Skali Lami. Flow Regime And Vortex Competition In Modified Taylor Couette System: Inner Rotating Wavy Cylinder Coaxial With a Smooth Stationary Outer Cylinder. 12th International Couette-Taylor Workshop, 2001.

[101] I. Raspo, S. Huges, E. Serre, A. Randriamampianina, and P. Bontoux. A Spectral Method for the simulation of complex three-dimensional rotating flows. *Computers & Fluids*, 31:745–767, 2002.

[102] W. S. Saric. Görtler vortices. *Annu. Rev. Fluid Mech.*, 26:379–409, 1994.

[103] A. Schultz and G. Pfister. Bifurcation and structure of flow between counter-rotating cylinders. *Lecture Notes in Physics*, 549:37–54, 2000.

[104] T. K. Sengupta, M. F. Kabir, and A. K. Ray. A Taylor Vortex Photocatalithic Reactor for Water Purification. *Ind. Eng. Chem. Res.*, 40:5268–5281, 2001.

[105] P. N. Shankar and M. Kumar. Experimental determination of the kinematic viscosity of glycerol-water mixtures. *Proc. R. Soc. London A*, 444:573–581, 1994.

[106] G. P. Smith and A. A. Townsend. Turbulent Couette flow between concentric cylinders at large Taylor numbers. *J. Fluid Mech.*, 123:187–217, 1982.

[107] H. A. Snyder. Change in wave-form and mean flow associated with wavelength variations in rotating Couette flow. Part 1. *J. Fluid Mech.*, 35:337–352, 1969.

[108] V. Sobolik, B. Izrar, F. Lusseyran, and S. Skali. Interaction between the Ekman layer and the Couette-Taylor instability. *Int. J. Heat Mass Transfer*, 43:4381–4393, 2000.

[109] A. E. Staples and A. J. Smits. The dynamics of spatially modulated Taylor-Couette flow. 12th International Couette-Taylor Workshop, 2001.

[110] J. T. Stuart. On the non-linear mechanics of the hydrodynamic stabiliy. *J. Fluid Mech.*, 4:1–21, 1958.

[111] H. Swinney. Turbulent Couette-Taylor Flow. ITP Conference on Physics of Hydrodynamic Turbulence, 2000.

[112] R. Tagg. The Couette-Taylor problem. *Non Linear Science Today*, 4(3):1–25, 1994.

[113] Y. Takeda. Quasi-periodic state and transition to turbulence in rotating Couette system. *J. Fluid Mech.*, 389:81–99, 1999.

[114] G. I. Taylor. Stability of a viscous liquid contained between two rotating cylinders. *Phil. Trans. Roy. Soc. London, Ser. A*, 223:289–343, 1923.

[115] L.H. Thomas. The stability of plane Poiseuille flow. *Phys. Review*, 91(4):780–783, 1953.

[116] A. A. Townsend. *The structure of turbulent shear flow.* Cambridge University Press, 1976.

[117] A. Tsameret and V. Steinberg. Competing states in a Couette-Taylor system with an axial flow. *Phys. Rev. E*, 49(5):4077–4086, 1994.

[118] V. Vaezi, E. S. Oh, and R. C. Aldredge. High-Intensity Turbulent Measurements in a Taylor-Couette Flow Reactor. *Exp. Therm. Fluid Sc.*, 15:424–431, 1997.

[119] F. Wendt. Turbulente Stömungen zwischen zwei rotierenden konaxialen Zylindern. *Ing.-Arch.*, 4:577–595, 1933.

[120] S. T. Wereley and R. M. Lueptow. Spatio-temporal character of non wavy and wavy Taylor-Couette flow. *J. Fluid Mech.*, 364:59–80, 1998.

[121] S. T. Wereley and R. M. Lueptow. Velocity field for Taylor-Couette flow with an axial flow. *Phys. Fluids*, 11(12):3637–3649, 1999.

[122] R. J. Wiener, G. L. Snyder, M. P. Prange, D. Frediani, and P. R. Diaz. Period-doubling cascade to chaotic phase dynamics in Taylor vortex flow with hourglass geometry. *Phys. Rev. E*, 55(5):5489–5497, 1997.

[123] Q. Xiao, T. T. Lim, and Y. T. Chew. Effects of acceleration on the wavy Taylor vortex flow. *Exp. Fluids*, 32(6):639–644, 2002.

[124] C.-X. Xu, J.I. Choi, and H. J. Sung. Identification and Control of Taylor-Görtler Vortices in Turbulent Curved Channel Flow. *AIAA Journal*, 41(12):2387–2393, 2003.

[125] A.J. Youd, A.P. Willis, and C.F. Barenghi. Reversing and non-reversing modulated Taylor-Couette flow. *J. Fluid Mech.*, 487:367–376, 2003.

[126] A.J. Youd, A.P. Willis, and C.F. Barenghi. Non-reversing modulated Taylor-Couette flow. *Fluid Dyn. Res.*, 2005. accepted for publication.